2009

Interactions Between Supersonic Gas Jets and Gas-Solid Fluidized Beds

Nestor Cruz

Interactions Between Supersonic Gas Jets and Gas-Solid Fluidized Beds

(Spine Title: Supersonic Gas Jets in Gas-Solid Fluidized Beds)

(Thesis format: integrated article)

by

Nestor Cruz

Graduate Program in Engineering Science
Department of Chemical and Biochemical Engineering

Submitted in partial fulfillment
of the requirements for the degree of
Master of Engineering Science

School of Graduate and Postdoctoral Studies
The University of Western Ontario
London, Ontario
July 2009

ABSTRACT

This thesis presents research on the use of attrition nozzles in gas-solid fluidized beds for two applications: green sand reclamation and particle size control in fluid cokers. These two applications make use of the same attrition principles, and the main difference between them is that for green sand reclamation fragmentation is not desired, since its goal is just to remove an outer layer of the green sand particles. The green sand reclamation method proposed in this research is a new, innovative process while jet attrition is already used in fluid cokers. In addition to fluid cokers, other applications of jet attrition in fluidized beds are in processes for the production of agricultural products, chemicals, carbon black, ceramics, minerals and metals, pharmaceuticals, cosmetics, pigments, resins and toners.

In the green sand experiments, the main objective was to determine the technical and economical feasibility of green sand reclamation using jet attrition in a gas-solid fluidized bed, and experimental results show that this proposed reclamation method may be technically and economically feasible if the green sand is calcinated prior to attrition.

In the particle size control experiments, the objective was to optimize the attrition nozzles that can be used in the fluid coking process to control the particle size distribution of the coke particles in order to maintain good fluidization. The main objective was to reduce the consumption of attrition gas. These nozzles are Laval type or convergent-divergent nozzles, and when modeling them, it was found that the original attrition nozzle has a geometrical shape that can be considered close to an optimum geometry. In addition to this, results show that grinding efficiency is correlated to the thrust produced by the supersonic nozzles.

Penetration of the gas jet created by the supersonic nozzles was studied using a set of triboelectric probes, and two correlations were presented: one that relates thrust with jet penetration, and another one that is a modification of a correlation that was proposed by Benjelloun et al. for the penetration of subsonic jets. These correlations agreed very well with the experimental data. Jet penetration studies are useful to avoid erosion of bed internals.

Keywords: *Gas-solid fluidized bed; attrition nozzle optimization; green sand reclamation; jet penetration; thrust.*

STATEMENT OF CO-AUTHORSHIP

This section presents the articles written for the thesis, and their contributors.

Chapter 2

Article Title: Green Sand Reclamation Using a Fluidized Bed with and Attrition Nozzle
Authors: Nestor Cruz, Cedric Briens, and Franco Berruti
Status: Submitted to *Resources Conservation and Recycling* (2008).
Nestor Cruz conducted the experiments, analyzed the data and wrote the manuscript. Cedric Briens and Franco Berruti supervised this work and reviewed several drafts of the paper.

Chapter 3

Article Title: Supersonic Attrition Nozzles in Gas-Solid Fluidized Beds
Authors: Nestor Cruz, Cedric Briens, and Franco Berruti
Status: To be submitted to *Chemical Engineering and Processing: Process Intensification.*
Nestor Cruz conducted the experiments, analyzed the data and wrote the manuscript. Cedric Briens and Franco Berruti supervised this work and reviewed several drafts of the paper.

Chapter 4

Article Title: Effect of Thrust on Supersonic Gas Jet Penetration in Gas Solid-Fluidized Beds
Authors: Nestor Cruz, Cedric Briens, and Franco Berruti
Status: To be submitted to *Powder Technology.*
Nestor Cruz conducted the experiments, analyzed the data and wrote the manuscript. The data was analyzed with a program written by Cedric Briens. Cedric Briens and Franco Berruti supervised this work and reviewed several drafts of the paper.

ACKNOWLEDGEMENTS

I would like to thank my supervisors Dr. Cedric Briens and Dr. Franco Berruti for their support and guidance during the time I spent doing this research. Their experience and knowledge was a key contribution to successfully finish this thesis work.

I am grateful for the financial support from Syncrude Canada Limited and the help provided by the University Machine Services, Engineering Stores and The Electronics Shop at the University of Western Ontario.

I am also so grateful to the ICFAR members for making my experience at Western better. Special thanks to Emma, Masoumeh, Ran, Rana, Sara, Aidan, Bashar, Feng, Frederic, Lorenzo, Martin, and Mohammed.

Finally, I wish to thank my family and friends, especially Sharis, who encouraged and motivated me to continue with graduate studies after being in Canada for some years.

Table of Contents

LIST OF TABLES

Chapter 2

Chapter 3

Chapter 4

Appendix

LIST OF FIGURES

Chapter 1

Chapter 2

Chapter 3

Chapter 4

NOMENCLATURE

A_e Area at the nozzle exit (m^2)

A_{th} Area at the nozzle throat (m^2)

C_g Correction factor for Benjelloun's correlation (-)

D Diameter (m)

D_e Diameter at the nozzle exit (m)

d_{gd} Gas distributor orifice diameter (m)

d_p Sauter mean particle diameter (m)

D_{th} Diameter at the nozzle throat (m)

$\dot{E}_k$ Kinetic energy of grinding gas (W)

f Friction coefficient (-)

F Thrust (N)

K Attrition constant (s^2/m^2)

L_{jet} Jet penetration depth (m)

M Momentum

$\dot{m}$ Mass flow rate of gas (kg/s)

M_e Mach number at nozzle exit (-)

M_{th} Mach number at nozzle throat (-)

p_e Gas pressure at the nozzle exit (kPa)

p_o Background pressure (kPa)

p_t Total pressure (kPa)

p_{th} Gas pressure at the nozzle throat (kPa)

R Gas constant (Nm/moles/K)

$R_{a,j}$ Jet attrition jet (kg/s)

T_e Gas temperature at the nozzle exit (K)

T_t Total temperature (K)

T_{th} Gas temperature at the nozzle throat(K)

U_e Gas velocity at the nozzle exit (m/s)

U_{eq} Equivalent velocity (m/s)

U_{gd} Gas velocity at gas distributor (m/s)

U_s Sonic velocity (m/s)

U_{th} Gas velocity at the nozzle throat (m/s)

V Voltage (V)

Greek letters

α Half angle of the sonic nozzle (degrees)

γ Specific heat ratio of the gas (-)

ε Bed voidage (-)

η Grinding efficiency (m^2/kg)

λ Correction factor for axial momentum loss (-)

λ Correction factor for axial momentum loss (-)

ρ_e Gas density at the nozzle exit

ρ_{gd} Gas density at gas distributor (kg/m^3)

ρ_p Bed particles density (kg/m^3)

ρ_{th} Gas density at the nozzle throat (kg/m^3)

CHAPTER 1

Introduction

This research studied the interactions between gas jets issuing from sonic nozzles and gas-solid fluidized beds with emphasis on possible applications to processes such as fluid coking and green sand reclamation. There are many other industrial applications of gas-solid fluidized beds in both catalytic and noncatalytic processes in the petrochemical, chemical, food and pharmaceutical industries, such as fluid catalytic cracking, polyethylene production, drying and classification, coating, and granulation. For this study sonic nozzles were used to either remove the outside layer of clay from green sand particles or to attrit particles. Green sand reclamation using a sonic nozzle in a gas-solid fluidized is studied in chapter two. Chapter three deals with the optimization of supersonic attrition nozzles and experiments in this section were conducted using silica sand particles and various supersonic nozzle geometries. In chapter four, jet penetration for different supersonic nozzles is measured and correlated.

1.1 Green sand reclamation

Sand is the largest foundry waste, and it accounts for around 70% of total waste volume. Most of the foundry sands are reclaimable, and can be effectively re-used (Simpson Technologies). Green sand is one type of foundry sand widely used in the foundry industry and its proper reclamation may lead to cost savings and improvements in quality, however, currently there is not an effective method to reclaim green sand. The method studied in this research uses jet attrition in a fluidized bed, which is not used in any of the current sand reclamation processes.

1.1.1 Foundry sands

Foundries produce castings of ferrous and non-ferrous metals, and most of the products are used in automobiles, plumbing fixtures, train locomotives, airplanes, and many other mechanical devices. The casting process requires the creation of a mold where the molten metal will be poured and cooled, and sand is the most common molding

material. High quality sand is utilized in foundries since poor quality sand can result in casting defects.

There are two different ways to use sand in metalcasting: as molding material to form the external shape of the cast part, and as core to form internal void spaces in parts such as engine blocks. In coremaking high strengths are necessary to withstand the heat of the molten metal.

The materials used to make these molds and cores depend on the type of metal being cast and on the design shape of the final product. The most common material consists of clean, uniformly sized, high quality sand that is mixed with carbon and other chemical compounds. A binder is required to bind the sand grains since they do not adhere naturally to each other, and in the case of green sand, clay is used as a binder. There are also chemical binders, which are organic compounds that are activated by a catalyst (Foundry Industry Recycling Starts Today website).

During the casting process large quantities of waste foundry sand are produced, and its recovery is possible using a procedure know as reclamation. The American Foundrymen's Society Sand Reclamation and Recovery Committee defines sand reclamation as "the physical, chemical or thermal treatment of a refractory aggregate to allow its reuse without significantly lowering its original useful properties as required for the application involved".

1.1.2 Foundry industry

Sand casting has become a stable market in North America, and international production is growing. China alone increased shipments 60% over the years of 1997 to 2002 (Dalquist and Gutowski, 2004), and now North America foundries have to compete with casting producers from places like Mexico, India and, China. This increasing international competition has lead to decrease in profits margins for the foundries and improvements in quality with regard to surface finish, dimensional accuracy and mechanical properties (Dziekonski, 2005). Sand reclamation is becoming an important step in foundry industry since this may help to reduce production costs and improve

quality. According to Dalquist, and Gutowski sand reclamation is common in the UK and US, and it is found that the small foundries could not afford to treat and reclaim their sand, while large foundries recycled up to 95% of their sand using dedicated equipment to do this.

1.1.3 Green sand characteristics

Green sand is made of 80 – 90% silica sand (SiO_2), 3.5 – 6% carbonaceous additive, 3 – 10 % clay and 3 - 4% water, and each one of these components has its specific purpose in the green sand itself and in the casting process. For the green sand reclamation, the two main components to take into account are silica sand and clay since the strong bonding between them is the main challenge in the reclamation process.

1.1.4 Sand reclamation methods

Zanneti and Fiore, 2002 reported that the green sand for molding operations can be used for several times without any significant refinement by just removing the large particles and adding new sand to replace the lost sand. However, to reuse the green sand for core operations reclamation is necessary after every casting operation. They stated that in general there are three methods for the reclamation of green sand for core operations: dry sand reclamation, wet sand reclamation and thermal reclamation.

Thermal reclamation without any attrition process only applies to chemical bonded sands, since the organic binders can be combusted at temperatures of around 600 ^{o}C. However, in the case of green sand high temperatures usually do not destroy the clay binder, and always some kind of attrition is required.

Dry mechanical attrition and pneumatic attrition use mechanical or pneumatic scrubbers to remove the lumps and binder from the sand. According to Hoyt (2001) scrubbers are the least expensive units and typically require the least floor space for their installation. Mechanical scrubbing (abrasion) moves each sand grain through a sand-to-sand or sand-to-metal interface to remove impurities (Zanneti and Fiore, 2002).

Pneumatic scrubbers use air stream to propel the grains between baffles or to hit a conical shape target that collects a layer of sand, and other grains sandblast this sand covered target, creating a sand to sand impact removing the loose material or dead clay (Granlund and Swenson, 2002).

Wet mechanical attrition uses just water, water and hydrochloric or sulfuric acid. Clay bonded systems work well with this process because the clays are very soluble in water. A disadvantage of this reclamation method is the treatment required of the water used during the process.

The most suitable method for sand reclamation will depend on the type of binder, the type of metal cast, and if the reclaimed sand will be used for molding or coremaking. Factors such as initial investment and operating costs are also important.

Granlund and Silsby (1992) suggests that a good option for reclamation of green sand is the combination of thermal and pneumatic processes. They said that if the green sand is calcined first, three benefits are achieved: removal of a high percentage of organic binders, deactivation of clays, and a partial removal of clay. The deactivation of clay makes easier its removal from the sand grains with attrition. It is found that green sand reclamation is mostly done with mechanical and pneumatic systems.

1.1.5 Proposed green sand reclamation method

The objective of the first part of the research was to determine the technical and economical feasibility of green sand reclamation using an attrition nozzle in a gas-solid fluidized bed. This proposed method uses an attrition nozzle with the purpose of breaking or removing the clay and carbonaceous layer that covers the silica sand particles. The main advantage of this method is that it does not require moving parts such as mills for grinding. It just uses particle to particle collisions and therefore there is not need to constantly replace eroded parts. Another advantage is the good mixing of the green sand particles in the gas-solid fluidized bed, which allows for uniform calcination of particles if required. It is also possible to separate the removed clay and organic material by elutriation or segregation.

When using the attrition nozzle, fragmentation and abrasion of the particles can occur (McMillan et al., 2007a). During abrasion fines are removed from the surface of the original particles, and the particle size distribution of the original particles remains nearly constant. In the fragmentation mechanism the particles break into large pieces. For this study, the desired attrition mechanism is abrasion since the objective of the green sand reclamation is to remove the shell (clay and carbonaceous material) formed around the silica sand grains, and to almost maintain the particle size distribution of the original silica sand grains. Although both mechanisms would occur while attriting the green sand, the goal is to make abrasion predominant by adjusting the operating conditions of the fluidized bed and the attrition nozzle.

For all the experiments a straight tube with a shroud (Fig. 1.1) was used, and the attriting gas was air. This type of nozzle reaches sonic velocity at the contraction, but the velocity does not go supersonic at the nozzle exit because there is not an expansion after that contraction. However, this expansion was present in most of the nozzles used in the experimental sections related to attrition nozzle optimization and jet penetration, therefore for those experiments supersonic velocities were obtained at the nozzle tip.

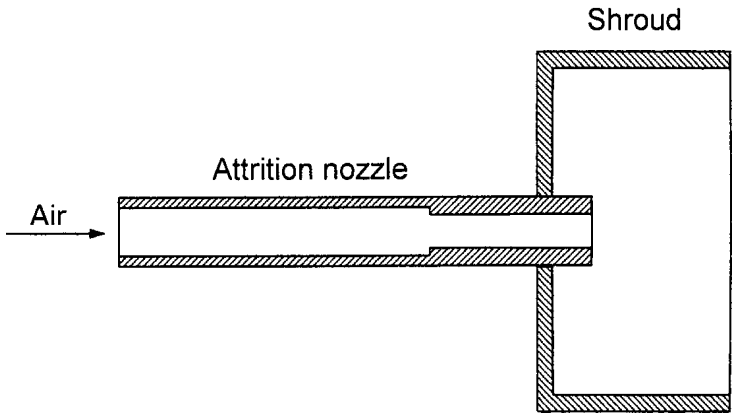

Figure 1.1: Shrouded attrition nozzle.

The purpose of the shroud was to improve mixing of particles in the fluidized bed, and entrainment of solids into the gas jet as stated by Hulet et al. (2007). According to them a shrouded nozzle produces a more stable jet in comparison with a free jet. The

shroud acts as physical barrier around the nozzle tip changing the flow pattern in the region surrounding the jet allowing entrainment of solids at a faster rate than a free jet. These characteristics are expected to make the attrition more efficient, and for this reason all experiments were conducted using a shrouded nozzle.

To measure the effectiveness of the proposed green sand reclamation method in removing the clay and organic material from the silica grains, four different characterization tests were performed before and after attrition: clay and organic content, acid request, and particle size analysis. For the clay content, organic content and acid request, the procedures described by Zanetti and Fiore (2002) and Zanetti and Godio (2006) were followed, and the particle size distribution was measured using a Malvern laser diffraction apparatus.

From the beginning it was found that the proposed reclamation method produced some separation of organic material and clay from the silica sand, and that proper removal of clay from the silica sand was difficult due to the strong bond between them. In order to make that bonding weaker and the clay on the surface of the silica sand more brittle, the green sand was calcinated at temperatures between 700 °C and 900 °C. Attrition of the calcinated green sand showed to be more effective than attrition of unburned green sand; however an additional cost was added to the process by heating the green sand at high temperatures. Due to time constraints and changes in planning and priorities, only preliminary experiments were conducted with green sand, though reclamation of green sand by using this method may be technically and economically feasible.

1.1.6 Reasons for reclaiming sand

The main reasons for reclaiming foundry sands are:

Cost savings: Use of exclusively new sand involves costs such as purchase, delivery, unloading, storing, handling and disposal. The disposal cost may include even more expensive expenditures such as landfill fees, and handling and transportation of the used sand to the landfill.

Environmentally responsible: Every day it is more difficult to dispose sand in landfills since environmental agencies want to know the chemicals in the disposal, and the effect that they could have in the environment. Besides, many companies are taking a more friendly approach towards the use of natural resources.

Technical advantages: Many foundries report that better casting can be made from reclaimed sand, and according to Simpson Technologies (1989) one explanation for this is the concept of "survival of the fittest". They state that during the cycle process of the sand some of the sand grains are given a thermal shock from the metal and/or mechanical shock from the shake-out, lump breaking, screening and handling, and the sand with poor chemical and physical structure will fracture. The sand reclamation process removes the broken grains and the strongest particles will continue to a new process.

1.2 Optimization of attrition nozzles

This part of the thesis focused on the optimization of attrition nozzles that could be used in the fluid coking process that upgrades the bitumen extracted from the oil sands in northern Alberta, Canada. Attrition nozzles are also used to grind materials such as toners, pharmaceutical powders, ultra-fine metal oxides, high purity ceramics, foodstuffs, pigments, polymer powders and ultra-fine particles for powder coating (McMillan, 2006). By optimizing these nozzles, consumption of the attriting gas is reduced, which saves energy and, in processes such as fluid coking, results in a throughput increase.

Another objective is to investigate possible relationships between grinding efficiency and parameters such as gas velocity or the thrust produced by the supersonic nozzles. This would help reach a better understanding of the grinding process, to optimize nozzle design and operation.

1.2.1 Oil sands

Alberta oil sands represent one of the largest oil deposits in the world, and 174 billion barrels of proven reserves are calculated (Alberta Energy and Utilities Board 2007). The composition of the oil sands found in Alberta is about 9-13% bitumen, 80-85% mineral matter – including sand and clays – and 3-7% water. From the mineral matter composition 15-30% are fine particles, mostly clays, with a diameter of less than 44 μm, and the challenge in production is to separate the bitumen not only from the sand but also from the micron and submicron sized clay particles (Gray et al. 2009). Bitumen is an unconventional heavy black viscous fossil oil and it is more costly to recover and process than conventional oil since it requires additional upgrading before it can be refined.

1.2.2 Oil sands production

There are two methods used for oil sands production depending on how far the oil sands are located from the surface:

Mining: It is used in locations where the oil sands are close to the surface. In these open-pit mines the oil sands are moved by trucks and shovels to a cleaning facility where the material is mixed with warm water to remove the bitumen from the sand.

In-situ: This method is required for oil sands reservoirs that are too deep to be mined, and an "in place" recovery is necessary to produce bitumen. The technologies developed for this oil sands production method apply thermal energy to heat the bitumen and allow it to flow to the well bore.

The mined oil sands are cohesive lumps that can be as large as 1m, and they are crushed and mixed with warm water to prepare a 40-55 ^{o}C slurry of much smaller lumps. This slurry is pumped through a hydrotransport pipeline to a gravity-separation vessel. While in the pipeline the bitumen is liberated from the sand grains, and at the same time bitumen droplets attach to entrained air bubbles. Once the slurry of sand and aerated bitumen enter the separation vessel, the aerated bitumen rises to the top to be skimmed off as froth, and the sand falls to the bottom together with water carrying clays and some bitumen (Gray et al. 2009).

The bitumen froth skimmed off in the gravity-separation vessel is cleaned of its sand, clay and emulsified water, but after this it is still too viscous and it contains too many impurities such as sulfur to be use as fuel and it needs to be upgrade to make suitable for the conventional refineries. Upgrading can be done by either thermal cracking, catalytic conversion or hydrogenation.

Thermal conversion or coking uses the property of hydrocarbons that if they are subjected to high temperatures they will react and change their molecular structures. At higher temperatures reactions occur faster, and during these reactions the large hydrocarbon molecules are cracked into smaller molecules. Oil companies used two types of coking to upgrade bitumen: fluid coking and delayed coking, and in both processes the thermal cracking converts the bitumen into a full range of lighter products, from gas to gas oils, and by- product coke.

Delayed coking is a batch process where bitumen is heated to 500 ^{o}C, and pumped into one side of double sided coker. The bitumen breaks into two products: solid coke and gas vapour, Once one drum is full the bitumen is diverted into the second coker to continue to cracking process, and the coke from the first coker is cut using a high pressure water drill.

Fluid coking is similar to delayed coking with the difference that is a continuous process and it uses just one coking drum. This is a non-catalytic continuous process that uses thermal cracking process chemistries (Hammond et al., 2003), and it uses the attrition nozzles studied in this research. In this process, a gas-liquid nozzle is utilized to inject the liquid (bitumen) at a temperature of around 350 ^{o}C into the fluidized bed (gas-solid) of hot coke particles that serve as a reaction media, and as a heat carrier. Uniform contact of the liquid droplets and entrained particles is essential for high yields (McMillan et al., 2005). The bitumen must contact a large amount of coke particles rapidly and uniformly to increase the rate of thermal cracking and to avoid heat or mass transfer limitations. Coking occurs at the surface of coke particles at temperatures between 510 ^{o}C and 550 ^{o}C, and the cracked hydrocarbon vapors leave the reactor, and are collected and condensed. The additional coke produced by the reaction is adhered to the surface of the bed coke particles incrementing their particle size. Supersonic attrition nozzles are used to control the coke particle size distribution by injecting superheated

steam to the nozzles producing an attrition jet inside the bed, which entrains coke particles, accelerates them at high speed within the jet cavity and slams them onto the dense bed particles near the tip of the jet cavity. McMillan et al. (2007b) also mentioned that the coke particles agglomerate when several coke particles stick together due to poor feed distribution, and that large particles will produced slugging and poor circulation, and that too many fine particles with a diameter less than 70 μm will cause agglomeration leading to poor fluidization.

Coke is withdrawn at the bottom of the reactor after passing the attrition section that controls the coke's particle size and breaks the agglomerates that are formed when several particles stick together. Particle attrition is done with high velocity steam jets produced by supersonic nozzles, and optimization of these nozzles will lead to less steam consumption, and more throughput of the reactors. After the attrition region a stripping section uses steam to remove absorbed hydrocarbons from the coke particles. Then coke is pneumatically transported to the fluid bed burner, which supplies the heat for the fluid coking process by partially combusting coke. The reheated coke is re-circulated to the top of the reactor at approximately 650 ^{o}C (House et al. 2004). Figure 1.2 shows a schematic of the fluid coking process.

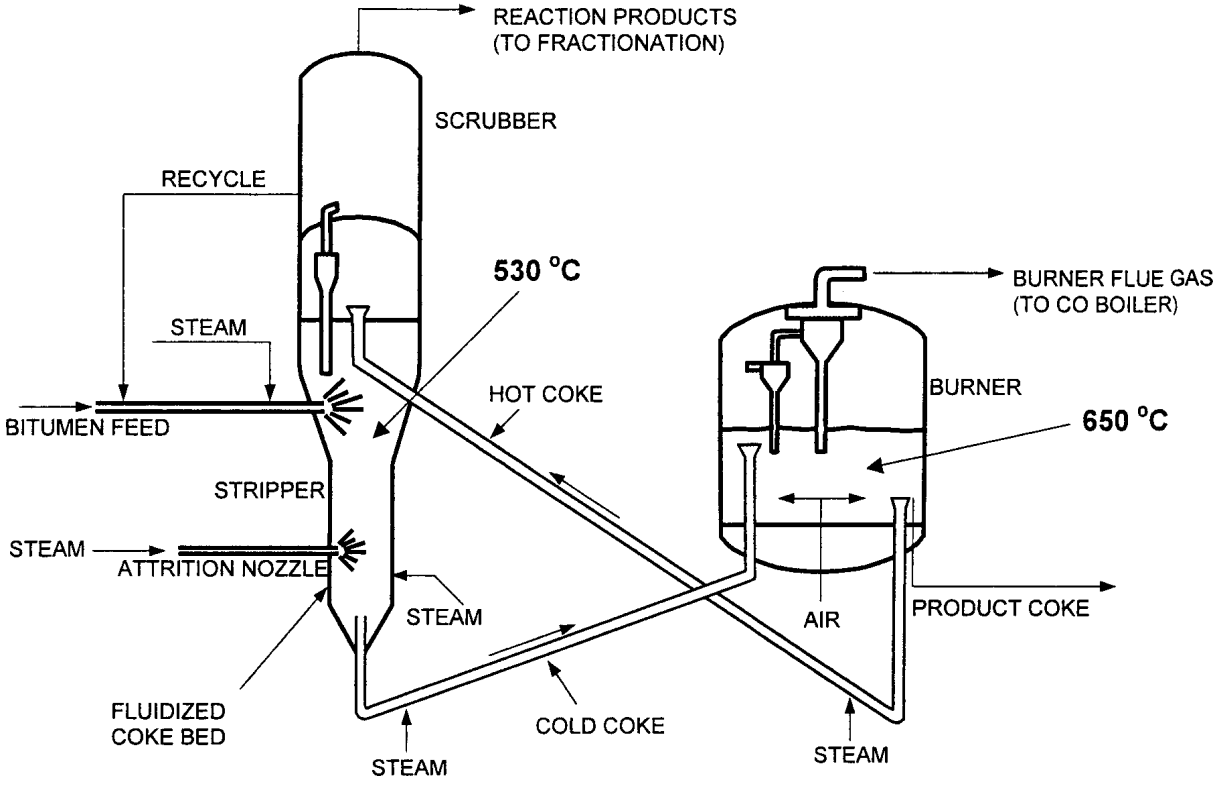

Figure 1.2: Fluid coker schematic, adapted from House et al. (2004).

1.2.3 Attrition nozzles used in fluid coking

For attrition of the particles in processes such as fluid coking, a Laval type nozzle or a convergent-divergent nozzle (Fig. 1.3) can be used, and this nozzle has a specific design whose dimensions may be considered within an optimal range. However, understanding of the way this nozzle works is not very clear, and it is suspected that the nozzle can be improved or a new better geometry can be created. In the attempt to optimize this nozzle, different geometries were made and tested for grinding efficiency of silica sand particles.

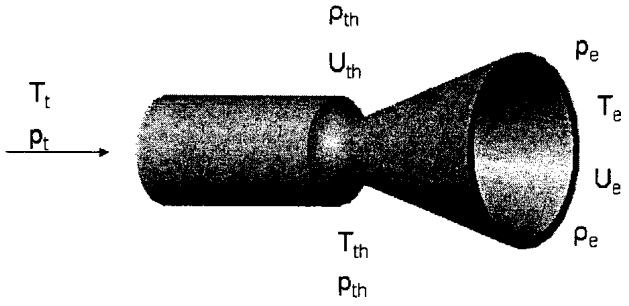

Figure 1.3: Convergent-divergent (C-D) nozzle showing different gas properties at the exit and at the throat.

The grinding efficiency (m^2/kg), η, was defined as the new surface area created during attrition (m^2/s) per mass of gas (kg/s) used:

$$Grinding\ efficiency\ (\eta) = \frac{New\ surface\ area\ created\ (m^2/s)}{Mass\ of\ gas\ used\ (kg/s)} \tag{1.1}$$

From this equation it is inferred that an optimum attrition nozzle will use the less possible amount of attriting gas to grind the bed particles.

As it was mentioned in the green sand reclamation section, the difference of this nozzle with the one used for green sand reclamation is the divergent area. The fluid coking attrition nozzle has a divergent section that accelerates the gas jet to supersonic velocities, and this high exit velocity provides a grinding efficiency advantage over the simple straight sonic nozzle as it was found in this and previous studies (McMillan et al. 2007a). However, a convergent-divergent nozzle may cause fragmentation of particles, which is not desired for greensand reclamation, for which a proper balance between mass flow rate and exit velocity must be achieved to make abrasion the predominant attrition mechanism. The green sand reclamation study focused on demonstrating that jet attrition

could be successfully used and left detailed optimization of nozzle geometry for future studies.

The gas fed to these nozzles changes its properties through the nozzle, and values for temperature, pressure and velocity can be calculated using equations for compressible flow (John and Keith, 2006). The momentum and thrust produced by the supersonic nozzles can also be calculated. In addition to this, different gases at different temperatures and pressures can be compared for grinding efficiency.

1.2.4 Comparison of attrition in green sand reclamation and in fluid coking

The main difference between the green sand and the coke used in fluid coking is that the green sand has several components that are intentionally mixed to produce certain characteristics necessary for casting processes, while coke in the thermal cracking process is made mostly of a single component that constantly increases its size due to the formation and deposition of the coke produced in the reaction.

In both green sand reclamation and fluid coking applications, attrition occurs through the two main mechanisms mentioned previously: abrasion and fragmentation. In green sand reclamation abrasion is desired, and in fluid coking process fragmentation is the best since generation of fine particles negatively affects the process. According to Palaniandy et al. (2007) silica sand abrasion is predominant at low grinding pressures, and fragmentation takes place at high attrition pressures. It is expected that this applies to most of the particles used in fluidization including coke and green sand.

1.3 Horizontal gas jet penetration into gas-solid fluidized beds

It is important to understand the interaction between gas jets and fluidized beds, and estimation of the jet penetration length is a key characteristic in fluidized bed design since jets may impact and erode bed internals. For this particular research, it is of interest to estimate the penetration length of the attrition jets used in the coking process. This

information may be also useful for the eventual design of green sand reclamation equipment.

Another objective of the jet penetration experiments was to demonstrate the correlation that exits between jet penetration and the thrust produced by the supersonic nozzles.

1.3.1 Jet penetration measurement technique

This study used a set of tribolectric probes to measure the gas jet penetration length. The method was taken from Dawe et al. (2008), but for this research the triboelectric probes were arranged in a different way.

This technique takes advantage of the phenomenon known as tribo-charging in which charges are exchanged whenever any two surfaces come into contact with each other, and a net charge will be created on each of the surfaces when they are separated. That occurs with conductors, semiconductors or insulators; solids or liquids; and even for cases where the bulk materials are the same (Castle, 1997). The objective with the triboelectric probe technique is to measure just the current created by contact between high velocity, entrained particles in the gas jet and a metal tip.

1.4 References

Castle, G. S. P., "Contact Charging Between Insulators", *J. Electrostat.* **40&41** 13-20 (1997).

Dalquist, S., and Gustowsky, T., "Proceedings of IMECE2004: 2004 ASME International Mechanical Engineering Congress & Exposition", November 13-19, 2004, Anaheim, California.

Dawe, M., Briens, C., and Berruti, F., "Study of Horizontal Sonic Gas Jets in a Gas-Solid Fluidized Beds", *Can. J. Chem. Eng.*, **86** 506-513 (2008).

Dziekonski, P. E., "Current Trends in Foundries' Use of Silica Sand", *Foundry Manage. & Technol.*, **133**, 1, 24-26 (2005).

Granlund, M. J., and Silsby, D. V., "Thermal-Pneumatic Reclamation of Molding Sand for Reuse in Core Work", *Simpson Technologies*, Application #500, (1992). http://www.simpsongroup.com/tech/ThermalPneuReclamation.pdf

Granlund, M.J., and Swenson, L., "Sand Reclamation = Sand Savings with Proper Planning", *Modern Casting*, **92**, 8, 29-31 (2002).

Gray, M., Xu, Z., and Masliyah, J., "Physics in the Oil Sands of Alberta", *Physics Today*, **62** 31-35 (2009).

Hammond, D.G., Lampert, L.F., Mart, C.J., Massenzio, S.F., Phillips, G.E., Sellards, D.L., and Woerner, A.C., "Review of FLUID COKING™ and FLEXICOKING™ Technologies", *Exxon Mobil Research and Engineering Company*, Sixth Topical Conference on Refining Processing Tutorial on Resid Upgrading, American Institute of Chemical Engineers Spring National Meeting, (2003).

House, P. K., Saberian, M., Briens, C.L., Berruti, F., and Chan, E., "Injection of a Liquid Spray into a Fluidized Bed: Particle-Liquid Mixing and Impact on Fluid Coker Yields", *Ind. Eng. Chem. Res.*, **43** 5663-5669 (2004).

Hoyt, D., "Should your Foundry Be Reclaiming its Sand?", *Modern Casting*, **91**, 8, 40-41 (2001).

Hulet, C., McMillan, J., Briens, C., Berruti, F., and Chan, E.W., "Visualization of the Effect of a Shroud on Entrainment of Fluidized Solids into a Gas Jet". *Int. J. Chem. React. Eng.*, **5** S4 (2007).

John, J. E., Keith, T. G., *Gas dynamics*, Pearson Prentice Hall, 3rd edn., 68-102 and 283-331 (2006).

McMillan, J., "Characterization of the Interactions Between High Velocity Jets and Fluidized Particles". *PhD Thesis*, The University of Western Ontario, (2006).

McMillan, J., Briens, C., Berruti, F., and Chan, E., "High Velocity Attrition Nozzles in Fluidized Beds", *Powder Technol.*, **175** 133-141 (2007a).

McMillan, J., Briens, C., Berruti, F., and Ed, C., "Particle Attrition Mechanism with a Sonic Gas Jet Injected into a Fluidized Bed", *Chem. Eng. Sci.*, **62** 3809-3820 (2007b).

McMillan, J., Zhou, D., Ariyapadi, S., Briens, C., Berruti, F., and Chan, E., "Characterization of the Contact between Liquid Spray Droplets and Particles in a Fluidized Bed", *Ind. Eng. Chem. Res.*, **44** 4931-4939 (2005).

Palaniandy, S., Azizli, K. A. M., Hussin, H., and Hashim, S. F. S., "Effect of Operational Parameters on the Breakage Mechanism of Silica in a Jet Mill", *Miner. Eng.*, **21** 380-388 (2008).

Strobl, S.M., "The Fundamentals of Green Sand Preparation and Control", *Simpson Technologies Corporation*, Aurora, Illinois, USA (2000).

Zanetti, M.C., Fiore, S., "Foundry Processes: The Recovery of Green Moulding Sands for Core Operations", *Resour. Conserv. & Recy.*, **38**, 243-254 (2002).

Zanetti, M.C., Godio, A., "Recovery of Foundry Sands and Iron Fractions from an Industrial Waste Landfill", *Resour. Conserv. & Recy*", **48** 396-411 (2006).

Websites

AFS (American Foundry Society), "The Foundry Industry...Recycling Yesterday, Today and Tomorrow".
http://www.afsinc.org/images/stories/govaffairs/recyclingbrochure_lr.pdf

Alberta Energy and Utilities Board. "Oil Reserves and Production 2007" http://www.energy.gov.ab.ca/Oil/pdfs/AB_OilReserves.pdf

First (Foundry Industry Recycling Starts Today), "What is recycled foundry sand?" http://www.foundryrecycling.org/Home/tabid/36/Default.aspx

Simpson Technologies, "Sand Reclamation", Application #500.
http://www.simpsongroup.com/tech/SandReclamation.pdf

CHAPTER 2

Green Sand Reclamation Using a Fluidized Bed with an Attrition Nozzle

2.1 Introduction

Foundries produce castings of ferrous and non-ferrous metals, and most of the products are used in automobiles, plumbing fixtures, train locomotives, airplanes, and many other mechanical devices. The casting process requires the creation of a mold or core of specific designs, where the molten metal is poured and cooled. Molds are used to form the external shape of the cast part, and cores to form internal void spaces in parts such as engine blocks. In core making, high strengths are necessary to withstand the heat of the molten metal (Foundry Industry Recycling Starts Today website).

The materials used to make these molds and cores depend on the type of metal being cast and on the design shape of the final product. The most common material consists of clean, uniformly sized, high quality sand that is mixed with carbon and other chemical compounds. Since sand grains do not adhere naturally to each other, binders are used to bind the grains and keep the shape of the mold or core during the pouring of the molten metal and the cooling of the casting. Two general types of binder systems are used (Foundry Industry Recycling Starts Today website):

Clay bonded systems (Green sand): Green sand is used to produce about 90% of casting volume in the U.S., and it is used mostly in mold making.

Chemically bonded systems (Resins): Resins are used both in core making and in mold making. The majority of the chemical bonded systems consist of an organic binder that is activated by a catalyst, although some systems also use inorganic binders.

The clay bonded system, or green sand, has a composition of 80 – 90% silica sand (SiO_2), 3.5 – 6% carbonaceous additive, 3 – 10 % clay and 3 - 4% water. The silica sand provides the structure for the mold (Zanetti and Fiore, 2002). The size and distribution of the sand grains affect the surface finish of the casting, and the ability of the mold to facilitate the evacuation of gases formed during the transformation of water to steam and during the decomposition of the organic constituents of the core binders and green sand additives. Sand distribution is also important to reduce the occurrence of sand expansion defects (Strobl, 2000). The carbonaceous additive is used to enhance the refractory properties of the sand, improve casting surface finish, and help reduce adhering sand grains, the occurrence of metal penetration, and expansion type defects caused by

nonlinear growth of silica aggregates. These additives are mostly bituminous coal and are used to cast iron sand systems (Strobl, 1994).

Clay acts as an adhesive to maintain the mold shape at both ambient and high temperatures. Sodium and calcium bentonite are the two types of natural clays, and they are utilized in the majority of the metalcasting operations. Sodium bentonite gives higher dry and elevated temperature compressive strengths, as well as wet tensile strength, and calcium bentonite has greater ability to flow freely through the sand system (Strobl, 2000).

Water is added to the green sand system to activate the clay. The moisture content of the green sand is extremely critical and can affect almost all the physical properties measured in the foundry (Strobl, 2000). Chemical binders may be added to the green sand for some casting processes such as core making (Zanetti and Fiore, 2002).

According to Zanetti and Fiore (2002), the main properties of a green sand mixture used in iron cast foundry are:

Constant particle size distribution (0.1 to 0.4 mm): Gives smooth and uniform surface to the metal. This property is measured using the thinness index (AFS), which shows the number of silica grain particles that remain on 1 mm^2 of the sieve surface. The thinness index becomes higher as the amount of fine particles increase. This index is calculated after the particle size distribution analysis.

Refractory: Molding sand must be chemically and physically stable on contact with melting metal. Organic material (coal dust) creates a protective layer (CO_2) between the mold and casting.

Permeability: Allows the passage of gases, produced during metal casting, through tiny channels in the mold. These channels are the result of the constant particle size and the binding agent.

Cohesion: The mold preserves the shape obtained with compression, thanks to the binding agent.

During the casting process large quantities of wasted foundry sand are produced, and its recovery is possible using a procedure known as reclamation. Zanetti and Fiore (2002) mention that, in molding operations, the green sand can be reused several times without any significant refinement, but for core making operations a more elaborated

reclamation process is required. They identify three methods for green sand reclamation for core operations: dry mechanical reclamation, wet mechanical reclamation, and thermal reclamation. Dry mechanical reclamation, where pneumatic scrubbers are used, is the closest process to a fluidized bed with an attrition nozzle. Pneumatic scrubbers use air to propel the green sand particles onto a target, where attrition results from particle target and particle-particle collisions. Attrition nozzles in fluidized beds use only particle on particle impact.

McMillan et al. (2007) state that there are two main attrition mechanisms: abrasion and fragmentation. Abrasion takes place when fines are removed from the surface of the original particles. During abrasion, many fines are generated and the particle size distribution of the original particles remains nearly constant. In the fragmentation mechanism the particles break into pieces larger than the ones in the abrasion mechanism. Figures 2.1 and 2.2 show the abrasion and fragmentation mechanisms.

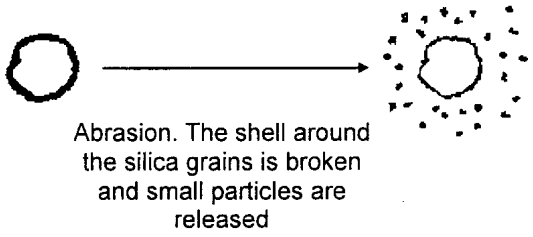

Figure 2.1: Particle abrasion mechanism.

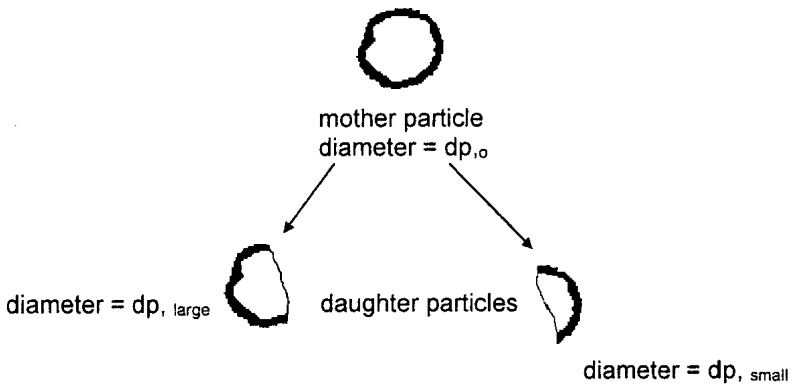

Figure 2.2: Particle breakage mechanism (McMillan et al. 2007).

For this study, the desired mechanism is abrasion since the objective of the green sand reclamation is to remove the shell (clay and carbonaceous material) formed around the silica sand grains, and to maintain the particle size distribution of the original silica sand grains. Although both mechanisms would occur while attriting the green sand, the key goal is to make abrasion predominant by adjusting the operating conditions of the fluidized bed and of the attrition nozzle.

The attrition nozzle used in these experiments is a straight tube with a shroud. Hulet et al. (2007) give a good explanation on how an attrition nozzle works with and without a shroud. They stated that the shroud forms a physical barrier around the nozzle tip changing the flow pattern in the region surrounding the jet, and they found that a shrouded nozzle jet is more stable and entrains solids at a faster rate than a free jet. These characteristics of the shrouded nozzle jet are expected to make the attrition more efficient, and for this reason all experiments were conducted using a shrouded nozzle. Figure 2.3 shows how the particles are entrained in a free nozzle and a shrouded nozzle.

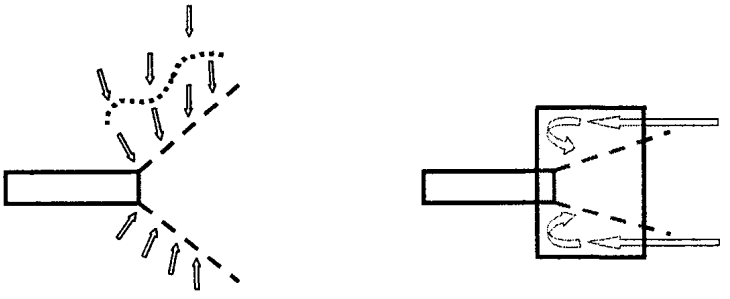

Figure 2.3: Entrainment into the gas jet (a) free nozzle (b) nozzle with shroud. The arrows indicate the direction of solids flow and relative velocity (the jet expansion angle has been exaggerated for the illustration). (Taken from Hulet et al. 2007).

2.2 Materials and methods

To determine the degree of removal of clay and organic material from the silica grains, four different characterization tests were performed before and after attrition: clay and organic content, acid request, and particle size analysis. The particle size distribution

was measured using a Malvern laser diffraction apparatus. For the clay content, organic content and acid request, the procedures described by Zanetti and Fiore (2002) and Zanetti and Godio (2006) were followed.

2.2.1 Clay (oolitic) content

Zanetti and Fiore (2002) introduced a procedure to measure the ageing degree of the green sand. This test calculates both the active and inactive clay, and it starts by calcining the green sand sample at 900 °C for 4 hours. Then 25 grams of the burned sample are reacted first with 100 ml of 6 N hydrochloric acid by boiling the mixture for 25 minutes. Once the acid reaction is finished, the sand is washed several times with distilled water until the pH is almost neutral. Next, an alkaline solution, prepared by adding 30 g potassium hydroxide to 125 ml of distilled water, is added to the remaining sample and boiled for another 25 minutes. After the resulting reaction, the sand is washed again with distilled water until no alkalinity is detected. Finally, the remaining sand is filtered and dried and the weight difference between the initial sample and the treated sample gives the oolitic or clay content.

2.2.2 Organic content

The samples are dried and then burned for 30 minutes at 900 °C. The difference between the initial and final weights gives the organic content.

2.2.3 Acid request

Zanetti and Godio (2006) describe this test as the quantity of acid that is neutralized by the alkali contained in the green sand. They state that this test is important to determine if the recovered green sand and the resin used in core making are compatible. To calculate the acid request, 50 ml of water and 50 ml of 0.1 N hydrochloric acid are added to a sample of 50 grams of recovered green sand. This mix is stirred for around 15 minutes and then titrated with a solution of 0.1 N sodium hydroxide until a pH

of 5 is obtained. The difference between 50 ml and the quantity of sodium hydroxide used in the titration gives the acid request.

For reclaimed green sand used in core making, the required value for both clay and organic content is less than 2 wt %, and acceptable acid request values are between 0 and 6 ml.

2.3 Experimental set up

The fluidized bed used during the experiments is represented in Figure 2.4. The bed dimensions are 0.94 m height and a rectangular cross section of 0.50 m by 0.10 m, and it is equipped with a cyclone to collect most of the fines elutriated.

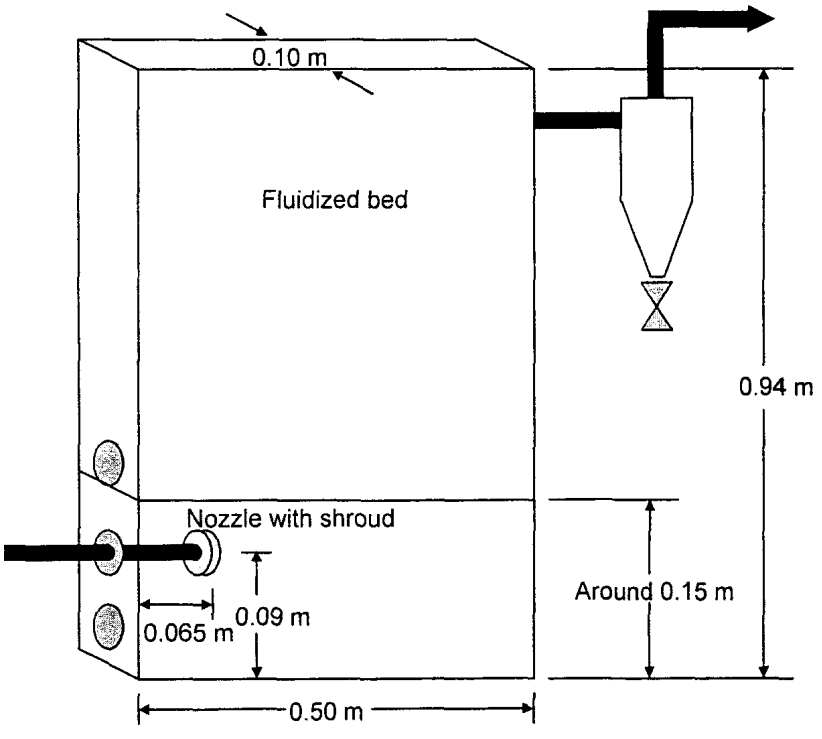

Figure 2.4: Fluidized bed diagram.

For all the experiments only one type of attrition nozzle was used, and this is a simple straight tube with an exit diameter of 4.3 mm, and a length of 19 mm. The shroud

placed around the nozzle tip has a diameter of 44 mm, and a length of 20 mm. Figure 2.5 shows the nozzle and the shrouded nozzle configuration. For all the tests, the nozzle was located inside the bed at 0.09 m from the gas distributor and around 0.065 cm from one of the lateral bed walls. In all cases air injection was horizontal.

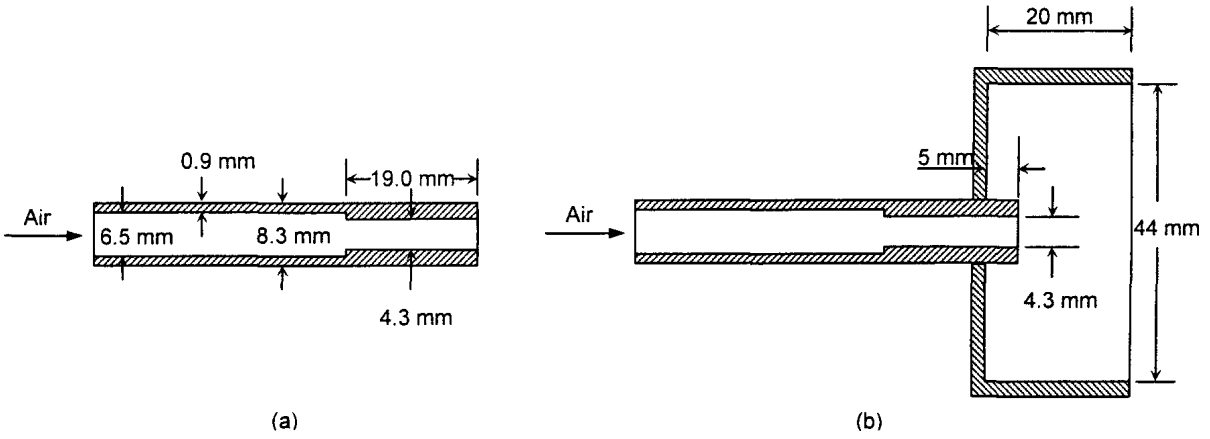

Figure 2.5: Attrition nozzle representation (a) free nozzle (b) nozzle with shroud.

The green sand used came from two different foundries identified as Foundry A and Foundry B. Green sand from Foundry A had to be dried, and both green sands were sieved using the tray with a 12 (1.4 mm) mesh screen. Foundry A green sand was used for the preliminary assessment of the behavior of the green sand in the fluidized bed.

The weight percentages of clay and organic content for the original Foundry A green sand were around 14% and 3.5% respectively while for the original Foundry B green sand, the clay content was roughly 5.5% and the organic content 3.8%. The acid request for the original Foundry B green sand was approximately 3.9 ml. Acid request was not calculated for green sand from Foundry A. The maximum requirements for core making operations is a green sand with a clay and organic content of less than 2 wt %, and the acid request is between 0 and 6 ml.

Preliminary tests indicate that the green sand segregates once the air supply to the attrition nozzle and to the gas distributor are stopped. Initial sampling of the bed showed that a layer of fines particles was formed on the top of the bed, and this layer was

relatively small compared to height of the bed. These fines have different organic and clay content, and a particle size distribution that is clearly different from the rest of the bed particles. It was decided that the particles of interest for this study were located under the layer of fines, and a solids probe sampler was used to collect samples of these particles. Figure 2.6 shows how sampling was performed and a representation of the sampler.

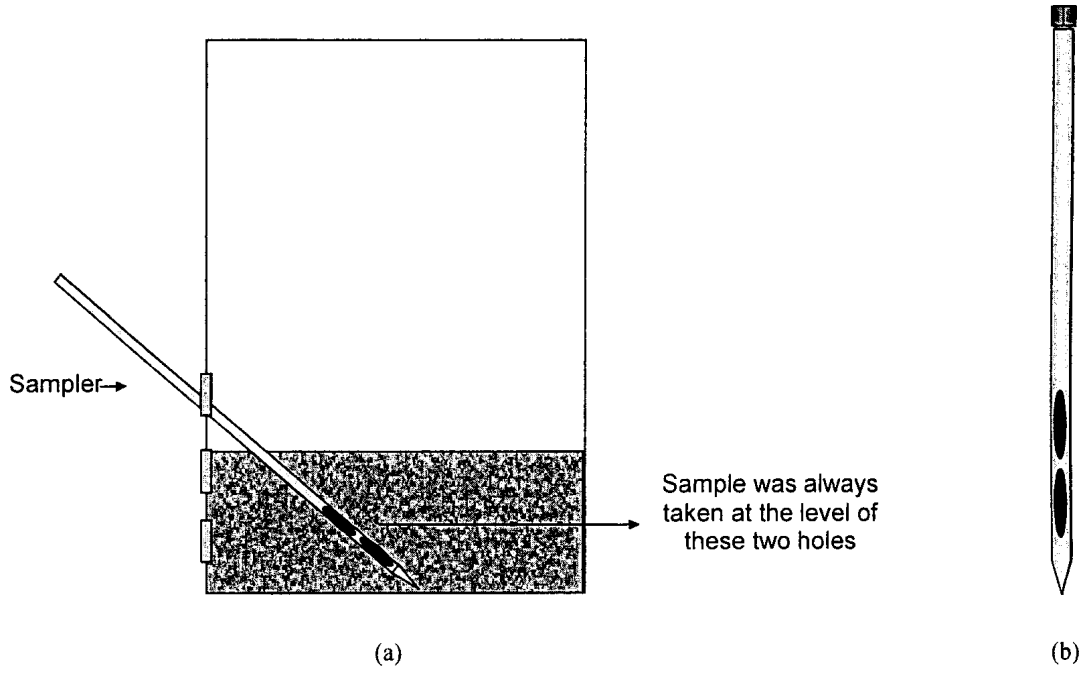

Figure 2.6: Representation of (a) the way sampling was done, and (b) the sampler.

Once an experimental procedure had been developed, more detailed tests were conducted using green sand from Foundry B. Besides clay content, organic content, acid request, and particle size analysis, the height of the bed and the fines collected in the cyclone were measured. Two air pressures were used for the attrition nozzle: 350 and 550 kPa, and the pressure for the fluidization air was always around 350 kPa, resulting in a superficial gas velocity of approximately 0.05 m/s.

Some samples of green sand from Foundry B were calcined at temperatures of 705 °C, 816 °C, and 900 °C, and attrition experiments were performed using the original unburned green sand as well as the calcined green sand to compare the effect of prior

calcination. A furnace was used to burn the green sand that was placed in a custom made ceramic container made of alumina. While heating the green sand, it was agitated with a customized rake, to simulate the commercial calcination conditions, which would possibly be carried out in a hot fluidized bed.

Samples of between 10.5 kg and 13 kg were used for the attrition tests in the fluidized bed. For all Foundry B samples, attrition was performed at different time intervals and after each interval, a sample was taken from the bed and the fines collected in the cyclone were removed and collected. Time intervals between samples were set from the change in bed height after every attrition run. For example, when attriting calcined green sand, the bed height changes faster than when attriting unburned green sand. After every attrition interval, the bed height was measured, and the fines in the cyclone were collected and weighted.

2.4 Results and discussion

In general, the results show that using an attrition nozzle in a fluidized bed achieves some separation of the clay and organic material from the green sand. As expected, the degree of separation of clay and organic material depends on the pressure upstream of the attrition nozzle. The results also demonstrate that calcination of the green sand before attrition helps remove the clay.

In regards to the particle size distribution, it is noticed that for the bed particles located under the layer of fines, the Sauter mean diameter increases due to the removal of the small particles from the green sand. Figure 2.7 shows the particle size distribution for an untreated sample of Foundry A green sand, and for a sample that was attrited for approximately 30 minutes with an attrition nozzle pressure of 350 kPa. In this figure, it is seen that as a result of the attrition and elutriation most of the small particles between 10 and 100 μm are removed from the bed. Figure 2.8 shows similar results for a Foundry B original green sand sample, and green sand that was attrited for 50 minutes, using an attrition nozzle pressure of 350 kPa. By comparing the two previous figures, it is

observed that Foundry B green sand has a more uniform particle size distribution than Foundry A green sand as well as a smaller Sauter mean diameter.

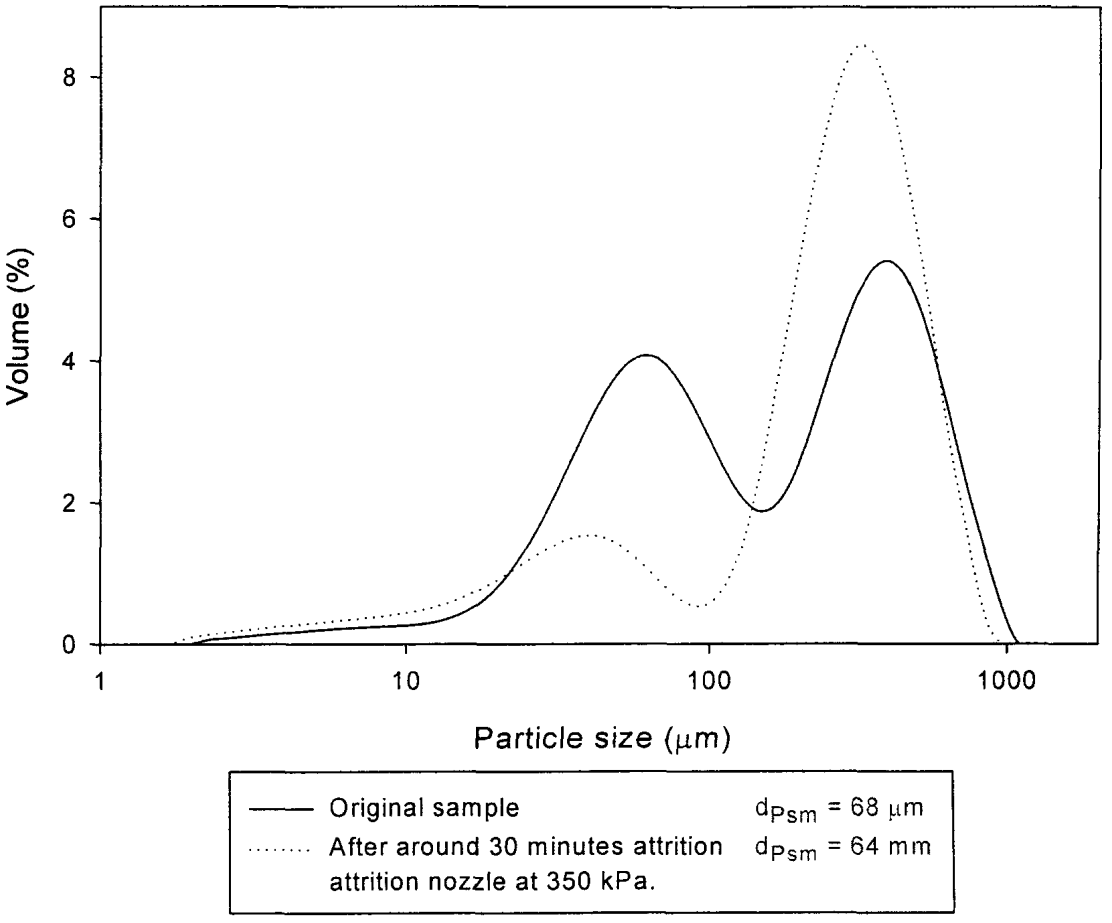

Figure 2.7: Particle size distribution for unburned Foundry A green sand before and after attrition using 350 kPa.

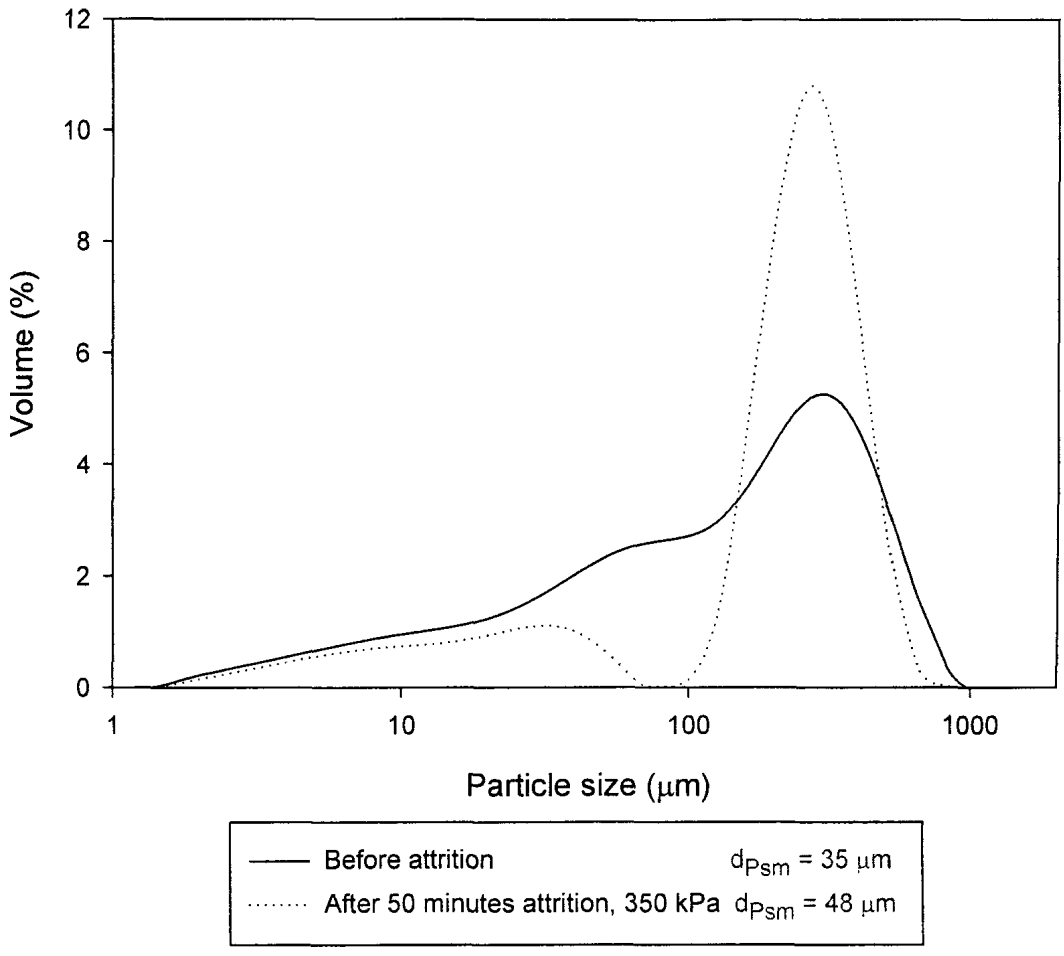

Figure 2.8: Particle size distribution for unburned Foundry B green sand before and after attrition using 350 kPa.

Figure 2.9 shows that burned or calcined green sand has a particle size distribution that is a lot more uniform than for unburned green sand, and the Sauter mean diameter increases considerably. In green sand, the smallest particles are made of organic material that is combusted away during calcination.

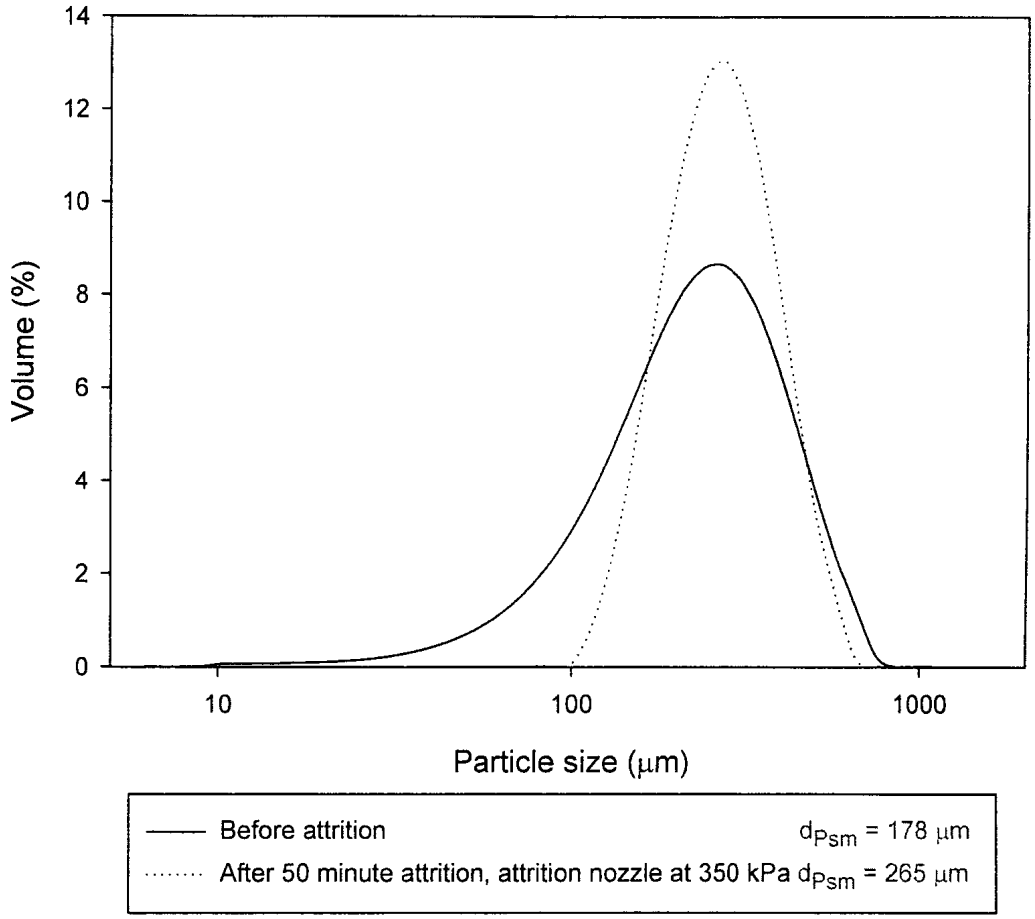

Figure 2.9: Particle size distribution for burned Foundry B green sand before and after attrition. Green sand burned at 900 °C and attrition nozzle pressure of 350 kPa.

If Figures 2.8 and 2.9 are compared, it can be said that particles smaller than 10 μm are made of organic material, and that for the burned green sand, most of the particles between 10 and 100 μm correspond to small clay particles that are free or not solidly bound to the silica grains.

Figures 2.7, 2.8 and 2.9 suggest that abrasion is the predominant attrition mechanism, as was the goal of the experiments. Figure 2.10 and 2.11 confirm this finding as it is seen that, for the unburned green sand, smaller particles are separated and that the Sauter mean diameter increases progressively after each attrition run. Figure 2.11

illustrates that for unburned green sand there was abrasion of the bigger particles and particles of approximately less than 80 μm are elutriated.

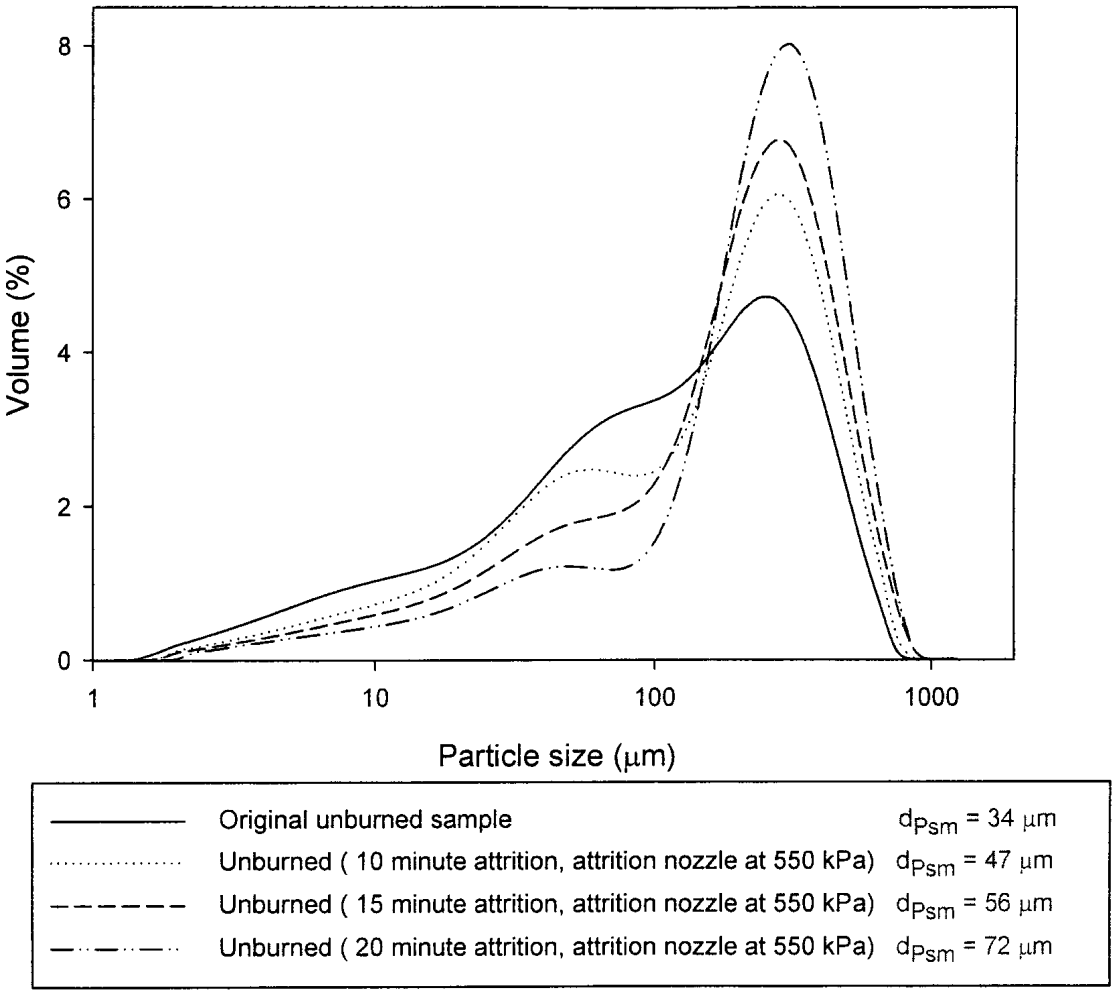

Figure 2.10: Particle size distribution for unburned Foundry B green sand and the attrition nozzle at 550 kPa.

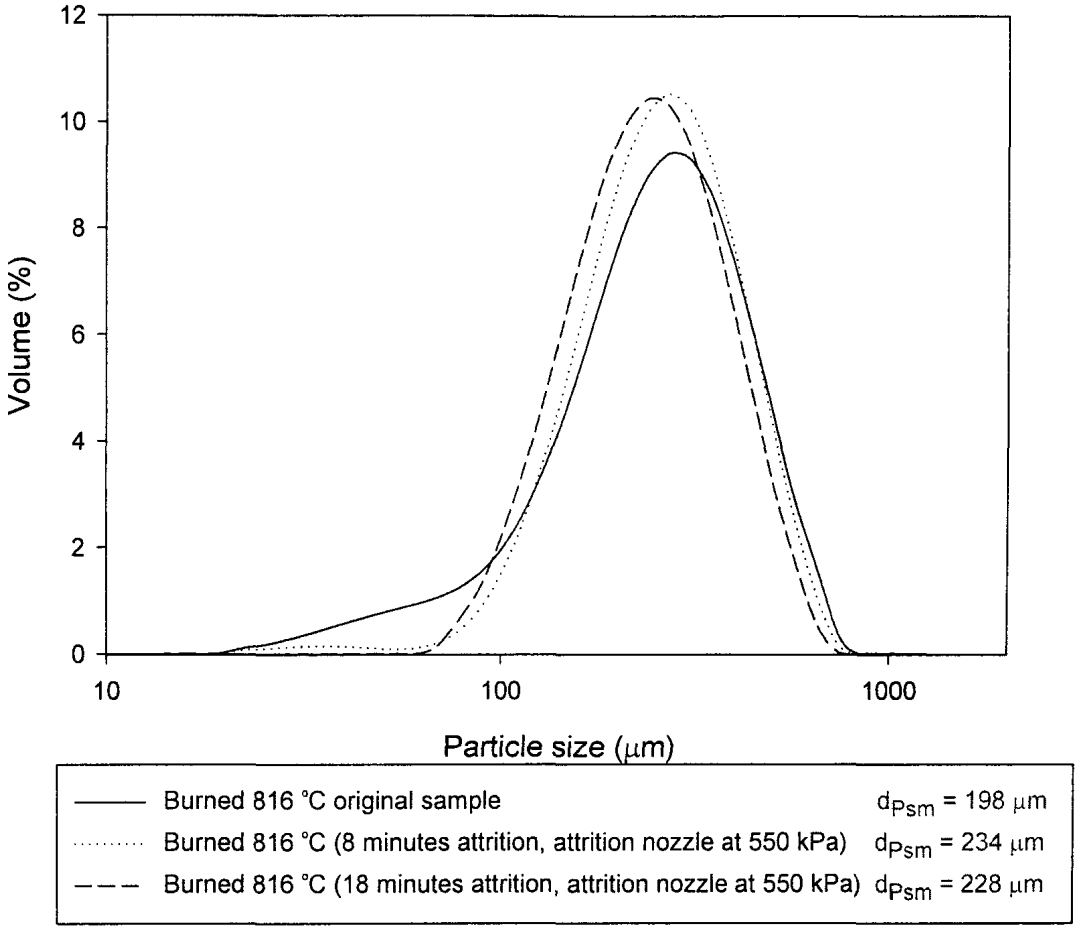

Figure 2.11: Particle size distribution for burned (816 °C) Foundry B green sand and the attrition nozzle at 550 kPa.

In general it is noticed that when attriting calcined green sand, the separation of small particles was easier and faster with burned green sand. Also, it is suspected that the undesirable fragmentation mechanism starts to predominate over abrasion once most of the small free particles as well as the particles with the weakest bond to the silica grains have been removed from the green sand.

Figure 2.12 and 2.13 compare samples before attrition and after attrition, respectively. Figure 2.12 shows the difference in particle size distribution for the original Foundry A and Foundry B green sand samples as well as the change in particles size

distribution when the untreated samples are calcined. The same variation is observed in Figure 2.13.

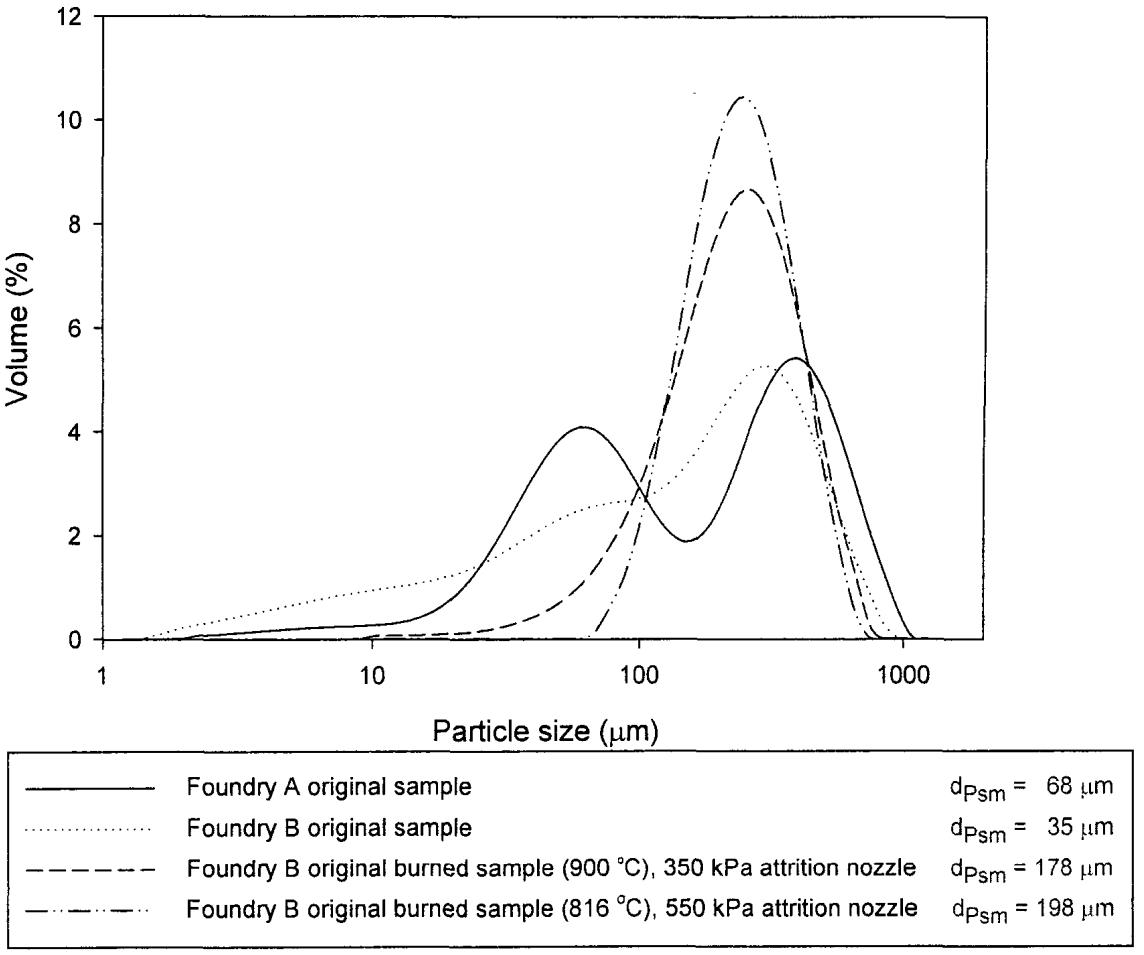

Figure 2.12: Particle size distribution for samples before attrition.

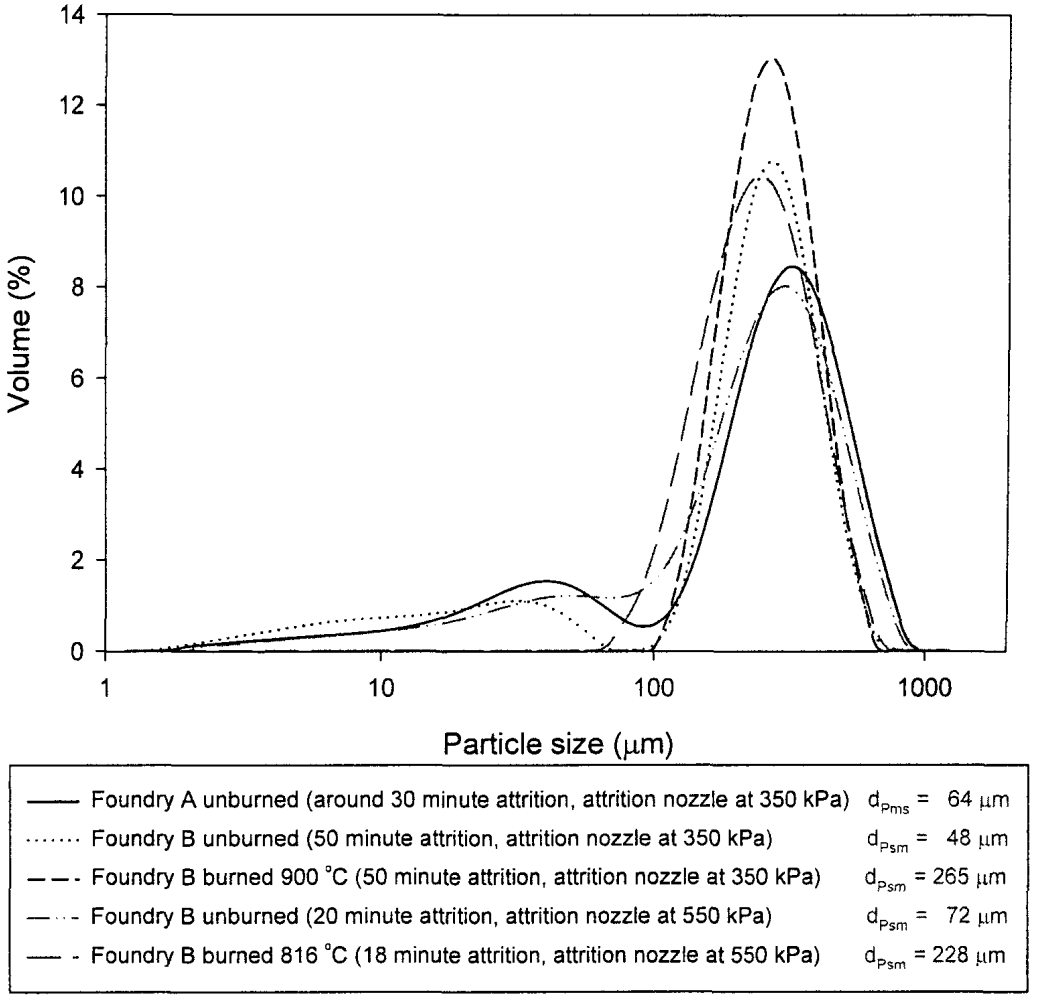

Figure 2.13: Particle size distribution for sample after attrition.

Oolitic and organic content results for the fines collected in the cyclone and for the samples taken from the bed show that during attrition, there is some separation of clay and organic material, and the rate of removal of these components is higher at the beginning of attrition. Figure 2.14 illustrates the Foundry B results for clay content in the samples taken from the bed, and it can be seen that, for burned green sand, the clay is separated at a faster rate than for unburned green sand. However, when using an attrition nozzle pressure of 550 kPa for unburned green sand, the rate of reduction of clay content is similar to the case of calcined green sand. It is believed that it is easier to remove the clay from burned green sand because the clay becomes brittle when is calcined and is

also presumed that the bond between the silica sand and the clay may have been weakened after calcination.

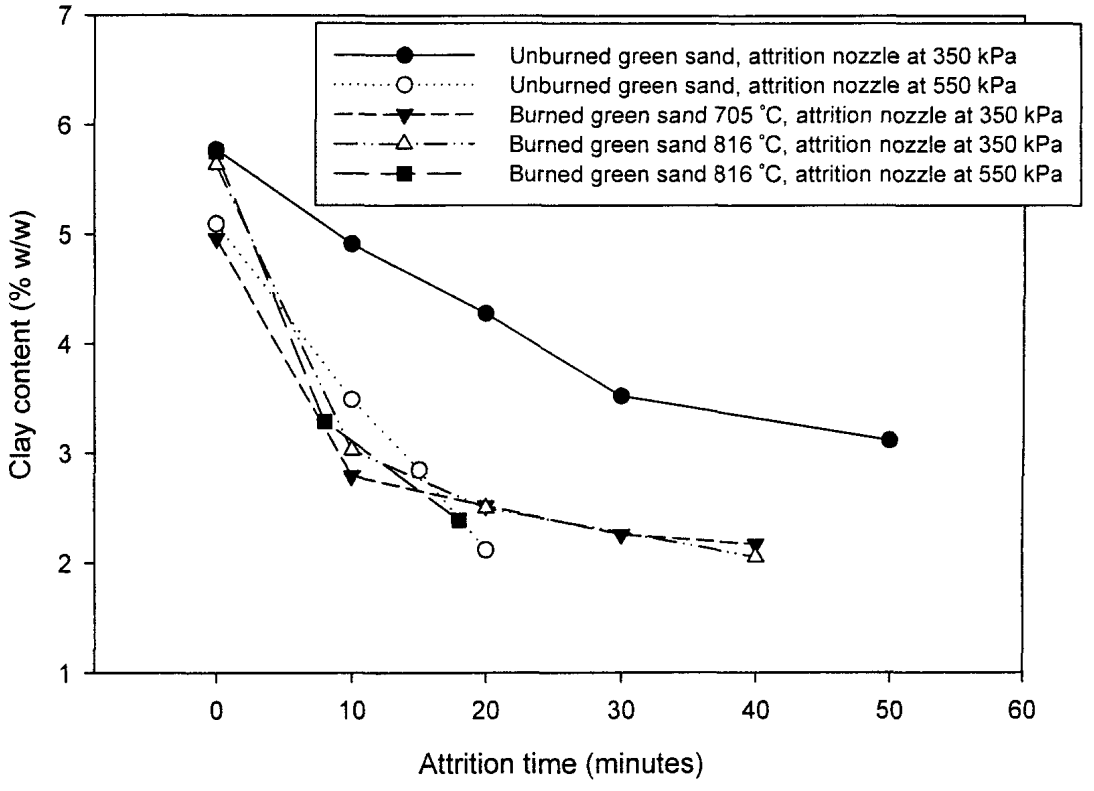

Figure 2.14: Clay content in samples taken from the bed, Foundry B green sand.

Figure 2.15 shows the clay content results for fines collected in the cyclone. These fines were produced while attriting unburned and burned (at 705 °C) green sand with an attrition nozzle pressure of 350 kPa. The clay content of the fines was much higher for unburned sand. One possible explanation may be that for unburned green sand, the chemical structure of the clay is almost intact while for calcined green sand most of the clay has been transformed into oxide compounds, and these particles are not easily trapped in the cyclone and, therefore, are lost in the exhaust system.

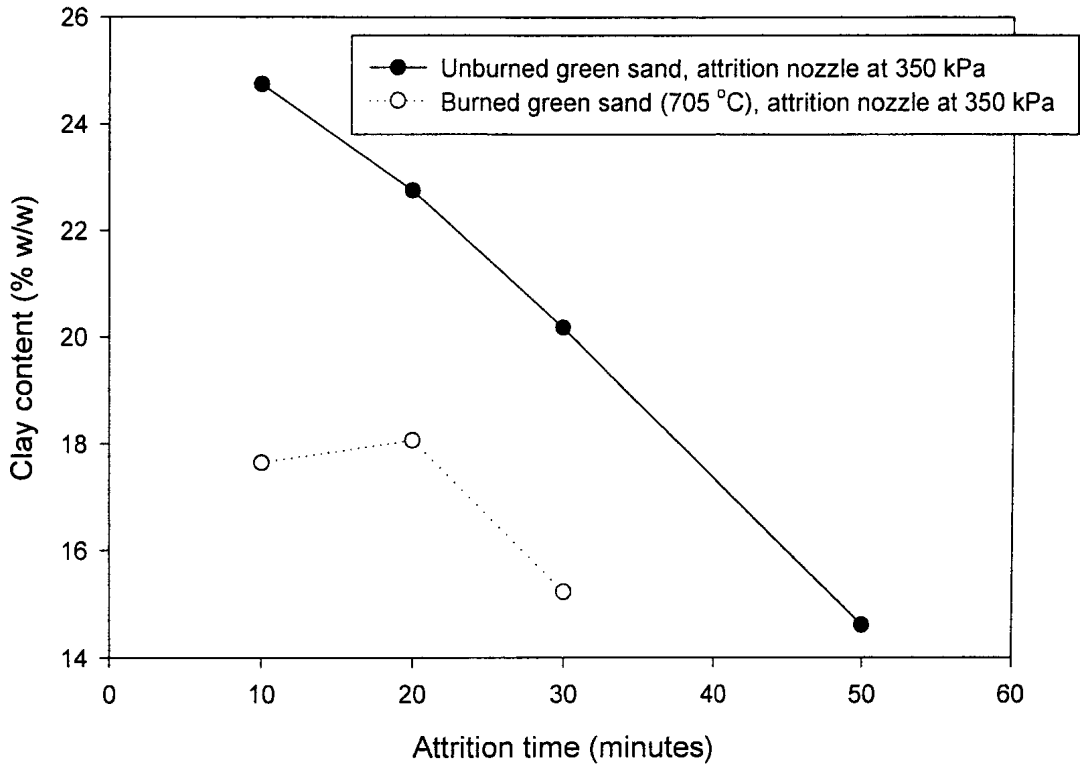

Figure 2.15: Clay content in fines collected in the cyclone for unburned and burned Foundry B green sand.

Calcining the samples at a temperature of around 700 °C may eliminate the organic content of the green sand. If unburned samples of green sand are attrited, the organic content decreases to near 1 wt% as shown in Figure 2.16. As with the clay content, using an attrition nozzle pressure of 550 kPa at the attrition nozzle speeds up the removal of organic matter.

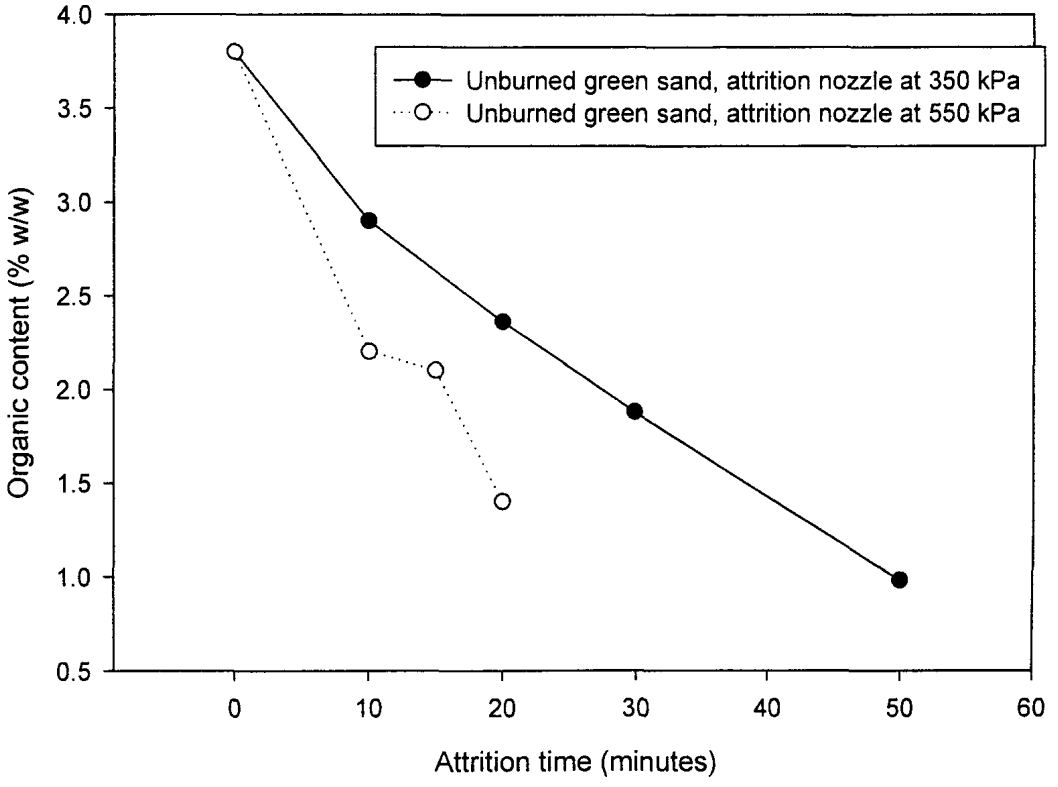

Figure 2.16: Organic content in unburned Foundry B green sand, bed samples.

When the untreated green sand is burned, the acid request is reduced. Also, the best acid request values after attrition are achieved on calcined green sand, as it can be seen in Figure 2.17. Figure 2.17 shows that the lowest acid request value is achieved by burning at 816 °C, and then attriting for 18 minutes at 550 kPa.

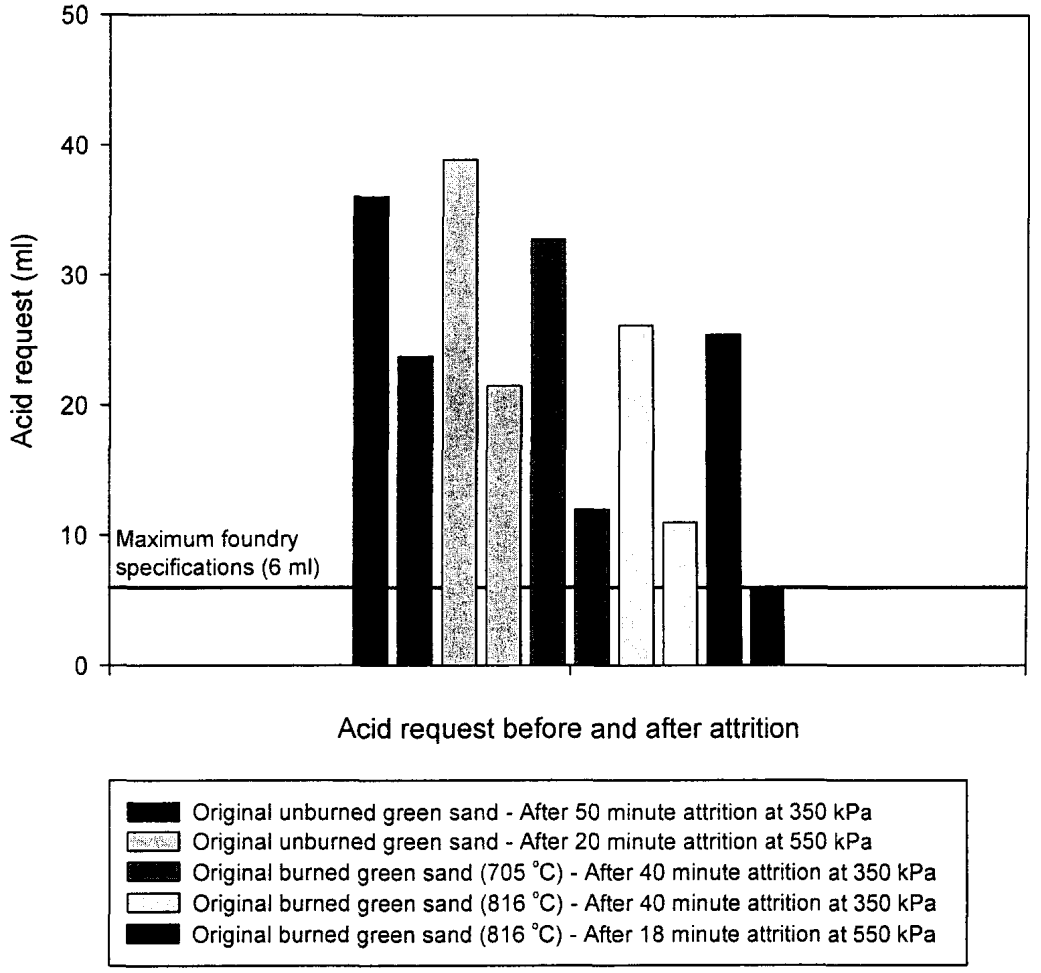

Figure 2.17: Acid request results for original Foundry B samples and after attrition samples.

As mentioned earlier, when using an attrition nozzle pressure of 550 kPa for unburned green sand, the results obtained for clay content are similar to the results for calcined green sand. However, one potential disadvantage of using higher air pressure in the attrition nozzle is that the losses in bed volume increase as it is shown in Figure 2.18, and, eventually, undesirable fragmentation attrition will predominate. The bed volume change is not a perfect indicator of mass lost during attrition since it results from a combination of changes in bed mass and in the green sand apparent density.

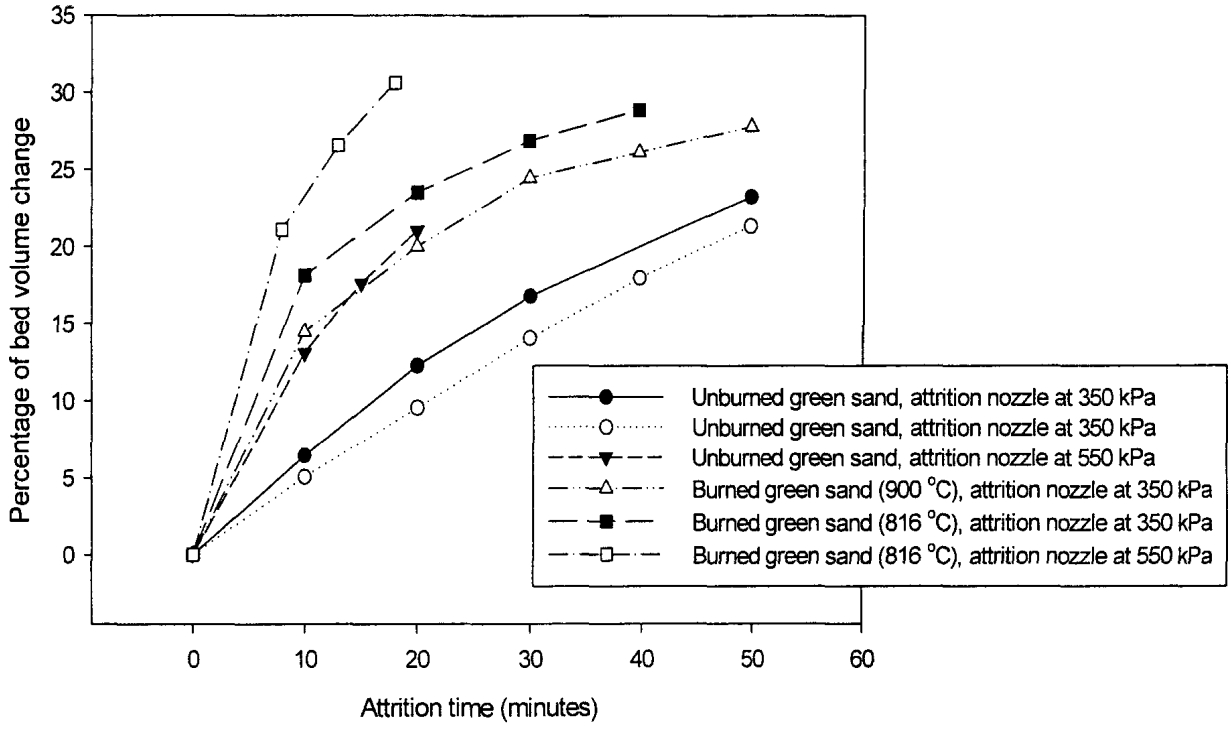

Figure 2.18: Bed volume change while attriting unburned and burned Foundry B green sand.

To obtain a better estimate of the mass lost during attrition, the fines in the cyclone were collected and weighted after every attrition interval. Figure 2.19 shows the amount of fines collected in the cyclone within each attrition interval, and it is found that the highest amount of collected fines corresponds to green sand that was burned at 816 °C and attrited at 550 kPa.

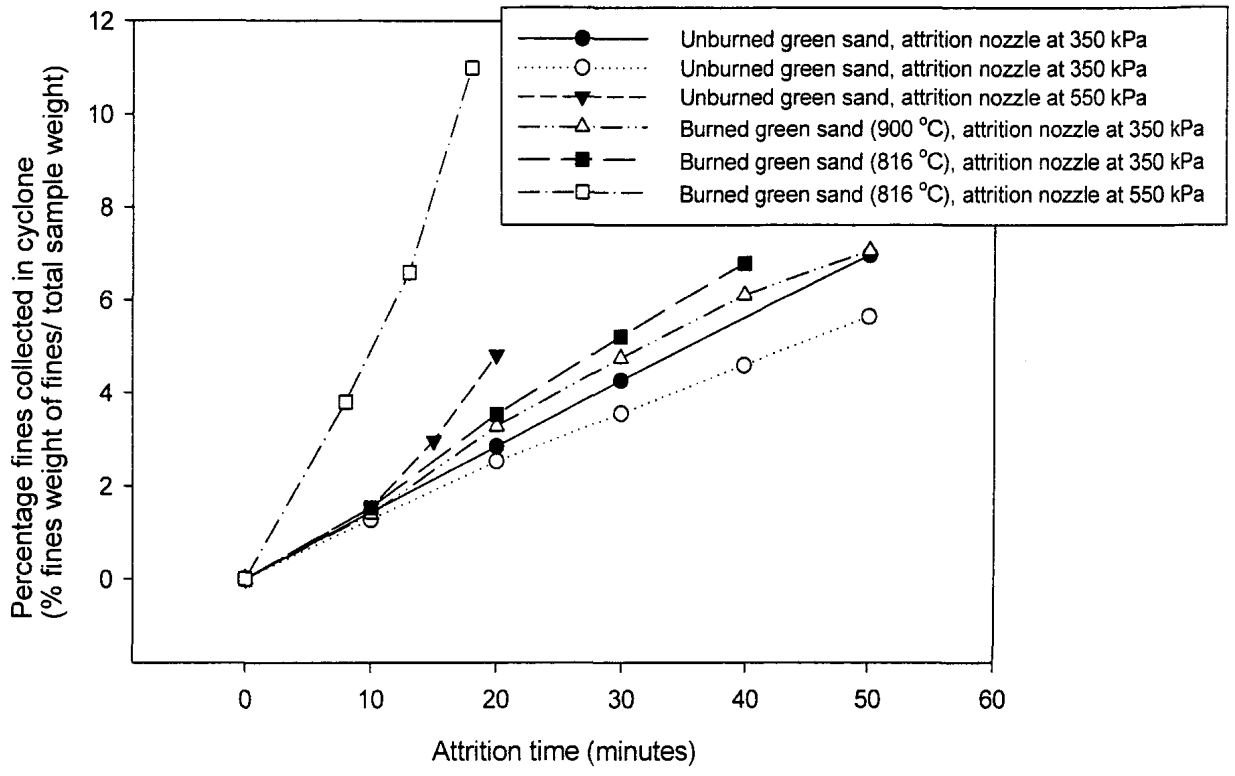

Figure 2.19: Fines collected in the cyclone at each attrition interval (Foundry B green sand).

Table 2.1 summarizes a mass balance for the attrition run that used burned green sand (Foundry B) at 816 °C and attrited with an attrition nozzle pressure of 550 kPa.

According to the results from the mass balance, 14% of green sand mass is lost during attrition, and this accounts for both fines collected in the cyclone (11 wt %) and particles that escape the cyclone and are lost to the exhaust system (3%). This value of 14% mass loss greatly differs from the 30.7% volume change for the same attrition run as a result of the variation in green sand apparent density during attrition.

Table 2.1: Mass balance for the attrition run with burned green sand (816 °C) and an attrition nozzle pressure of 550 kPa (Foundry B).

	Weight (g)
Initial green sand in the bed	10400
Samples collected from the bed	353
Weight after samples taken	10047
Fines collected in cyclone	1069
Green sand collected from bed after attrition	8655
wt % lost (fines in cyclone + lost particles)	14
wt % fines collected in cyclone	11
wt % lost particles to the exhaust system	3

To try to find the best attrition conditions, a clay removal efficiency is established. This efficiency is the ratio of the percentage of clay removed to the percentage of bed volume change. Figure 2.20 gives the results for different attrition runs, and the best efficiencies are obtained when attrition is performed on unburned green sand with an attrition nozzle pressure of 550 kPa. However, one disadvantage of these conditions is that the acid request is unacceptable high (around 20 ml) when compared to the maximum required value of 6 ml.

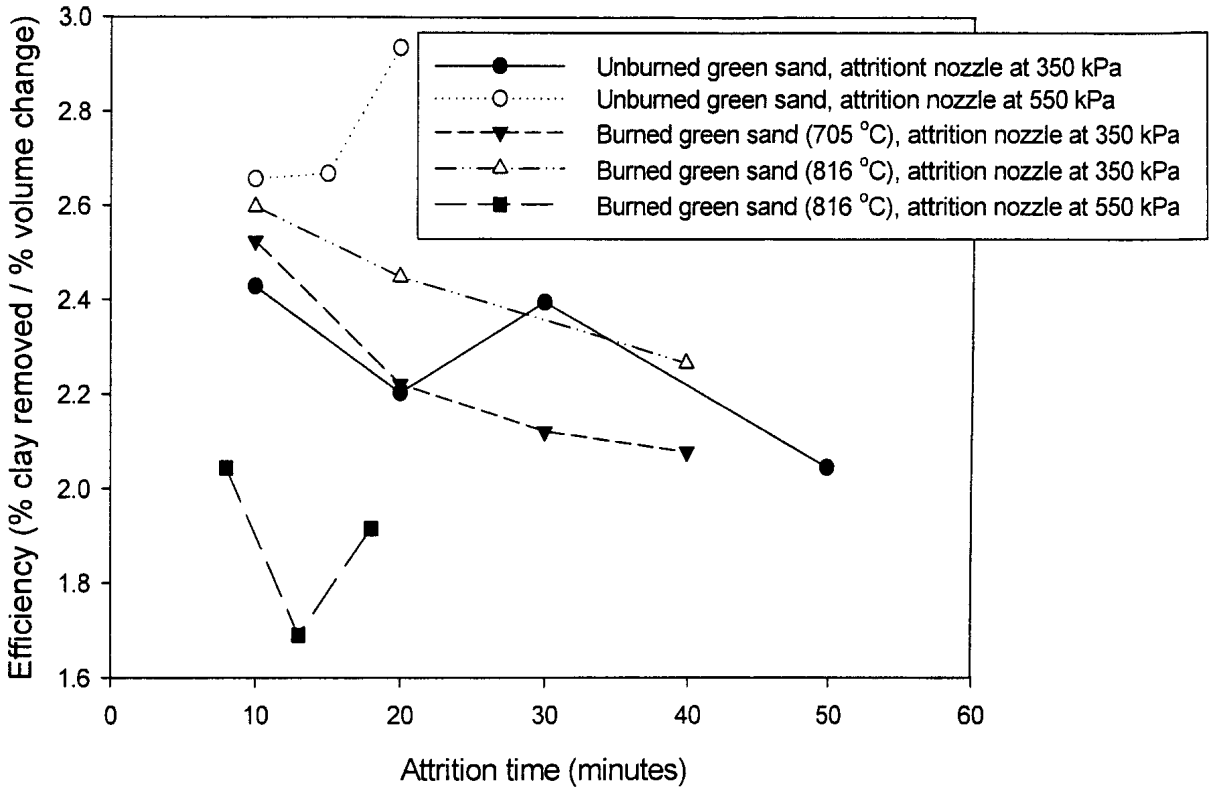

Figure 2.20: Clay removal efficiency (Foundry B).

Finally, the volumetric flow rate of air required to feed the attrition nozzle, when operating at 550 kPa, and to attrit 3000 kg/hr of green sand is around 0.236 m^3/s at standard conditions (500 SCFM). Our results indicate that a reasonable attrition time for green sand is about 5 minutes, and the mass of air consumed per kg of green sand is, thus, about 0.34 kg air/kg green sand. To obtain this amount of compressed air, the energy required is approximately 100 kWh. This may be a drawback of this method for the removal of clay from the green sand and the next section, therefore, compares its cost to the calcination cost.

In the case of green sand calcination, some companies manufacture equipment to carry out the thermal reclamation where the organic binders in the chemically bonded foundry sands is burned up at temperatures close to 700 °C. It is reported by one of these companies (Gudgeon Brothers), that approximately 0.034 m^3 of natural gas are required to heat up one kg of silica sand mixed with organic binders from ambient temperature to

around 700 °C, and the calcination equipment consumes nearly 53 kWh per ton of sand processed. Table 2.2 shows an approximate calculation of the energy that may be required to process the green sand. It is seen in this table that around 88 kWh and 34 m^3 of natural gas are needed if one ton per hour of green sand is to be calcinated and attrited, and the cost of this energy is roughly US$ 23. Besides these energy costs, there are additional expenses, associated with equipment, installation and maintenance, and labor. According to different sources (American Foundry Society and Opta Minerals Inc.), prices for new silica sand may vary from US$ 40 to US$ 140 per ton, and disposal costs for green sand also vary widely depending on the form of disposal. From the previous analysis, calcination and attrition may be an economically feasible method. However, currently there is no industrial scale equipment that reclaims green sand using an attrition nozzle on calcinated green sand and, therefore, no data is available about the final quality of reclaimed green sand. Results from this study might differ from the ones that could be obtained by performing calcination and attrition simultaneously since attrition tests reported in this work were conducted at ambient temperature.

Table 2.2: Estimation of energy required to process one ton of green sand using attrition and calcination.

	kWh per ton of green sand	**kWh cost (US$)**	**Total cost (US$)**
Attrition gas compressor	35	0.05	1.8
Calcination equipment	53		2.6
Total kWh	**88**		**4.4**
	m^3 natural gas per ton of green sand	**m^3 cost (US$)**	
Natural gas for calcination	34	0.41	**13.9**
	Total energy cost per ton of green sand		**22.7**

2.5 Conclusions

Using an attrition nozzle in a fluidized bed may be a good method to reclaim green sand for core making use. Good results for clay content are achieved when attriting unburned green sand with a nozzle pressure of 550 kPa, but the acid request value is around 20 ml, which is still very high for core making applications. The maximum desired value is 6 ml.

Attriting calcined green sand, on the other hand, produces the best results. As expected, after calcination, the organic content of the green sand is almost zero. Removing the clay from calcined green sand is faster, and the lowest clay content achieved is around 2 % w/w. Acid request values are much better for burned green sand, and the best value is close to 6 ml when using an attrition nozzle pressure of 550 kPa .

According to the mass balance, the mass lost during the attrition process could be around 14%, and this may be considered acceptable.

Although the attrition nozzle requires a high gas flowrate, calcination of green sand seems much more energy intensive and expensive. The combined cost of attrition and calcination is around US$ 0.023/kg, and new silica sand price is between US$ 0.04/kg and 0.14/kg depending on its quality. Once disposal costs of green sand are added, the proposed method appears economically attractive.

2.6 References

Hulet, C., McMillan, J., Briens, C., Berruti, F., and Chan, E.W., "Visualization of the Effect of a Shroud on Entrainment of Fluidized Solids into a Gas Jet". *Int. J. Chem. React. Eng.*, **5** S4 (2007).

McMillan, J., Briens, C., Berruti, F., and Ed, C., "Particle Attrition Mechanism with a Sonic Gas Jet Injected into a Fluidized Bed", *Chem. Eng. Sci.*, **62** 3809-3820 (2007b).

Strobl, S.M., "The Fundamentals of Green Sand Preparation and Control", *Simpson Technologies Corporation*, Aurora, Illinois, USA (2000).

Strobl, S.M., "*Controlling Green Sand Carbons*", *Modern Casting*, June 1, 1994.

Zanetti, M.C., and Fiore, S., "Foundry Processes: The Recovery of Green Moulding Sands for Core Operations", *Resour. Conserv. & Recy.*, **38**, 243-254 (2002).

Zanetti, M.C., and Godio, A., "Recovery of Foundry Sands and Iron Fractions from an Industrial Waste Landfill", *Resour. Conserv. & Recy.*, **48** 396-411 (2006).

Websites

First (Foundry Industry Recycling Starts Today), What is recycled foundry sand? http://www.foundryrecycling.org/Home/tabid/36/Default.aspx

AFS (American Foundry Society), The Foundry Industry...Recycling Yesterday, Today and Tomorrow. http://www.afsinc.org/images/stories/govaffairs/recyclingbrochure_lr.pdf

Private information sources

Gudgeon Brothers.

Opta Minerals Inc.

CHAPTER 3

Supersonic Attrition Nozzles in Gas-Solid Fluidized Beds

3.1 Introduction

Some industrial applications of gas-solid fluidized beds require a control of the size distribution of the particles in the bed in order to maintain good fluidization, and the fluid coking process is an example where this need is critical. Fluid coking is used to produce synthetic crude oil by thermal cracking of the bitumen extracted from the oil sands. Coke particles with a specific particle size distribution are used for fluidization, and during the thermal cracking process the particle size of these coke particles increases gradually due to the deposition of coke produced in the reaction. The coke particles also agglomerate when several coke particles stick together due to poor feed distribution. Large coke particles will induce slugging and poor circulation, while too many fine particles with a diameter smaller than 70 μm will cause agglomeration leading to poor fluidization (McMillan et al., 2007). Supersonic attrition nozzles are used to control the coke particle size distribution by injecting superheated steam through specially designed nozzles to produce an attrition jet inside the bed, which entrains coke particles accelerating them at high speed so that they hit slow moving bed particles located near the tip of the jet cavity formed by the injected steam. These supersonic nozzles are more efficient than subsonic nozzles to control the size of the bed particles (McMillan et al., 2007).

Particle to particle collisions near the jet tip reduce the particle size through two main mechanisms of attrition: abrasion and fragmentation (McMillan et al., 2007). Abrasion occurs when fines are removed from the surface of the original particles. This attrition mechanism generates many fines, and the particle size distribution of the original particles remains nearly constant. In the fragmentation mechanism, the particles break into large pieces. For silica sand, abrasion is predominant at low grinding pressures, and fragmentation takes place at high attrition pressures (Palaniandy et al., 2008). Figures 3.1 and 3.2 show these two attrition modes. It is also found that the amount of fine particles produced and the grinding efficiency increase with higher attrition pressures (McMillan et al., 2007; Midoux et al., 1999). The grinding efficiency for this research is defined as the new surface area created during attrition per mass of attrition gas used and measured in m^2/kg (McMillan et al., 2007).

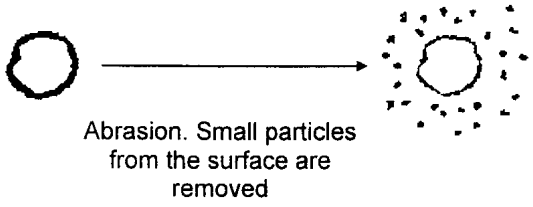

Figure 3.1: Particle abrasion mechanism.

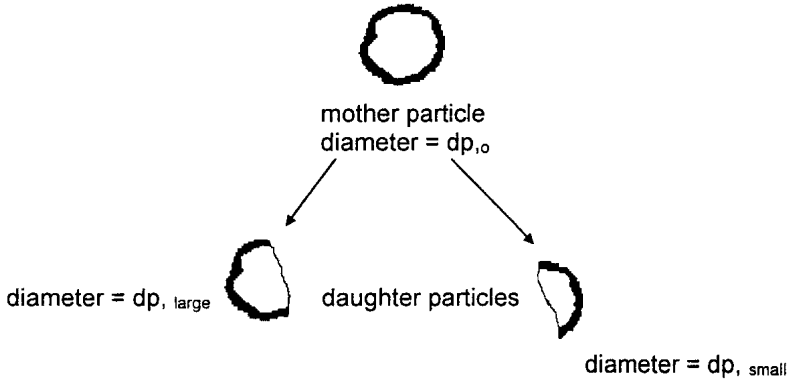

Figure 3.2: Particle fragmentation mechanism (Adapted from McMillan et al. 2007).

Some researchers have found (Werther and Xi, 1993; Ghadari et al., 1994; Shamlou et al., 1990; Arastoopour and Chen, 1983; Lin et al., 1980; Stein et al., 1998) that, in fluidized bed processes, attrition may be caused by grid jets, gas bubbles and cyclones and they have presented models to calculate attrition rates. Other researchers studied the jet attrition of catalyst particles to predict the attrition caused by gas distributors, and they found that the attrition rate was proportional to the attrition gas density, the orifice diameter and the jet exit velocity (Werther and Xi, 1993). The following equation was presented to calculate the jet attrition rate (kg/s) (Werther and Xi, 1993):

$$R_{a,j} = K\rho_{gd} d_{gd}^2 U_{gd}^3 \tag{3.1}$$

where K is the attrition gas constant and refers to the properties of the attrited material and ρ_{gd}, d_{gd}, and U_{gd} are the gas density, orifice diameter and gas velocity at the distributor.

For this study, the previous attrition effects are not taken into account since these effects, in the equipment used, may be considered negligible when compared with the attrition produced by a supersonic attrition jet.

The main variables affecting the attrition process can be divided in properties of the particles and properties of the environment (Patel et al., 1986). Particle properties include size, shape, surface roughness and strength. Fluidization velocity, height of the bed, pressure, temperature and humidity are some of the key properties of the environment. The fines produced during attrition have also been found to reduce the breakdown rate by providing an additional cushioning effect (Forsythe and Hertwig, 1949).

One disadvantage of jet grinding, as other grinding processes, is its high energy consumption, since only about 2% of the energy provided is used to create new surfaces (Mebtoul et al., 1996). Therefore, it is critically important to optimize the supersonic nozzles used for grinding particles, and this is the main the objective of the present study.

The next section reviews the equations and concepts such as thrust and equivalent velocity that have been traditionally applied to supersonic nozzles in the aeronautics field.

3.2 Modeling of Laval supersonic nozzles

Thrust is typically defined in the aeronautics field as the force produced by a rocket propulsion system acting upon a vehicle (Sutton and Biblarz, 2001). In the present study, thrust can be interpreted as the reaction force created by the ejection at high velocity of attrition gas from the supersonic nozzle. The equivalent velocity is the thrust divided by the mass flow rate of the gas exiting the nozzle.

To calculate the thrust and the equivalent velocity of the supersonic jet, compressible, isentropic flow of a perfect gas is assumed. This means that friction and heat transfer are not considered, and variations in gas properties are caused by the variation in cross-sectional area. One-dimensional, steady flow is also assumed, and, for gas flows, changes in potential and gravitational forces are neglected (John and Keith, 2006). Figure 3.3 represents a Laval-type convergent divergent nozzle that could be used for particle attrition.

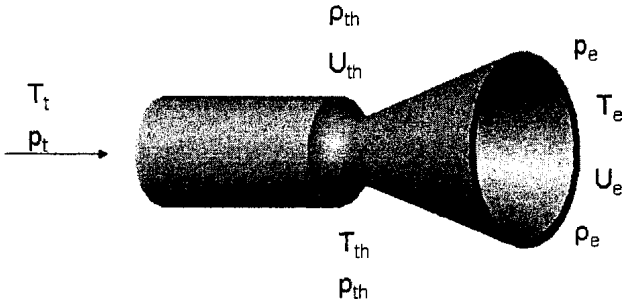

Figure 3.3: Convergent-divergent (C-D) Laval-type nozzle showing different gas properties at the exit and at the throat.

The equations required to calculate equivalent velocity and thrust are presented in table 3.1 (John and Keith, 2006):

Table 3.1: Calculation of different properties for the Laval-type nozzle.

Property	Equation
Mass flow rate (3.2)	$\dot{m} = A_{th} p_t \sqrt{\frac{\gamma}{T_t R}\left(\frac{\gamma+1}{2}\right)^{\frac{\gamma+1}{2(1-\gamma)}}}$
Exit Mach (3.3)	$\frac{A_e}{A_{th}} = \frac{1}{M_e}\left[\left(\frac{\gamma+1}{2}\right)\left(1+\frac{\gamma-1}{2}M_e^2\right)\right]^{\frac{\gamma+1}{2(\gamma-1)}}$
Exit temperature (3.4)	$\frac{T_e}{T_t} = \left(1+\frac{\gamma-1}{2}M_e^2\right)^{-1}$
Exit pressure (3.5)	$\frac{p_e}{p_t} = \left(1+\frac{\gamma-1}{2}M_e^2\right)^{\frac{\gamma}{1-\gamma}}$
Exit density (3.6)	$\frac{\rho_e}{\rho_t} = \left(1+\frac{\gamma-1}{2}M_e^2\right)^{\frac{1}{1-\gamma}}$
Exit velocity (3.7)	$U_e = M_e\sqrt{\gamma R T_e}$
Thrust (3.8)	$F = \dot{m}U_e + (p_e - p_o)A_e$
Equivalent velocity (3.9)	$U_{eq} = U_e + \frac{(p_e - p_o)A_e}{\dot{m}}$

The variations of pressure, temperature, density, and Mach number with cross-sectional area through a convergent-divergent nozzle are illustrated in Figure 3.4, and it is seen that pressure decreases faster than temperature and density.

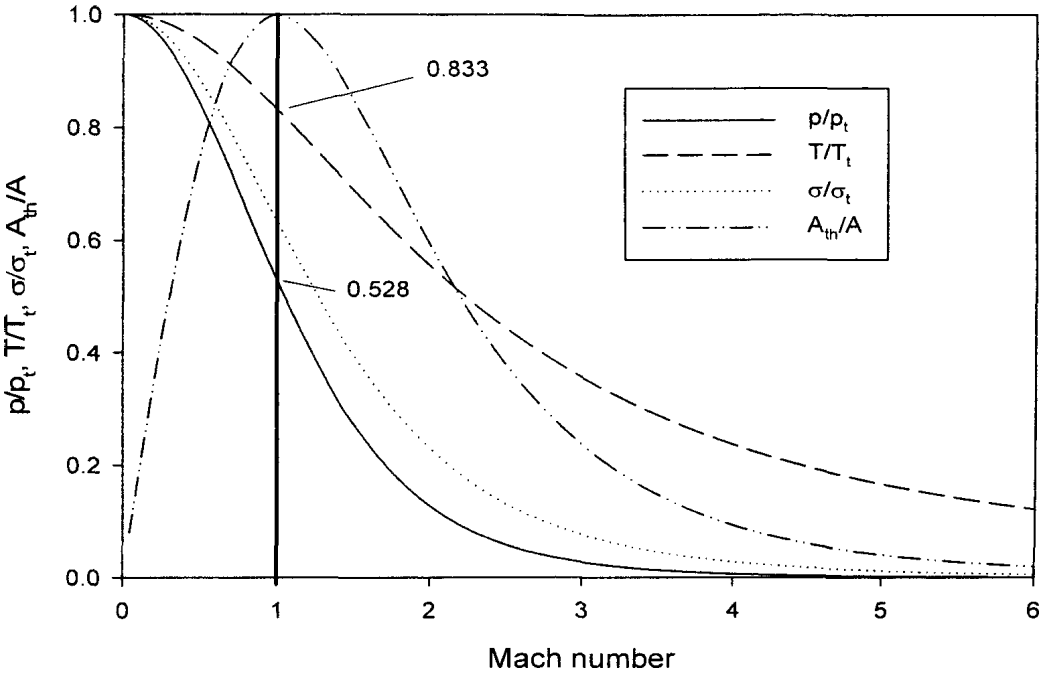

Figure 3.4: Variation of pressure, temperature, density, and Mach number with cross-sectional area through a convergent-divergent nozzle.

Three previous studies used the Laval-type nozzle (McMillan et al., 2007; Benz et al., 1996; Mebtoul et al., 1996), but they did not relate thrust or equivalent velocity with grinding efficiency. It is expected that the Laval-type nozzle was used because this nozzle can produce supersonic velocities, and Equations 3.2 to 3.9 show that to achieve this, the gas must change its temperature and pressure through the nozzle so it will be reasonable to use these equations to calculate the gas properties at different locations, especially at the nozzle tip where there is the first contact between the attriting gas and the fluidized bed particles. It is found that the slope of the curve that represents the variation of the mean particle velocity versus the air velocity at the nozzle exit has an abrupt change at the transition point from subsonic to supersonic flow in the divergent section of the nozzle (Mebtoul et al., 1996).

An abrupt nozzle, similar to the convergent–divergent nozzle but without the divergent section, was used for grinding experiments (Midoux et al., 1999), and the grinding power supplied as gas kinetic energy for sonic nozzles was expressed by:

$$\dot{E}_k = \frac{1}{2}\dot{m}U_s^2 \tag{3.10}$$

The grinding pressure is directly correlated to kinetic energy of the gas and, therefore, to the energy transmitted to particles for grinding (Midoux et al., 1999). It is also stated that an increase in momentum gives an increase in grinding efficiency (McMillan et al., 2007).

Figure 3.5 illustrates the pressure distribution along the Laval-type nozzle, depending on the total inlet pressure (p_t) and the background pressure (p_o) (John and Keith, 2006).

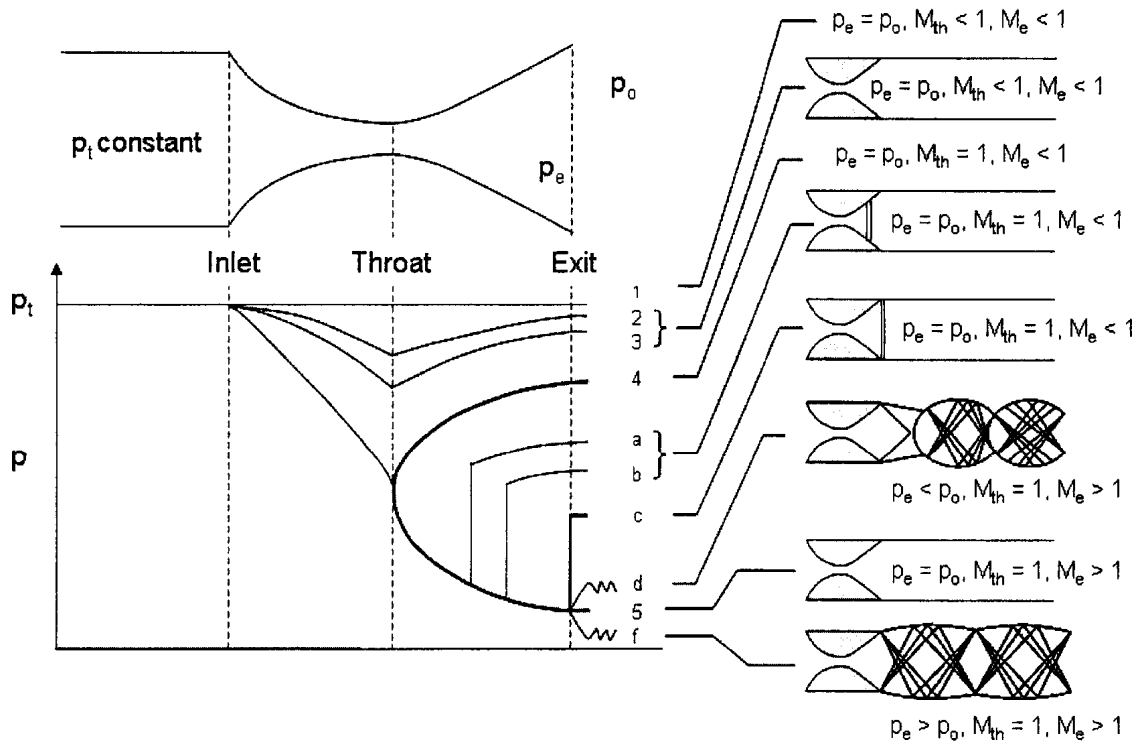

Figure 3.5: Pressure distribution in a convergent–divergent nozzle. Adapted from John and Keith (2006).

To analyze this Figure, we could first consider that p_o is set equal to p_t, and, given this initial condition, there would be no flow in the nozzle. When the backpressure starts decreasing below the total pressure, subsonic flow is induced through the nozzle. In the subsonic flow, the pressure decreases up to the throat section and then increases in the

divergent section of the nozzle or, in other words, the pressure is minimum at the throat. These are conditions 2 and 3 in Figure 3.5. As the back pressure is further reduced, eventually sonic flow occurs at the throat, and this is represented with curve 4. At this point, the flow through the nozzle remains constant with further reductions in the back pressure. If the back pressure is reduced below curve 4, a normal shock is formed in the nozzle just downstream of the throat (curve a). By lowering further the backpressure, this normal shock is pushed farther downstream (curve b). At some point the shock will be located at the nozzle exit plane (curve c). When the pressure is reduced beyond that of curve c, a shock wave appears, and this wave is inclined at an angle at the exit plane of the nozzle. This discontinuity is called and oblique shock and it is weaker than a normal shock (John and Keith, 2006). At this stage the backpressure is higher than the nozzle exit pressure and the nozzle becomes overexpanded.

If the backpressure is reduced even further, the angle between the oblique shock and the flow decreases, as well as its strength, until the design condition is reached, and this is represented by curve 5. At the design condition, the backpressure is equal to the nozzle exit pressure, and the flow is perfectly uniform. If the backpressure is reduced below curve 5, the exit plane pressure will be greater than the backpressure, and the pressure outside the nozzle will be reduced in the form of expansion waves, and with these conditions the nozzle becomes underexpanded. Cases 4, c and 5 in Figure 5 represent transitions between the subsonic to sonic flow at the throat, the formation of normal shocks from the throat to the nozzle exit, and the overexpanded and underexpanded flows, respectively (Chapman, 2000).

It is important to mention that for all backpressures below curve c, the flow downstream the exit plane adjusts to the backpressure outside the nozzle, and the flow inside the nozzle remains unchanged. Figure 3.6 shows how the nozzle exit pressure and the backpressure are related in a convergent–divergent nozzle (John and Keith, 2006).

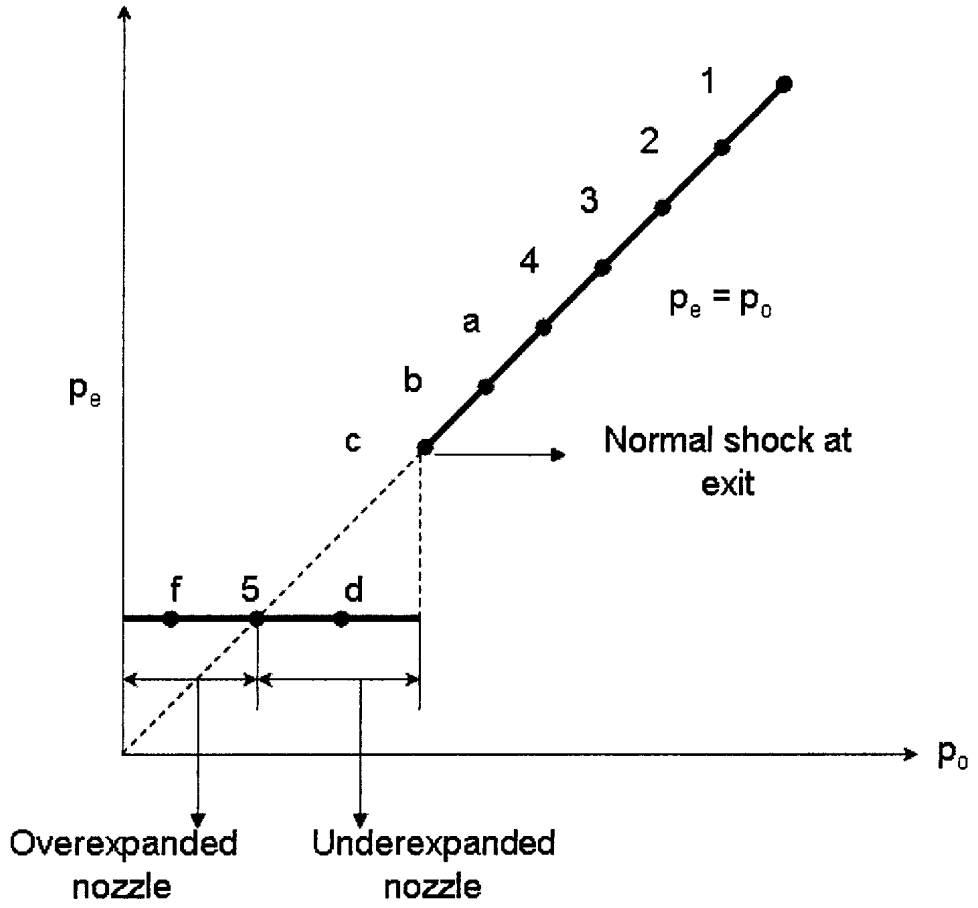

Figure 3.6: Exit pressure versus backpressure for a convergent-divergent (CD) nozzle. Adapted from John and Keith (2006) (points 1, 2, 3, 4, a, b, c, d, 5 and f corresponds to the similarly named cases in figure 5)

To obtain the highest possible thrust from a convergent-divergent nozzle, there are some constraints in its design, especially for the divergent section. If the angle of the divergent section is too large, shocks will form and energy will be dissipated, and if the divergence angle is too small, excessive friction will occur (Perry et al., 1997). Besides, there is a theoretical correction factor λ that can be applied to a convergent-divergent nozzle with a conical divergent section when friction of the gas on the nozzle wall is considered negligible. This factor represents the ratio between the momentum of the gases in a nozzle with a finite nozzle angle, and the momentum of an ideal nozzle with all the gases flowing in an axial direction (Sutton and Biblarz, 2001):

$$\lambda = \frac{1}{2}(1+\cos\alpha) \tag{3.11}$$

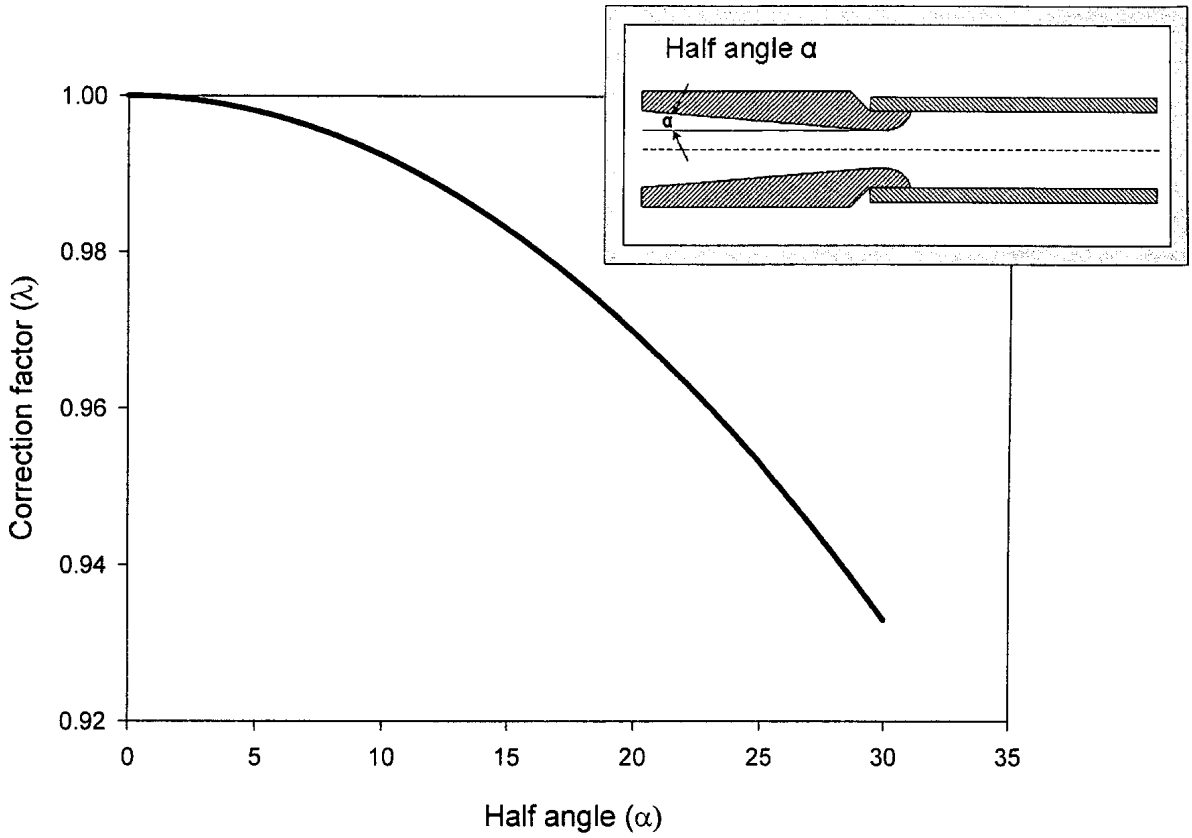

Figure 3.7: Nozzle angle correction factor for conical nozzles.

It is seen in Figure 3.7 that for half angles more than 5°, the axial momentum losses increase drastically.

To account for friction effects in a convergent-divergent nozzle, Mach number, pressure, and temperature are calculated with Equations 3.12 to 3.14 (Abdulhadi, 1988).

Mach number:

$$\gamma M^2 \frac{f}{2D} = \frac{2dD}{Ddx} + \frac{2(1-M^2)}{M[2+(\gamma-1)M^2]}\frac{dM}{dx} \tag{3.12}$$

For temperature:

$$\frac{1}{T}\frac{dT}{dx}=\frac{2(\gamma-1)M^2}{(1-M^2)D}\frac{dD}{dx}+\frac{\gamma(\gamma-1)M^4 f}{2(1-.M^2)D} \tag{3.13}$$

For pressure:

$$\frac{1}{P}\frac{dp}{dx}=\frac{2\gamma M^2}{(1-M^2)D}\frac{dD}{dx}+\frac{\gamma M^2(1+(\gamma-1)M^2)f}{2(1-M^2)D} \tag{3.14}$$

If the divergent section of the convergent-divergent nozzle is conical, the previous equations become:

Mach number:

$$\frac{dM}{dx}=\frac{(\gamma M^2 f-8\tan\alpha)(M(2+(\gamma-1)M^2))}{4(1-M^2)(D_{th}+2x\tan\alpha)} \tag{3.15}$$

For temperature:

$$\frac{dT}{dx}=\left(\frac{8(\gamma-1)M^2\tan\alpha-\gamma(\gamma-1)M^4 f}{2(1-M^2)(D_{th}+2x\tan\alpha)}\right)T \tag{3.16}$$

For pressure:

$$\frac{dp}{dx}=\left(\frac{\gamma M^2(8\tan\alpha-[1+(\gamma-1)M^2])f}{2(1-M^2)(D_{th}+2x\tan\alpha)}\right)T \tag{3.17}$$

In this work the previous equations have been utilized to describe the flow in convergent-divergent Laval-type nozzles used for particle attrition.

3.3 Experimental set-up

Attrition experiments were performed in a small fluidized bed that was 0.90 m high, and with a 0.1 m by 0.5 m rectangular cross sectional area, as shown in Figure 3.8. For all the experiments 25 kg of silica sand particles with an initial Sauter mean diameter of 200 μm were attrited using air, helium, helium–nitrogen mixture (0.82:0.18 on a molar basis), argon, or carbon dioxide as attrition gases. The tip of the horizontal attrition nozzle was located inside the bed at 0.21 m above the porous plate gas distributor, and 0.03 m from the wall. The bed height was approximately 0.29 m for the static bed, and around 0.34 m when the fluidization velocity was 0.18 m/s. This fluidization velocity was kept constant for all the attrition runs, and the attrition time was set depending on the attrition gas injected by keeping constant its mass. Thus, when the attrition gas was air, argon and carbon dioxide, the mass of gas utilized was always maintained at 2.9 kg for every run, regardless of the attrition gas pressure. The weights of helium, and of the mixture helium- nitrogen mixture were 0.50 kg and 0.75 kg, respectively. All these gases were supplied from high pressure cylinders. The grinding efficiency, η, was defined as the new surface area created during attrition per mass of attrition gas used and measured in (m^2/kg).

The experimental procedure consisted of two stages: the first stage was the actual grinding of the particles, and the second one was the elutriation for 30 minutes of the fine particles generated during attrition. The fluidization velocity for elutriation was kept constant at 0.25 m/s for all the experiments. Elutriation was performed because it was otherwise difficult to get a representative sample from the bed after attrition. In all cases a layer of fine particles appeared at the top of bed, and many of these particles adhered to the bed walls. Although some fines were not collected in the cyclone during both the attrition and the elutriation stages, and were lost in the exhaust air, its impact on the attrition efficiency was negligible and did not affect it by more than 1 m^2/kg.

For the initial experiments many replicates were done to check for the repeatability of the method. After confirmation of the method reliability, duplicates were done for the rest of the experimental runs.

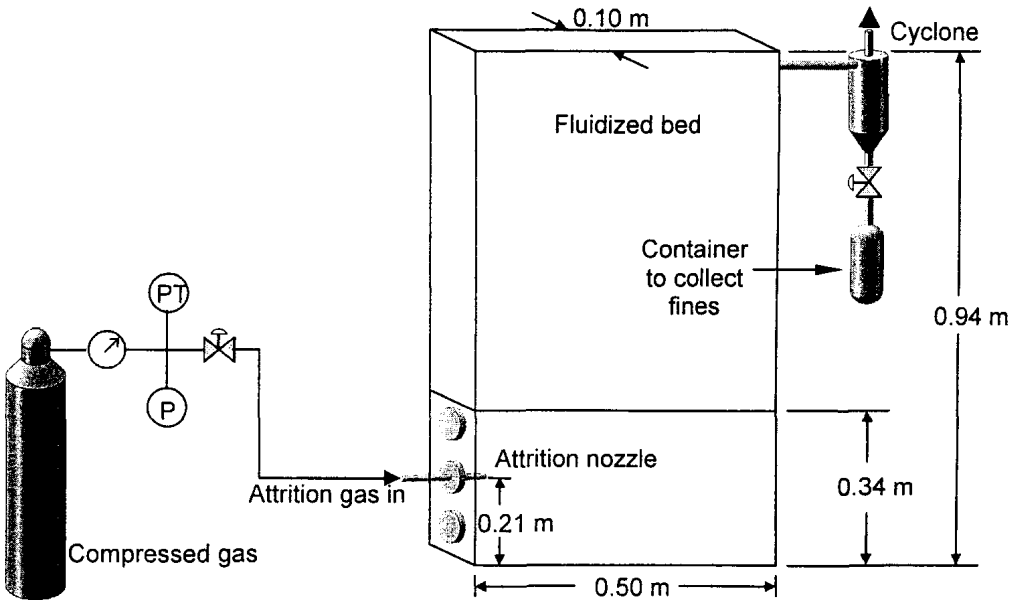

Figure 3.8: Equipment used for the attrition experiments.

For each attrition experiment, the fluidized bed was loaded with 25 kg of silica sand, and the bed was fluidized for 5 minutes to mix the particles. After this, the fluidization gas was suddenly stopped to slump the bed, and particle samples were taken from different locations inside the bed. These samples gave the initial Sauter mean diameter of the bed particles, prior to attrition. The fluidization velocity was then set at 0.18 m/s, and a constant mass of the attrition gas was fed to the attrition nozzle over a period of time calculated depending on the attrition gas and its pressure, as mentioned above. After the attrition was completed, the elutriation step was carried out for 30 minutes. The amount of attrition gas used was also confirmed based on the difference between the initial and the final pressure of the gas cylinder.

After finishing the elutriation, the bed was slumped again, and three random samples were taken. The elutriated fines were collected and weighted. Particle size analysis was carried out, for both coarse and fine bed particles collected using a Mastersizer 2000 Malvern instrument employing a laser diffraction technique.

The attrition gas gauge pressures tested varied between 138 kPa and 2550 kPa (20 psig and 370 psig). Several Laval-type nozzle geometries (convergent-divergent) were investigated and a simple straight nozzle was also used for a few comparative experiments. Nozzles are classified as A1, A2, A3, B, C, D, E, F, G, H and S (Figs. 3.9 to 3.14). Table 3.2 shows the critical measurements and attrition pressures of all the nozzles used during the experiments.

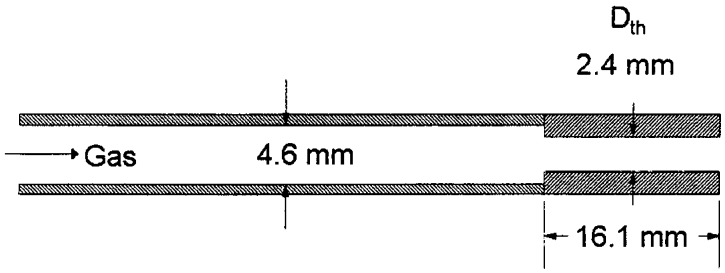

Figure 3.9: Simple straight nozzle, S nozzle.

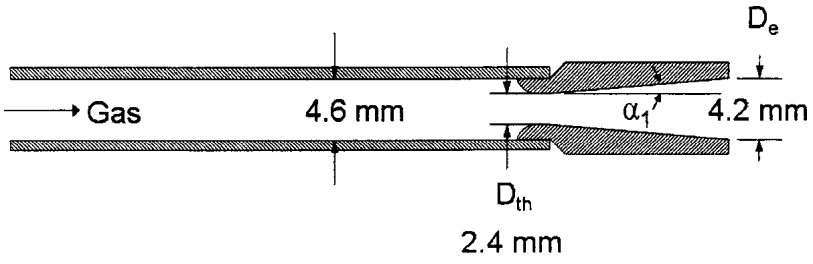

Figure 3.10: A1 nozzle.

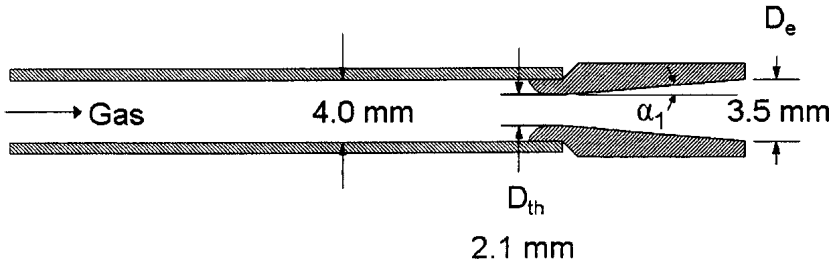

Figure 3.11: A2 nozzle.

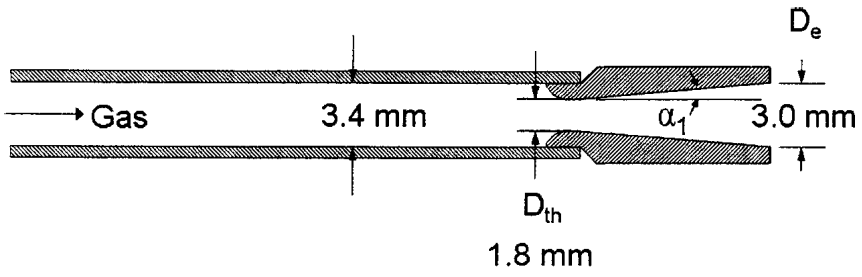

Figure 3.12: A3 nozzle.

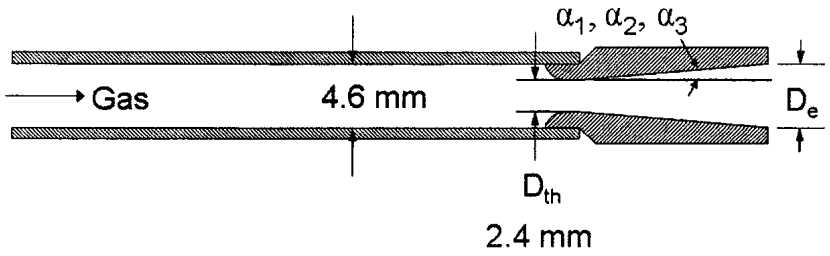

Figure 3.13: B, C, D, E, F, and G nozzles.

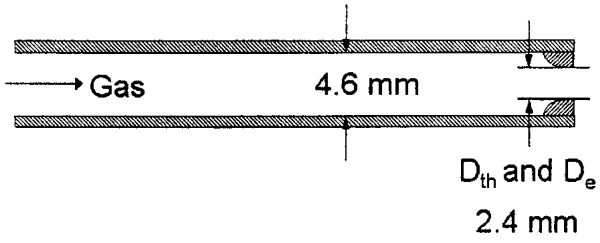

Figure 3.14: H nozzle.

Nozzles A1, A2, and A3 have the same shape, but different throat diameters (2.44, 2.10, and 1.80 mm), and nozzles B to H have different geometries, but with the same throat diameter. The key difference among these nozzles is the length of the divergent section and its half angle. Nozzles A1, A2, A3 and nozzles B, C, D, and E have the same half angle, and nozzle F and G have different ones. The base nozzles for this study are the type A nozzles with a α_1 half angle bigger that the α_2, but smaller than the α_3 half angle. Nozzle H is just equipped with the convergent section.

Table 3.2: Critical measurements of the convergent-divergent nozzles, and attrition pressures used.

Attrition gas	Nozzle Type	Nozzle throat diameter D_{th}(mm)	Nozzle exit diameter D_e (mm)	Half angle α	Upstream pressure kPa (Gauge)
Air	A1	2.4	4.2	α_1	138, 414, 620, 1103, 1275,1930, 2550
Argon	A1	2.4	4.2	α_1	620, 1275, 1930
0.82 He_2/0.18 N_2	A1	2.4	4.2	α_1	620, 1275, 1930
Helium	A1	2.4	4.2	α_1	620, 1275, 1930
Carbon dioxide	A1	2.4	4.2	α_1	1275, 1654
Air	A2	2.1	3.5	α_1	620, 1276, 1930
Air	A3	1.8	3.0	α_1	620, 1276, 1930
Air	B	2.4	4.7	α_1	1103, 1276, 1930, 2550
Air	C	2.4	4.6	α_1	620, 1276, 1930, 2550
Air	D	2.4	2.8	α_1	1103, 1930
Air	E	2.4	3.5	α_1	1103, 1930
Helium	D	2.4	2.8	α_1	1930
Air	F	2.4	3.2	α_2	1103, 1930
Argon	F	2.4	3.2	α_2	1930
Air	G	2.4	5.0	α_3	1103, 1930
Air	H	2.4	–	–	1103
Air	S	2.4	2.4		620, 1103, 1276, 1930

3.4 Results and discussion

3.4.1 Modeling results

The divergent-convergent nozzle may have many different shapes, and some shapes are more efficient than others in producing thrust or equivalent velocities. There are three main factors that may affect thrust and equivalent velocity: friction effects, axial momentum loss, and thrust loss due to the pressure difference between the nozzle exit plane and the background. Equations for friction and axial momentum loss where presented in the introduction section. Figure 3.15 illustrates the results of the numerical solution of the flow equations for different half angles and a friction coefficient equal to 0.005, which is the value for commercial steel pipe with a standard roughness of 0.046 mm (John and Keith, 2006; Perry et al., 1997). It displays the thrust calculated for air at 25 °C, and a total pressure 2170 kPa (300 psig), using the A1 nozzle shape. Figure 3.16 shows the correction factor for different half angles and friction coefficients. This correction factor represents the ratio between the thrust provided by a nozzle with a limited friction coefficient and the thrust of a frictionless nozzle.

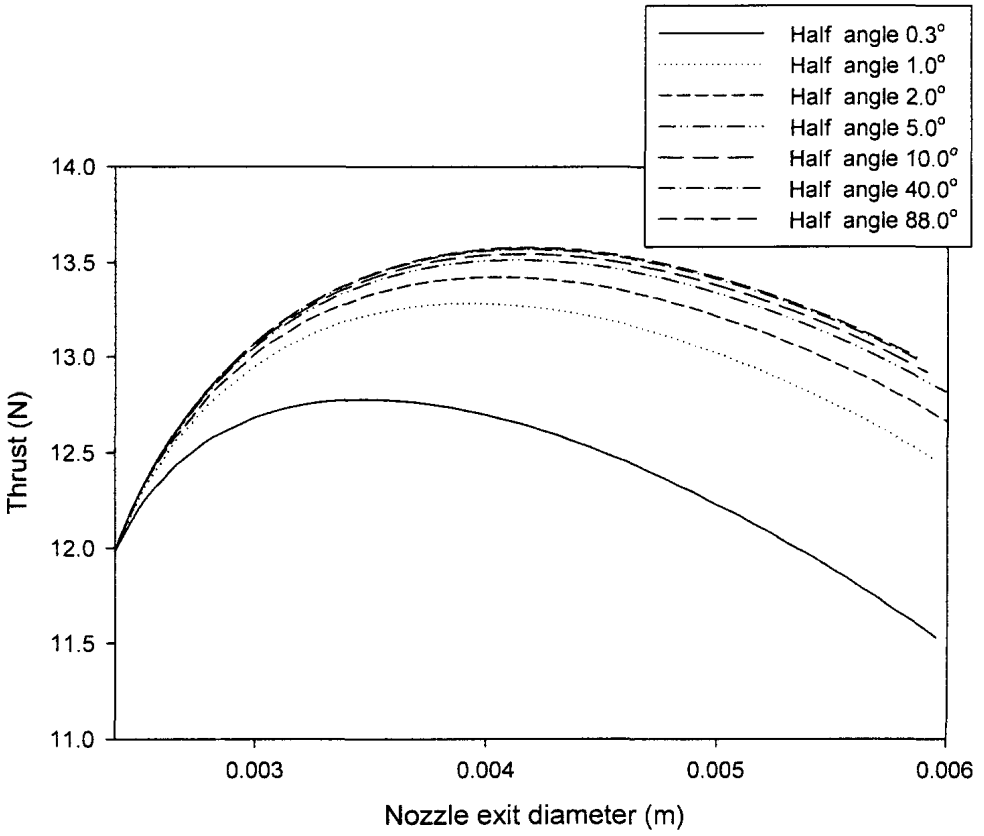

Figure 3.15: Thrust for different nozzle divergent lengths. Nozzle throat diameter 2.4 mm, and friction coefficient (f) 0.005.

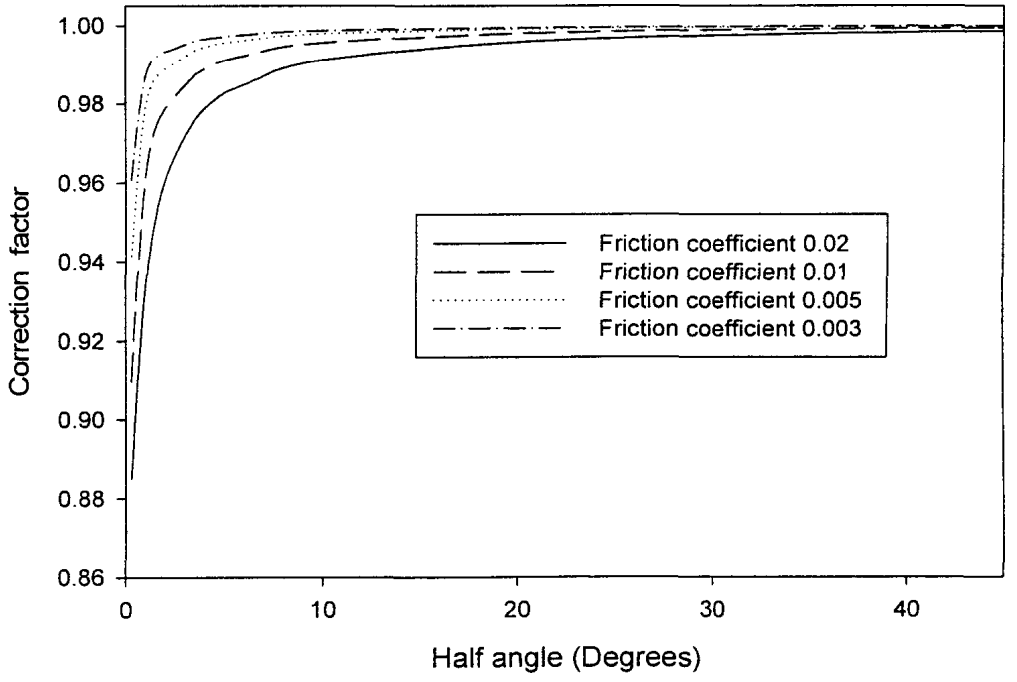

Figure 3.16: Thrust correction factor for different friction coefficients and half angles.

When friction is considered, it is better to have convergent-divergent nozzles with large half angles. However the axial momentum losses increase with the angle since a higher percentage of the exiting flow will be non axial. Figure 3.17 shows the results obtained when combining divergence and friction losses in the thrust calculation. This figure illustrates the correction factor for a friction coefficient of 0.005, which corresponds to standard commercial steel piping, and it shows that the optimum half angle is approximately between 3° and 7.5°, for which the correction factor was greater than 0.99. When the friction coefficient is very high, with a value of 0.02, the optimum angle is around 8.5° and gives a correction factor just over 0.98. On the contrary, if the friction coefficient is very low, e.g. 0.003, an optimum angle between 2° and 9° results in a correction factor of over 0.99.

All the nozzles used in this study were in the optimum half angle range for a friction coefficient of 0.005, and, for this reason, friction and axial momentum losses were neglected. Moreover, it was assumed that thrust losses are caused mainly by the pressure difference between the nozzle exit plane and the background.

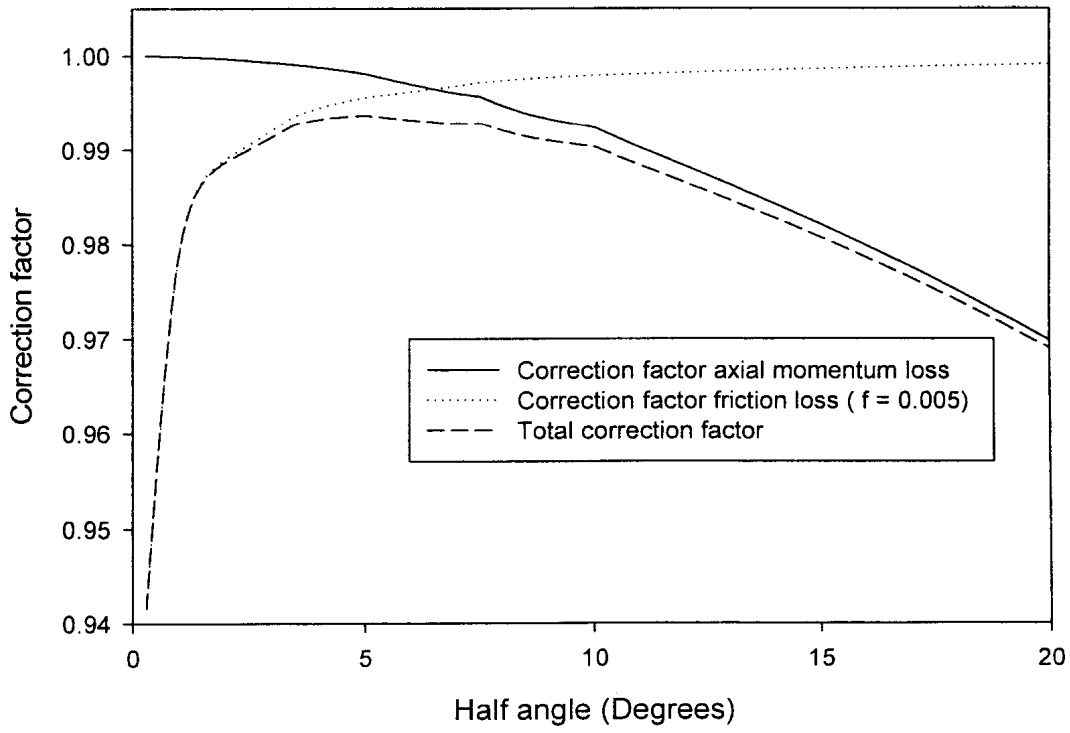

Figure 3.17: Correction factors for thrust lost. Momentum and friction loss, and combined momentum and friction loss (f = 0.005).

3.4.2 Experimental results

This section reviews the experimental results that were obtained in this study. First, it presents the effect of nozzle geometry on grinding efficiency, using air as attrition gas. It then shows the effect of gas composition on grinding efficiency. Finally, a correlation for grinding efficiency is developed.

In the experimental set-up section, it was mentioned that the fines generated during attrition were separated by elutriation. It has been experimentally determined that the Sauter mean diameter of these fines is between 13 and 20 μm, and that the size of the bed particles after elutriation depends on the attrition pressure and varies between 140 and 200 μm approximately. Figure 3.18 shows the particle size distribution of the original silica sand, the coarse particles left in the bed after the elutriation step, and the collected fines. These data refer to an experimental run using the A1 nozzle with injection of air during 220 seconds at a grinding pressure of 1275 kPa (185 psig). For this run the percentage of fines collected was around 2% of the total initial mass of silica sand.

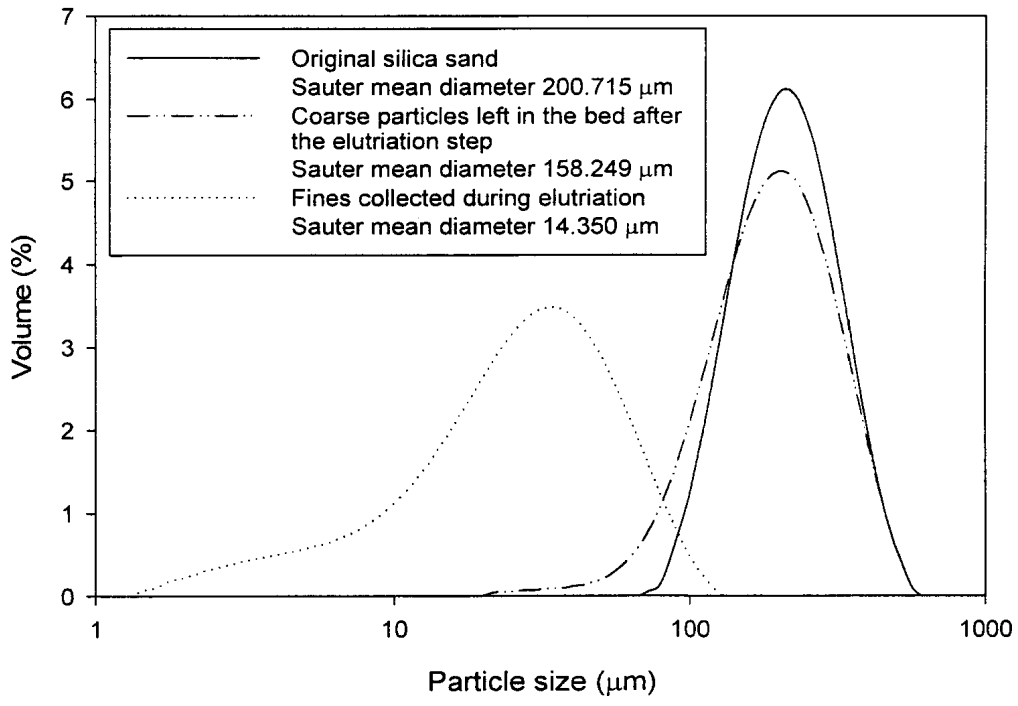

Figure 3.18: Particle size distribution for original silica sand, particles left in the bed after attrition and elutriation and fines collected during elutriation step. Attrition using the A1 nozzle with injection of air at 1275 kPa for 220 seconds.

The relationship between grinding efficiency and attrition pressure (Fig. 3.19) shows that, in general, the grinding efficiency increases with attrition pressure, and the slope of this curve progressively decreases when pressure is increased. However, for the simple straight (S) nozzle the grinding efficiency increases by a relatively small amount for the range of attrition pressures tested. This nozzle does not produce supersonic velocities at its exit, and its grinding efficiency is similar to the other nozzles at low pressures (around 600 kPa), but much lower at high pressures (Fig. 3.19).

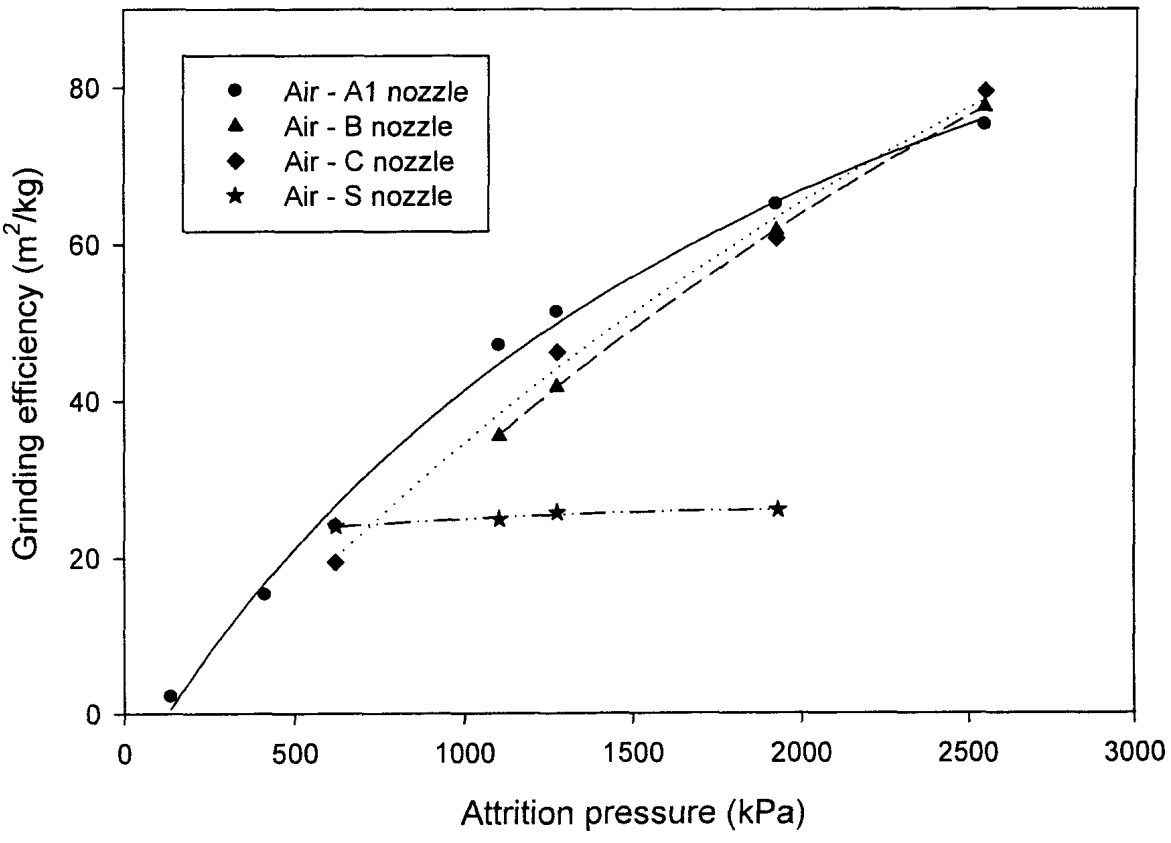

Figure 3.19: Grinding efficiency versus attrition pressure for A1, B, C, and S nozzle types. Air was used for attrition.

Figures 3.20 to 3.22 illustrate the grinding efficiency results when using all the convergent-divergent nozzles and air for attrition. Figure 3.20 shows that there is a clear relationship between grinding efficiency and pressure for each nozzle geometry, while Figure 3.21 suggests that there is a single relationship between grinding efficiency and equivalent velocity for all the Laval type nozzles with the same throat diameter.

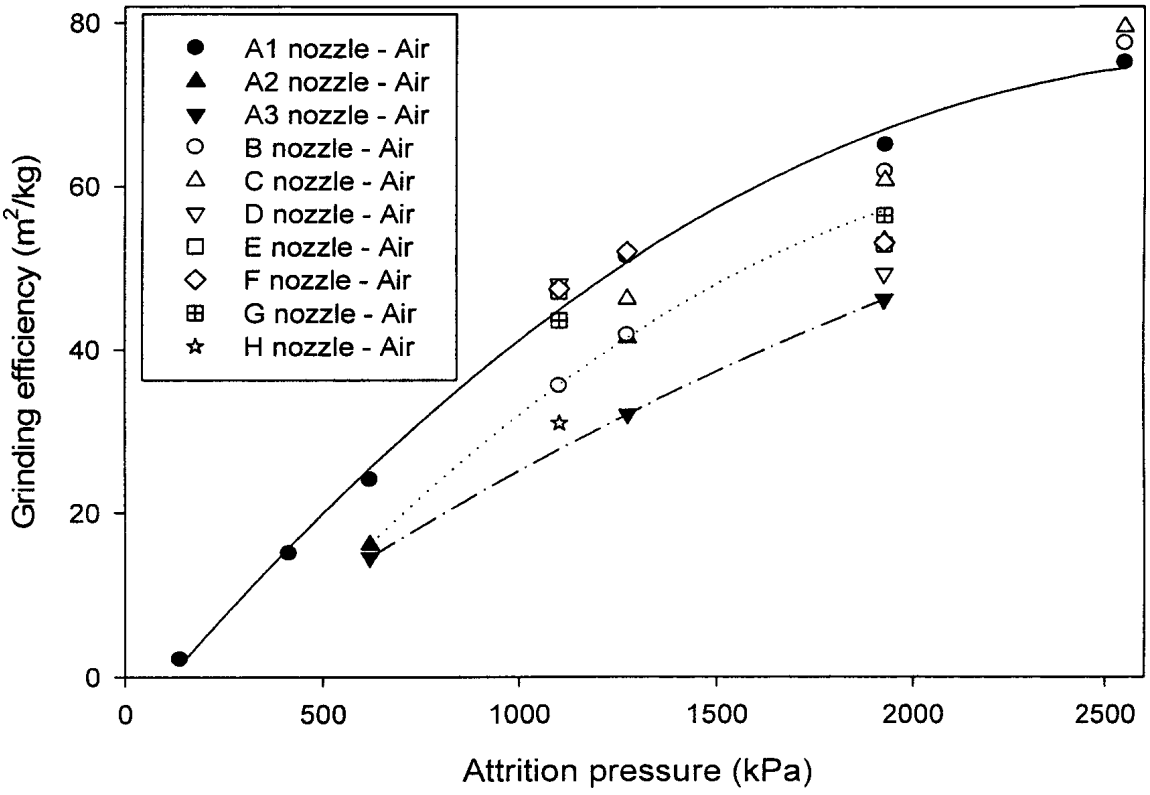

Figure 3.20: Grinding efficiency versus attrition pressure when using air for attrition.

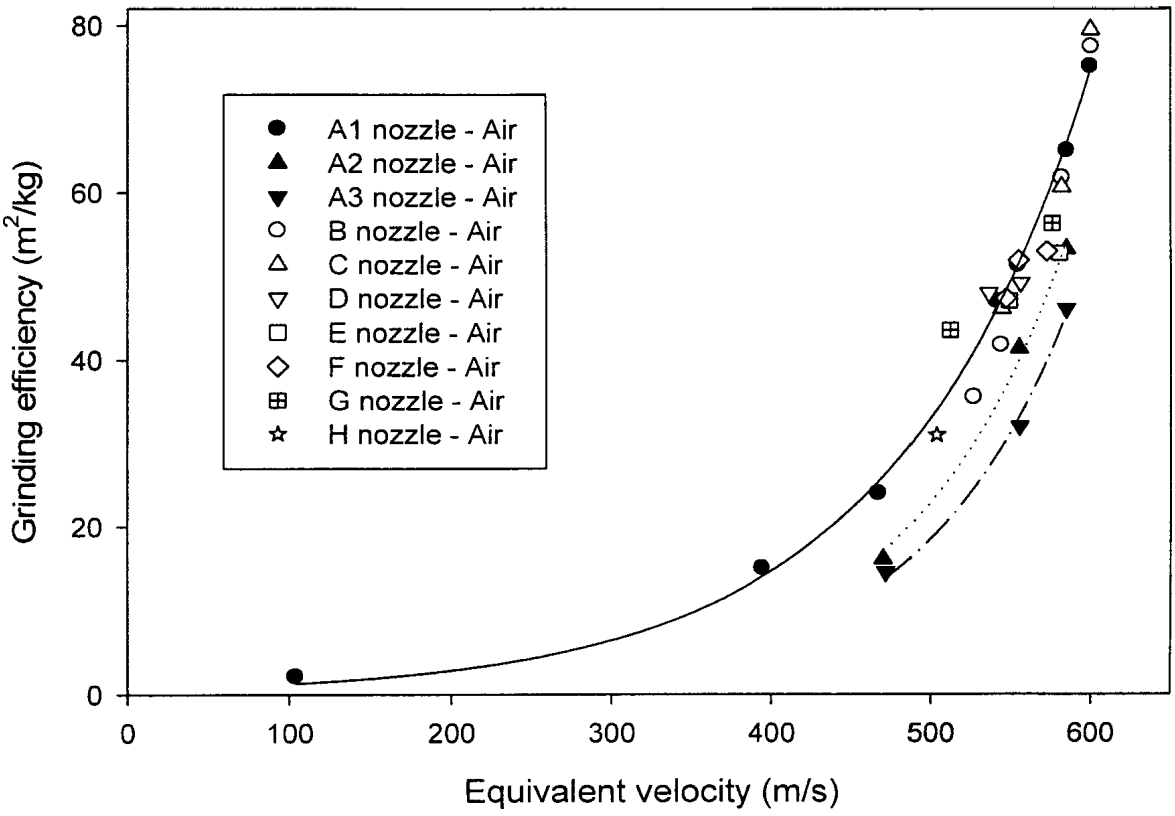

Figure 3.21: Grinding efficiency versus equivalent velocity for all the nozzles using air for attrition.

Results presented in Figure 3.22 indicate that when considering thrust most data points fit on a single curve, except for some points for which a possible explanation is provided later. The relationship between grinding efficiency and thrust is related to the study (Midoux et al., 1999) reviewed in the section on the modeling of Laval nozzles, where the grinding pressure is directly correlated to kinetic energy of the gas and to the energy transmitted to particles for grinding. The main difference is that in that study (Midoux et al., 1999), there were no supersonic velocities since an abrupt nozzle without the divergent section was used; therefore, it is assumed that the sonic velocity U_s corresponds to a Mach number equal to 1. It was also mentioned in the section on the modeling of Laval nozzles that an increase in momentum gives an increase in grinding efficiency (McMillan et al., 2007), and this concept is also similar to the thrust concept

with the difference that the thrust takes into account the effect of the background pressure, and nozzle exit pressure, as well as the nozzle exit area.

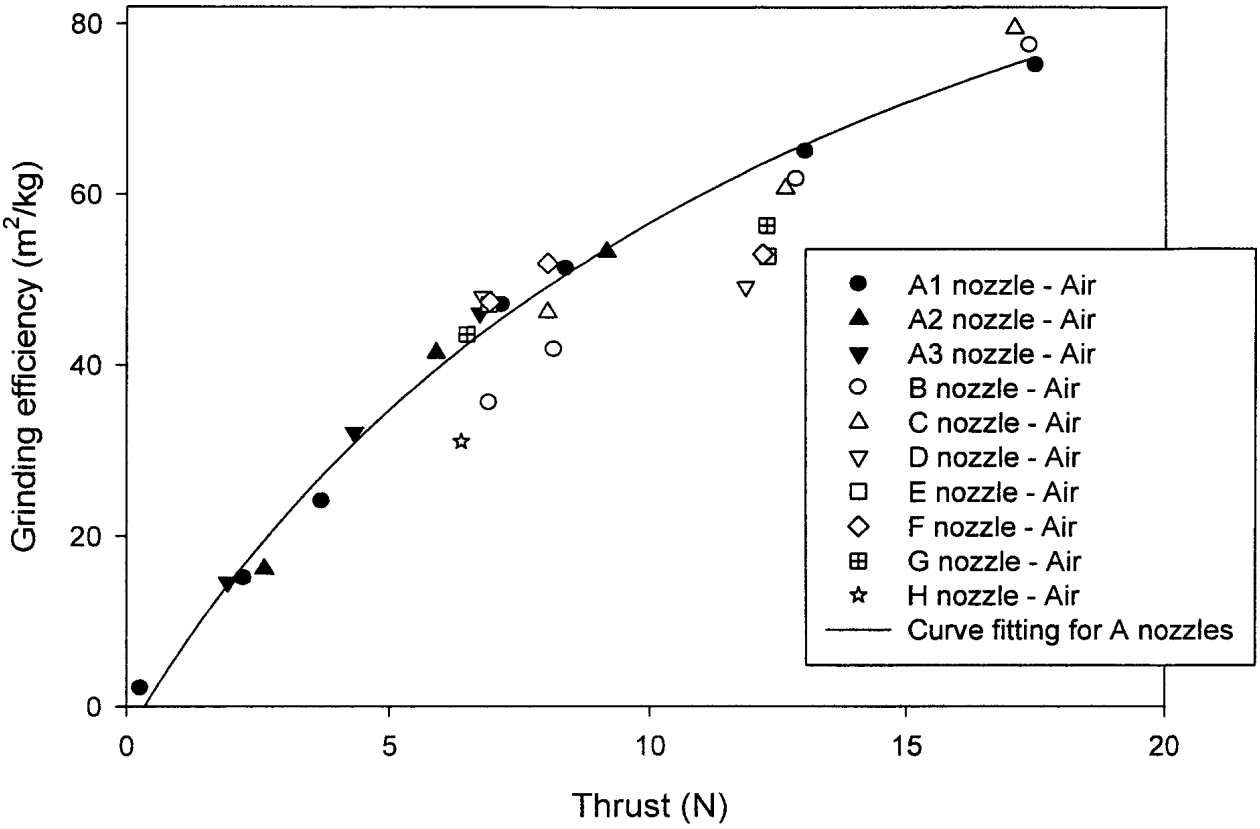

Figure 3.22: Grinding efficiency versus thrust with air as attriting gas.

Figures 3.23 to 3.25 show the effect of different attrition gases for the A nozzle geometry (A1, A2, and A3 nozzles). The main conclusion from these three figures is that grinding efficiency results with different attrition gases fit on different curves for attrition pressure, equivalent velocity and thrust even for the same nozzle type. A new relationship must, therefore, be developed to properly account for the effect of gas properties.

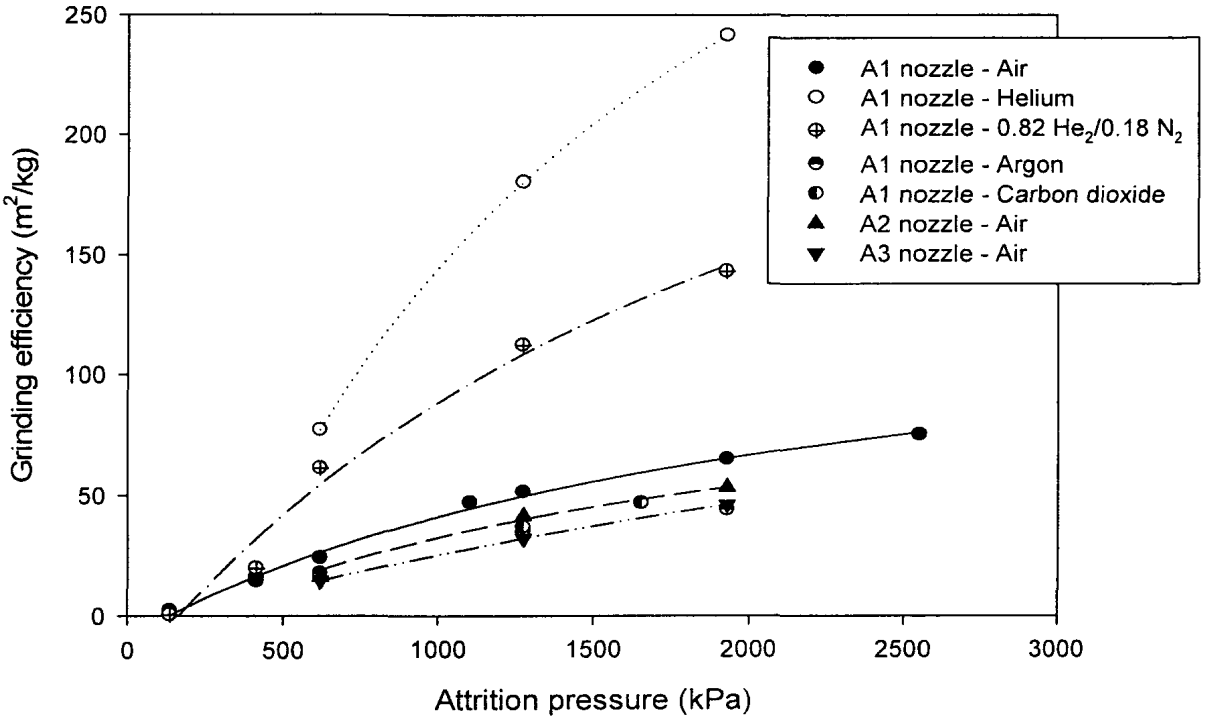

Figure 3.23: Grinding efficiency versus pressure for the A nozzles and all the attrition gases.

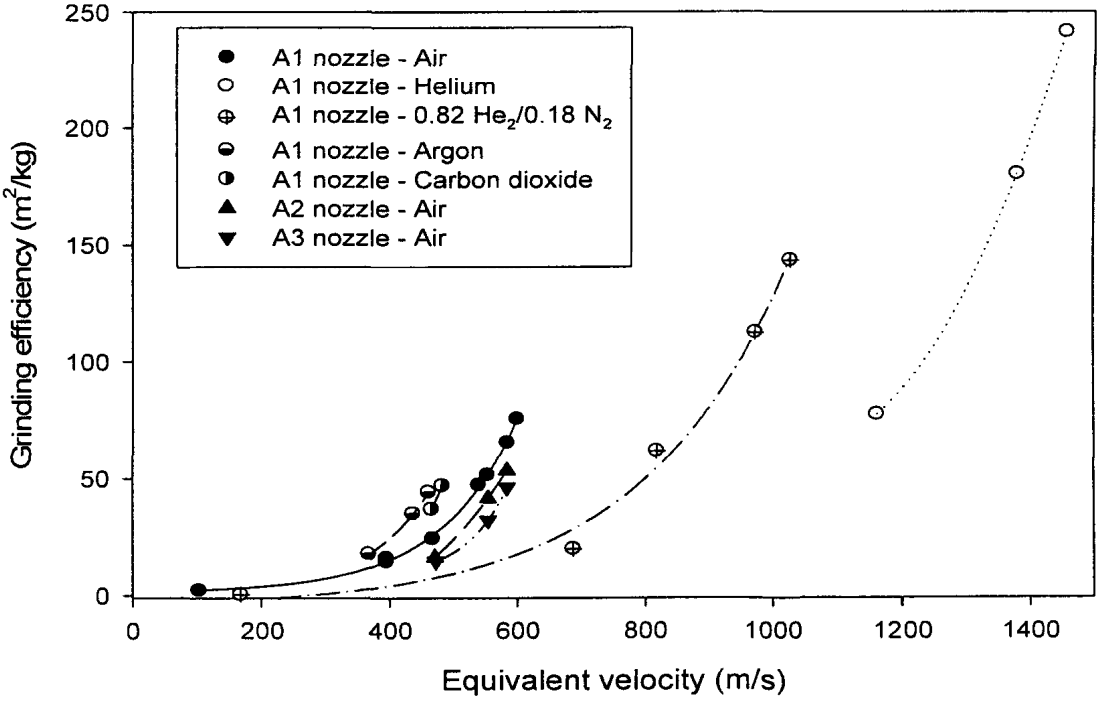

Figure 3.24: Grinding efficiency versus equivalent velocity for A nozzles and all the gases.

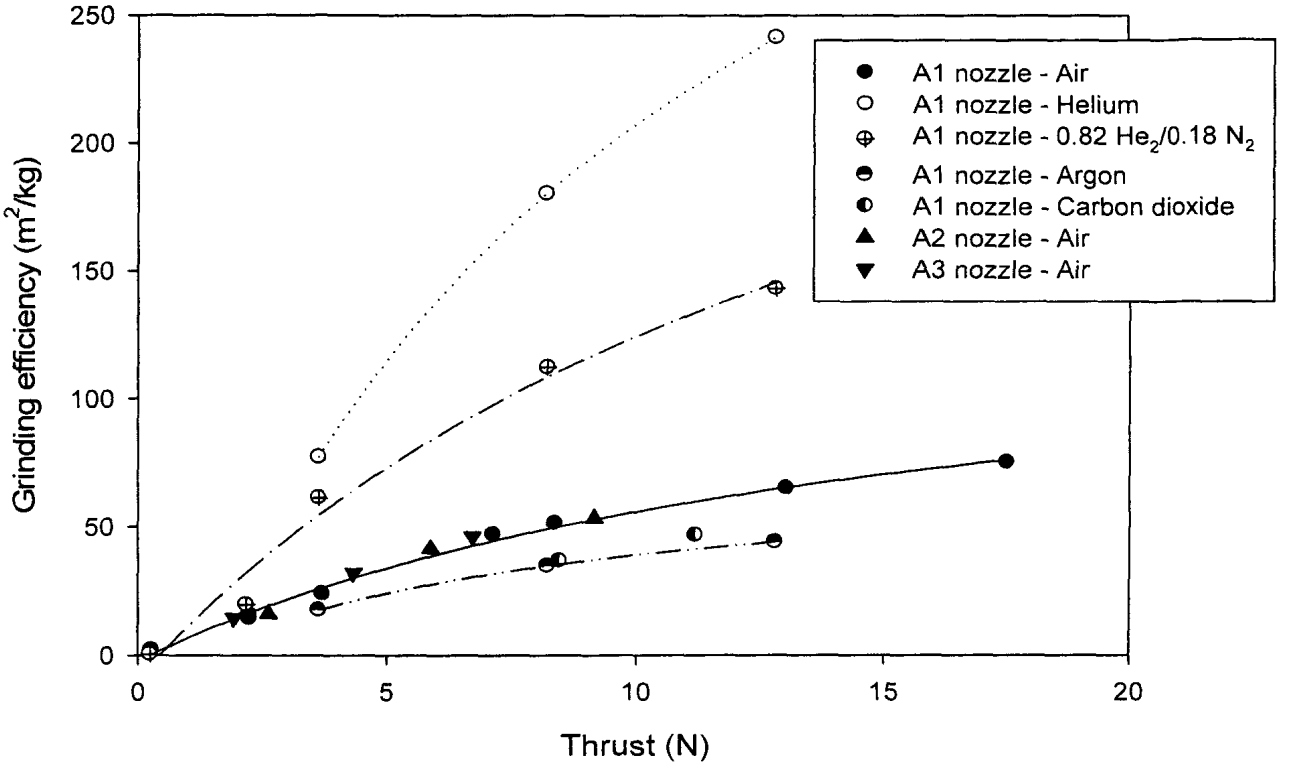

Figure 3.25: Grinding efficiency versus thrust for the A nozzles and the different gases used during experimentation.

Figures 3.26 and 3.27 used all the attrition runs performed in this work, and show the relationship between grinding efficiency and equivalent velocity, and grinding efficiency and thrust, respectively. They confirm the strong effect of gas properties on grinding efficiency that cannot be accounted for by the equivalent velocity or the thrust.

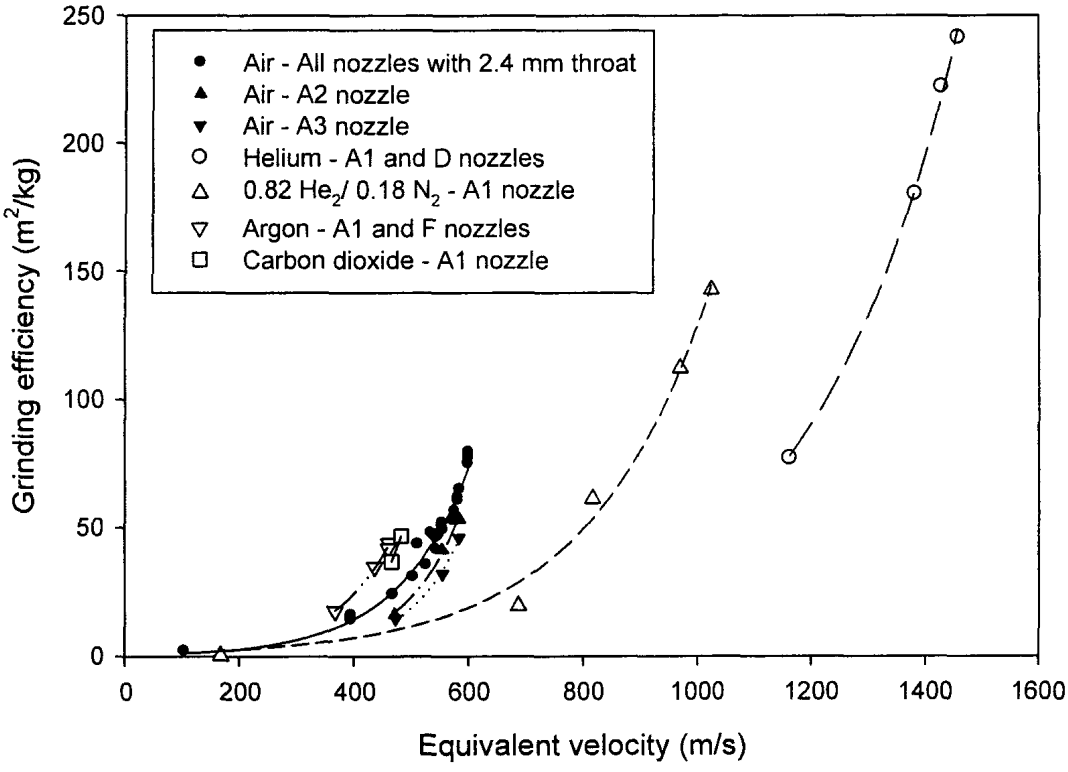

Figure 3.26: Relationship between equivalent velocity and grinding efficiency for all attrition runs.

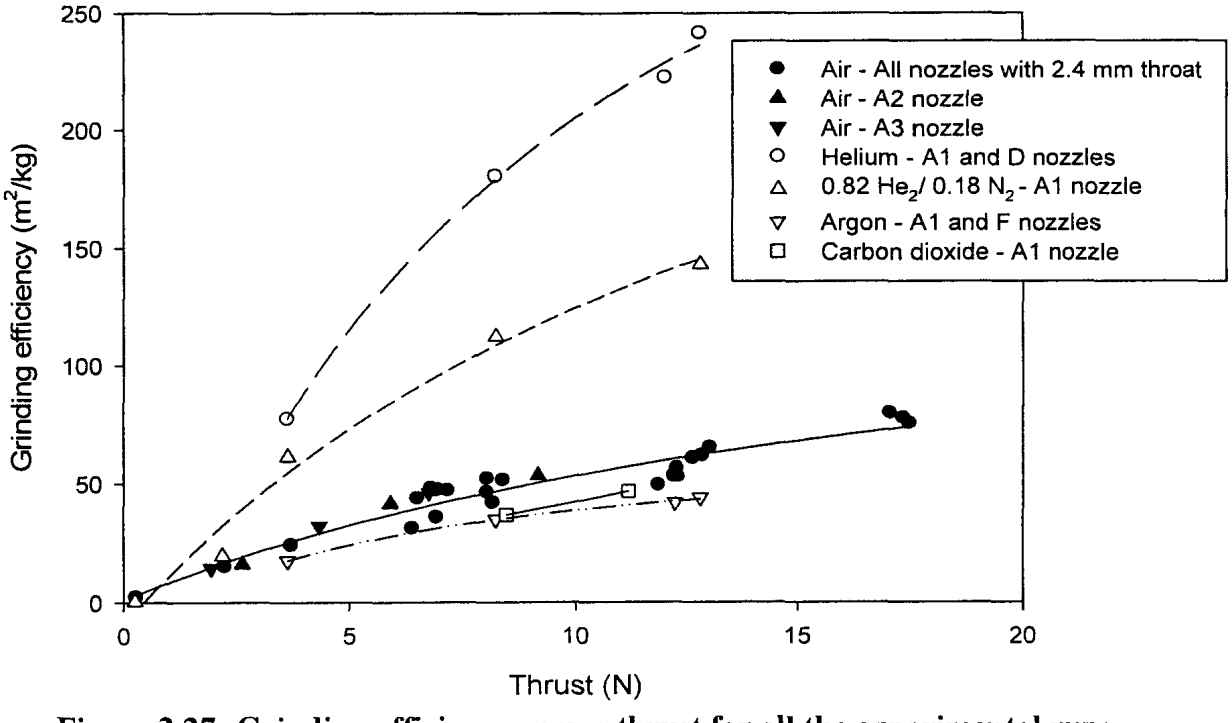

Figure 3.27: Grinding efficiency versus thrust for all the experimental runs.

As with Figure 3.25, Figure 3.27 shows that there are different fitting curves for different attrition gases, and data for air runs are represented by a single curve even for nozzles with different throat diameters, as was also shown by Figure 3.22. In order to extend this relationship to other gases, a correction factor is proposed to account for the impact of gas properties:

$$\left(\frac{U_{eq.gas}}{U_{eq.air}}\right)^{0.61}\left(\frac{\rho_{gas}}{\rho_{air}}\right) \tag{3.18}$$

Figure 3.28 shows that multiplying the measured grinding efficiency by this correction factor provides an excellent general relationship between the corrected grinding efficiency and thrust for all the A nozzle experiments.

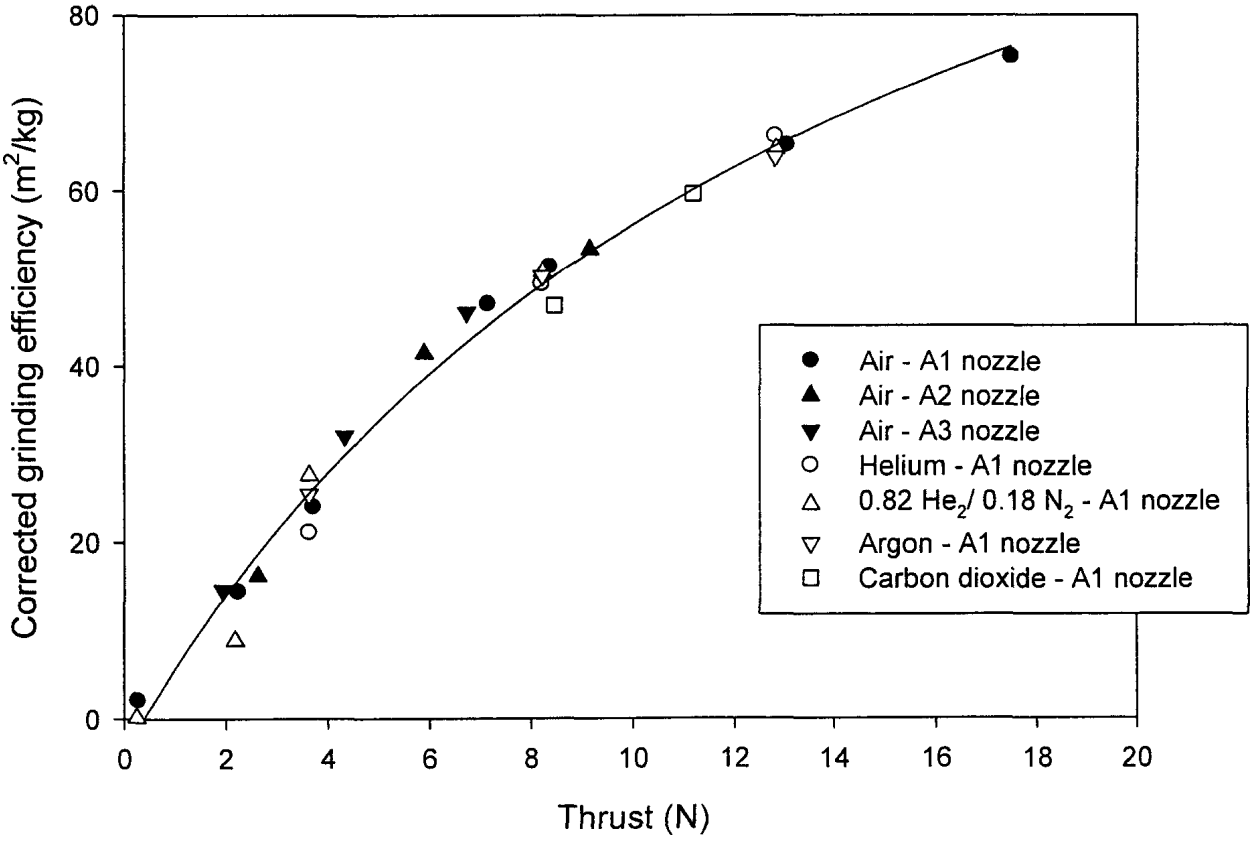

Figure 3.28: Corrected grinding efficiency versus thrust for all the gases and the A nozzles.

The following correlation is proposed for the grinding efficiency:

$$\eta_{pred.} = \frac{(-3.849 + 9.842 * F)}{(1 + 0.069 * F)} \Bigg/ \left(\frac{U_{eq.gas}}{U_{eq.air}}\right)^{0.61} \left(\frac{\rho_{gas}}{\rho_{air}}\right) \tag{3.19}$$

where F is the thrust in Newtons.

Figures 3.29 and 3.30 illustrate the comparison between predicted and experimental grinding efficiencies. Figure 3.29 shows all data points, and Figure 3.30 shows the data over the 0 to 100 m^2/kg range to clearly identify the nozzles for which the experimental efficiencies were significantly lower than the predicted efficiencies.

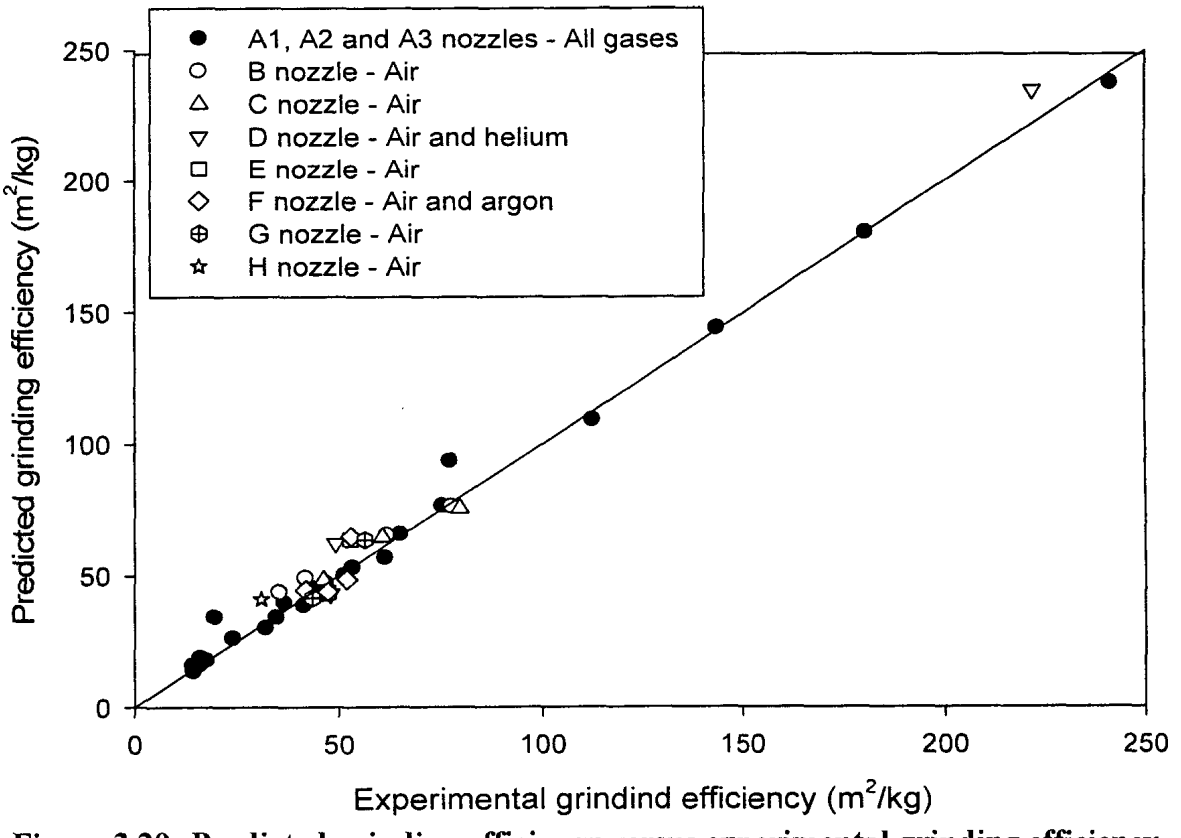

Figure 3.29: Predicted grinding efficiency versus experimental grinding efficiency.

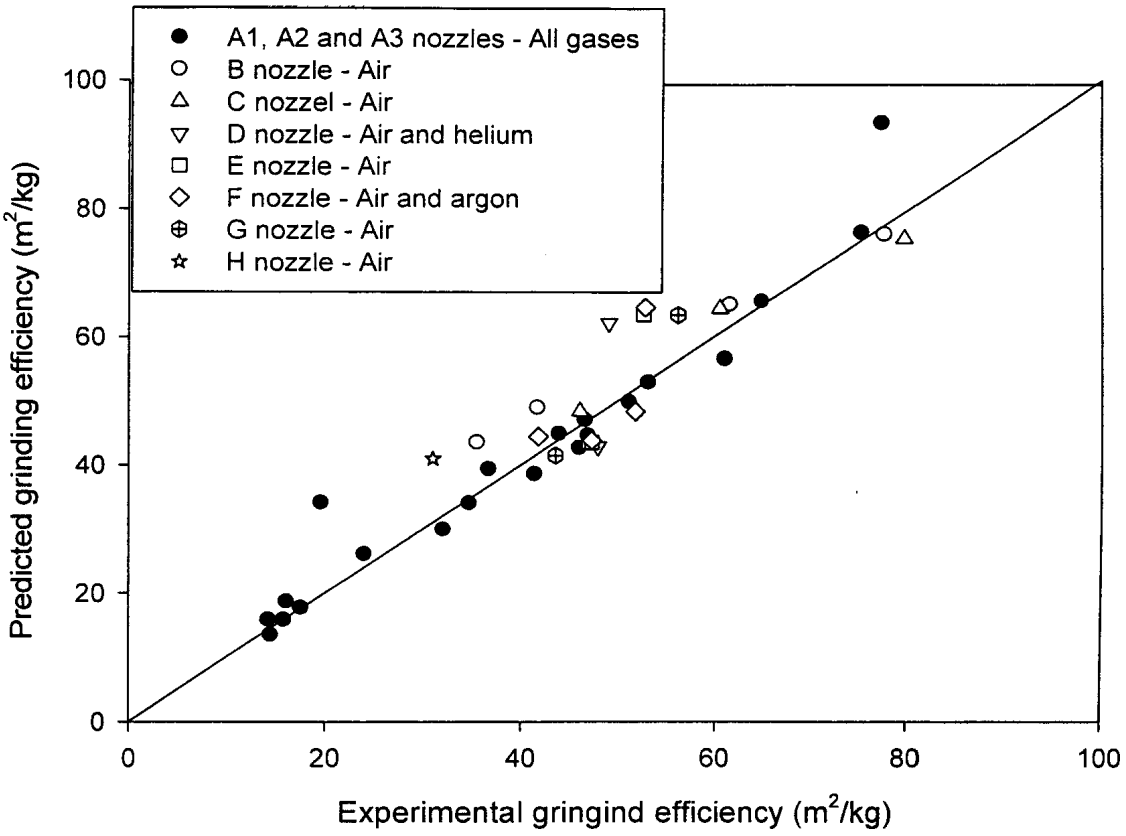

Figure 3.30: Predicted grinding efficiency versus experimental grinding for a smaller data range.

Nozzles that fail to achieve the efficiency predicted by Equation (3.19) correspond to conditions with the highest or lowest difference between exit pressure and background pressure, thus making the nozzles underexpanded or overexpanded, respectively. For these nozzles, the term $(p_e - p_o)A_e$ in Equation 3.8, is either positive or negative. In the case of a negative value, it seems obvious that this will have a detrimental effect on the calculated thrust and, therefore, on the resulting grinding efficiency. However, a positive value might be expected to increase the thrust and, therefore, to also increase the grinding efficiency: this does not happen, as shown in Figure 3.31. In this Figure, it is clear that both high and low values of $(p_e - p_o)A_e$ negatively affect the grinding efficiency. The points on the left represent the overexpanded nozzles and the points on the right are for underexpanded nozzles. Figure 3.31 reveals that there are experimental conditions tested where the grinding efficiency is greatly affected, and that even the A1 nozzle may give undesirable results if the

difference between the exit pressure and the background pressure makes the nozzle overexpanded. Although it is highly probable that the waves and shocks formed in the open air, for an underexpended or overexpanded nozzle, do not behave the same way when the nozzle is inside a fluidized bed, they still negatively affect the grinding efficiency.

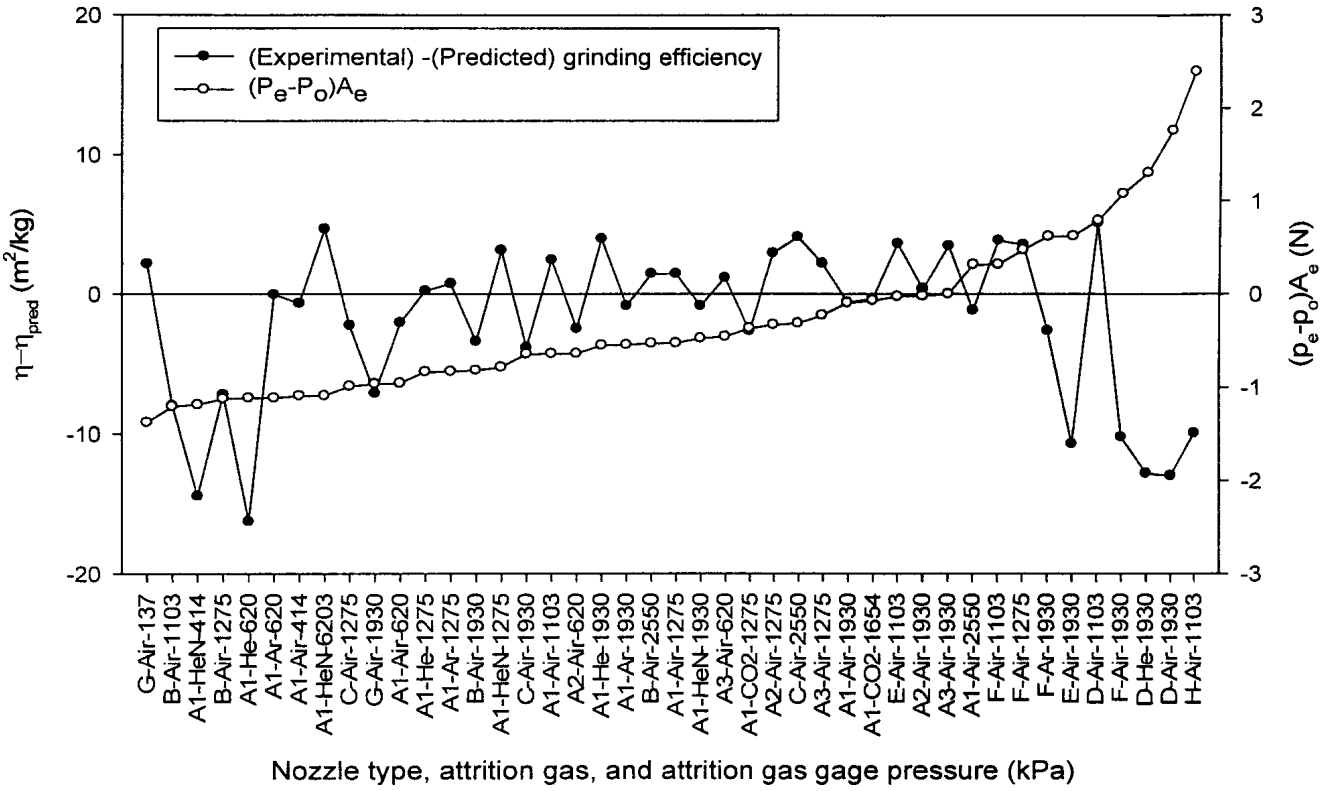

Figure 3.31: Experimental minus predicted grinding efficiency when looking at the grade of underexpansion and overexpansion in the sonic nozzles.

The A nozzles have a geometry that make them work well over a wide range of pressures. At low attrition pressures (414 – 620 kPa), these nozzles are not better than most of the other nozzles, but perform better at pressures of 1000 – 1500 kPa. Nozzles B and C seem equal or better than the A1 nozzle for pressures around 2500 kPa.

One limitation of the experiments described in this work is that the backpressure was always kept constant and it was not possible to change it due to equipment

limitations. If that pressure could be set equal to the nozzle exit pressure for the nozzles that were highly underexpanded or overexpanded, it would be possible to confirm the effect of backpressure on the grinding efficiency.

3.5 Conclusions

Grinding experiments were conducted in a gas-solid fluidized bed using 11 sonic nozzles with different geometries, and 5 attrition gases, at attrition pressures between 138 and 2550 kPa. Fluidization velocity, mass of bed solids, and the size distribution of the initial silica sand particles were kept constant for all the experiments.

A new approach analyzes the grinding efficiency by using the theoretical equations for a compressible gas, assuming isentropic and one-dimensional flow. The grinding efficiency is related to the thrust generated by the sonic nozzles, with an empirical correction for gases other than air, since gases with lower molecular weights produce higher nozzle exit and equivalent velocities, which enhances grinding.

Highly underexpanded or overexpanded nozzles produce poor grinding efficiency results, and optimal results correspond to operating conditions when the nozzle exit pressure is equal to the background pressure.

3.6 Nomenclature

A_e Area at the nozzle exit (m^2)

A_{th} Area at the nozzle throat (m^2)

D_e Diameter at the nozzle exit (m)

$\dot{E}_k$ Kinetic energy of grinding gas (W)

d_{gd} Gas distributor orifice diameter (m)

D_{th} Diameter at the nozzle throat (m)

f Friction coefficient (-)

F Thrust (N)

K Attrition constant (s^2/m^2)

$\dot{m}$ Mass flow rate of gas (kg/s)

M_e Mach number at nozzle exit (-)

M_{th} Mach number at nozzle throat (-)

p_e Gas pressure at the nozzle exit (kPa)

p_t Total pressure (kPa)

p_{th} Gas pressure at the nozzle throat (kPa)

p_o Background pressure (kPa)

R Gas constant (Nm/moles/K)

$R_{a,j}$ Jet attrition jet (kg/s)

T_e Gas temperature at the nozzle exit (K)

T_t Total temperature (K)

T_{th} Gas temperature at the nozzle throat(K)

U_{gd} Gas velocity at gas distributor (m/s)

U_s Sonic velocity (m/s)

U_e Gas velocity at the nozzle exit (m/s)

U_{eq} Equivalent velocity (m/s)

U_{th} Gas velocity at the nozzle throat (m/s)

Greek letters

α Half angle of the sonic nozzle (degrees)

γ Specific heat ratio of the gas (-)

ρ_e Gas density at the nozzle exit

ρ_{gd} Gas density at gas distributor (kg/m^3)

ρ_{th} Gas density at the nozzle throat (kg/m^3)

λ Correction factor for axial momentum loss (-)

η Grinding efficiency (m^2/kg)

3.7 References

Abdulhadi, "Dynamics of Compressible Air Flow with Friction in a Variable-Area Duct", *Wärme – und Stoffübertragung*, **22** 169-172 (1988).

Arastoopour, M., and Chen, C., "Attrition of Char Agglomerates", *Powder Technol.*, **3** 99-106 (1983).

Benz, M., Herold, H., and Ulfik, B., "Performance of a Fluidized Bed Jet Mill as a Function of Operating Parameters", *Int. J. Miner. Process.*, **44 – 45** 507-519 (1996).

Chapman, C. J., *High Speed Flow*, Cambridge texts in applied mathematics, 1st edn. 127-131 (2000).

Forsythe, W. L., and Hertwig, W. R., "Attrition Characteristics of Fluid Cracking Catalyst", *Ind. Eng. Chem.*, **41** 1200-1206 (1949).

Ghadiri, M., Cleaver, J. A. S., Tuponogov, V. G., and Werther, J., "Attrition of FCC Powder in the Jetting Region of a Fluidized Bed", *Powder Technol.*, **80** 175-178 (1994).

John, J. E., and Keith, T. G., *Gas Dynamics*, Pearson Prentice Hall, 3rd edn., 68-102 and 283-331 (2006).

Lin, L., Sears, J. T., and Wen, C. Y., "Elutriation and Attrition of Char from a Large Fluidized Bed", *Powder Technol.*, **27** 105-115 (1980).

McMillan, J., Briens, C., Berruti, F., and Chan, E., "High Velocity Attrition Nozzles in Fluidized Beds", *Powder Technol.*, **175** 133-141 (2007).

Mebtoul, M., Large, J. F., and Guigon, P., "High Velocity Impact of Particles on a Target – an Experimental Study", *Int. J. Miner. Process.*, **44 – 45** 77-91 (1996).

Midoux, N., Hosek, P., Pailleres, L., and Authelin, J. R., "Micronization of Pharmaceuticals Substances in a Spiral Jet Mill", *Powder Technol.*, **104** 113-120 (1999).

Palaniandy, S., Azizli, K. A. M., Hussin, H., and Hashim, S. F. S., "Effect of Operational Parameters on the Breakage Mechanism of Silica in a Jet Mill", *Miner. Eng.*, **21** 380-388 (2008).

Patel, K., Nienow, A.W., and Milne, I. P., "Attrition of Urea in a Gas-Fluidised Bed", *Powder Technol.*, **47** 257-261 (1986).

Perry, R. H., Green, D. W., and Maloney, J. O., *Perry's Chemical Engineers' Handbook*, McGraw-Hill, 7th edn., 6-25 – 6-26 (1997).

Shamlou, P. A., Liu, Z., and Yates, J. G., "Hydrodynamic Influences on Particle Breakage in Fluidized Beds", *Chem. Eng. Sci.*, **45** 809-817 (1990).

Stein, M., Seville, J. P. K., and Parker D. J., "Attrition of Porous Particles in a Fluidized Bed", *Powder Technol.*, **100** 242-250 (1998).

Sutton, G. P., and Biblarz, O., *Rocket Propulsion Elements*, John Wiley & Sons, Inc, 7th edn., 32, and 77-82 (2001).

Werther, J., and Xi, W., "Jet Attrition of Catalyst Particles in Gas Fluidized Beds", *Powder Technol.*, **76** 39-46 (1993).

CHAPTER 4

Effect of Thrust on Supersonic Gas Jet Penetration in Gas-Solid Fluidized Beds

4.1 Introduction

Gas-solid fluidized beds are used in the petrochemical, chemical, food and pharmaceutical industries, and it is important to understand the interaction between gas jets and the fluidized bed for design purposes. Vertical jet penetration from gas distributors has been widely studied (Merry, 1975; Yang and Keairns, 1979; Luo et al., 1999; Hong et al., 2003), and some studies have also investigated horizontal subsonic gas jets (Zenz, 1968; Merry, 1971; Yates et al., 1988; Benjelloun et al., 1995; Hong, 1997). Dawe et al. (2008) developed a correlation to predict gas jet penetration for supersonic nozzles, and Ariyapadi et. al (2004) proposed a model to predict the jet penetration of sonic horizontal gas-liquid jets using the Benjelloun et al. (1995) correlation. They mentioned that momentum in a free jet is conserved, and the jet penetration can be related to some degree to the energy dissipation. That model is based on the momentum flux of two-phase sprays. Ariyapadi et al. (2003) also correlated gas jet penetration with momentum.

Jet penetration depends on variables such as fluidizing gas and solids densities, particle diameter, bed height, fluidization velocity, void fraction, velocity of the injected gas, and injection nozzle diameter (Li et al., 2008; Merry, 1971; Hong et al., 1997). Li et al. (2007) and Vaccaro (1997) mentioned that the expansion angle is another important factor to be considered when describing jet behavior, as this may affect the prediction of gas and particle entrainment in the jet. An increase in gas and solids entrainment into the jet reduces jet penetration (Dawe et al., 2008; Ariyapadi et al., 2003) because energy dissipation occurs faster. It is generally accepted that jet penetration increases with both increasing nozzle diameter and velocity of the injected gas. On the other hand, increasing the fluidization velocity reduces the jet penetration (Ariyapadi et al., 2003; Chyang et al., 1997).

Some correlations for horizontal subsonic jet penetration are shown in Table 4.1.

Table 4.1: Some correlations to calculate jet penetration of horizontal subsonic gas jets.

Correlation's reference	Equation
Zenz (1968)	$0.044\frac{L_{jet}}{D_e}+1.48=0.5\log_{10}\left(0.67\rho_e U_e^{\,2}\right)$
Merry (1971)	$\frac{L_{jet}}{d_e}+4.5=5.25\left[\frac{\rho_e U_e^{\,2}}{(1-\varepsilon)\rho_p g d_p}\right]^{0.4}\left(\frac{\rho_o}{\rho_p}\right)^{0.2}\left(\frac{d_p}{D_e}\right)^{0.2}$
Yates et al. (1998)	$\frac{L_{jet}}{D_e}=2.8\left[\frac{\rho_e U_e^{\,2}}{(\rho_p-\rho_e)gD_e}\right]^{0.4}$
Benjelloun et al. (1995)	$\frac{L_{jet}}{D_e}=5.52\left[\frac{\rho_e U_e^{\,2}}{(\rho_p-\rho_e)gD_e}\right]^{0.27}$
Hong et al. (1997)	$\frac{L_{jet}}{D_e}+3.8=1.89\,X\,10^{6}\left[\frac{\rho_e u_e^{\,2}}{(1-\varepsilon)\rho_p g d_p}\right]^{0.327}\left(\frac{\rho_o}{\rho_p}\right)^{1.974}\left(\frac{d_p}{D_e}\right)^{-0.040}$

In this work, the effect of thrust on the gas jet penetration has been investigated. The thrust concept is taken from the aeronautics field where it is typically defined as the force produced by a rocket propulsion system acting upon a vehicle (Sutton and Biblarz, 2001). Therefore, thrust can be interpreted as the reaction force created by the ejection at high velocity of gas from a supersonic nozzle.

Figure 4.1 shows a convergent-divergent nozzle and its key properties at the nozzle's throat and exit. The thrust of the supersonic jet is calculated assuming isentropic flow of a perfect gas, neglecting friction and heat transfer and attributing the variations in gas properties only as a result of the variations in cross sectional area. One-dimensional, steady flow is also assumed, and for gas flows, changes in potential and gravitational forces are neglected (John and Keith, 2006).

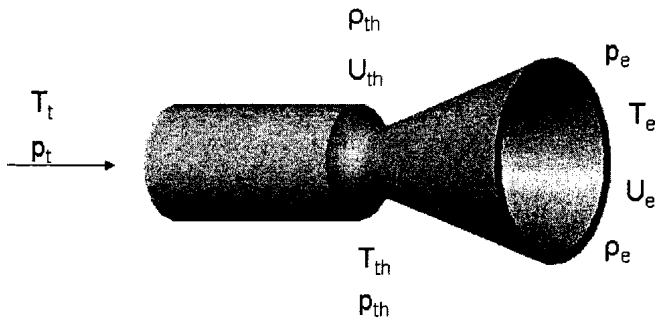

Figure 4.1: Convergent-divergent (C-D) nozzle showing different gas properties at the exit and at the throat.

Thrust is calculated with the conditions at the tip of the nozzle:

$$F = \dot{m}U_e + (p_e - p_o)A_e \tag{4.1}$$

The mass flow rate is given by:

$$\dot{m} = A_{th} p_t \sqrt{\frac{\gamma}{T_t R}\left(\frac{\gamma+1}{2}\right)^{\frac{\gamma+1}{2(1-\gamma)}}} \tag{4.2}$$

The exit Mach number (M_e) can be obtained from:

$$\frac{A_e}{A_{th}} = \frac{1}{M_e}\left[\left(\frac{\gamma+1}{2}\right)\left(1+\frac{\gamma-1}{2}M_e^2\right)\right]^{\frac{\gamma+1}{2(\gamma-1)}} \tag{4.3}$$

The exit pressure can be obtained from:

$$\frac{p_e}{p_t} = \left(1 + \frac{\gamma - 1}{2} M_e^2\right)^{\frac{\gamma}{1-\gamma}} \tag{4.4}$$

The exit temperature is derived from:

$$\frac{T_e}{T_t} = \left(1 + \frac{\gamma - 1}{2} M_e^2\right)^{-1} \tag{4.5}$$

Finally, the exit velocity can be obtained from:

$$U_e = M_e \sqrt{\gamma R T_e} \tag{4.6}$$

Conditions at the nozzle throat are obtained by taking the Mach number as 1.

The variations of pressure, temperature, density, and Mach number with respect to change in cross-sectional area through a convergent-divergent nozzle are shown in Figure 4.2, and it is seen that pressure decreases faster than temperature and density. Figure 4.3 shows the different flow conditions through a convergent-divergent nozzle and outside the nozzle. Different kinds of flows can be observed, depending on the total pressure of the gas (p_t) and the background pressure (p_o).

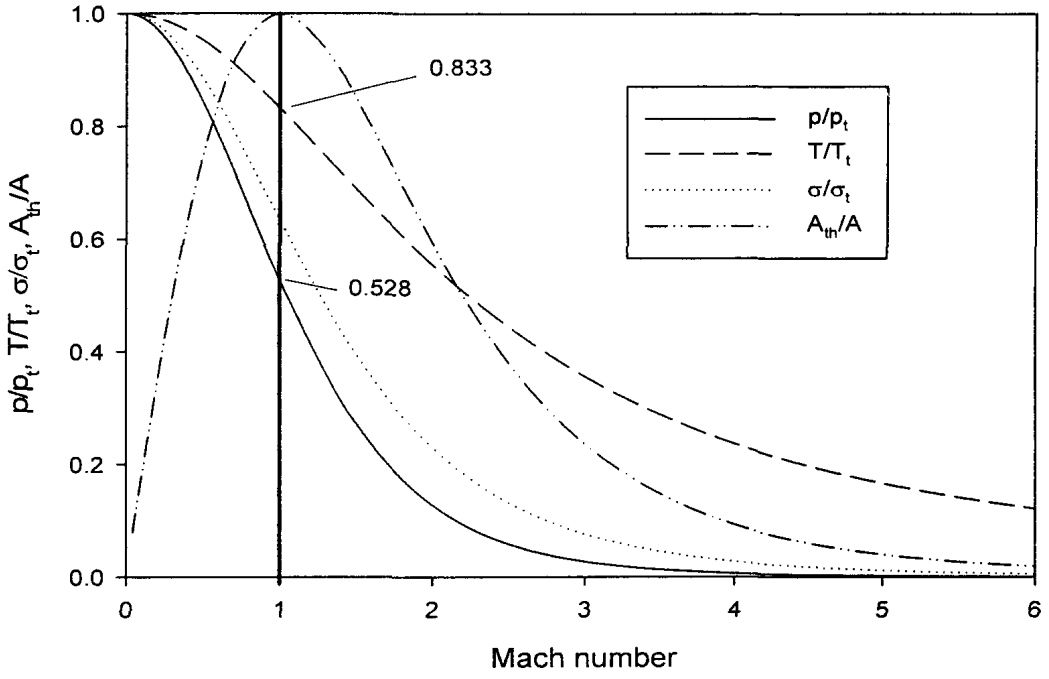

Figure 4.2: Variation of pressure, temperature, density, and Mach number with area change through a convergent-divergent nozzle.

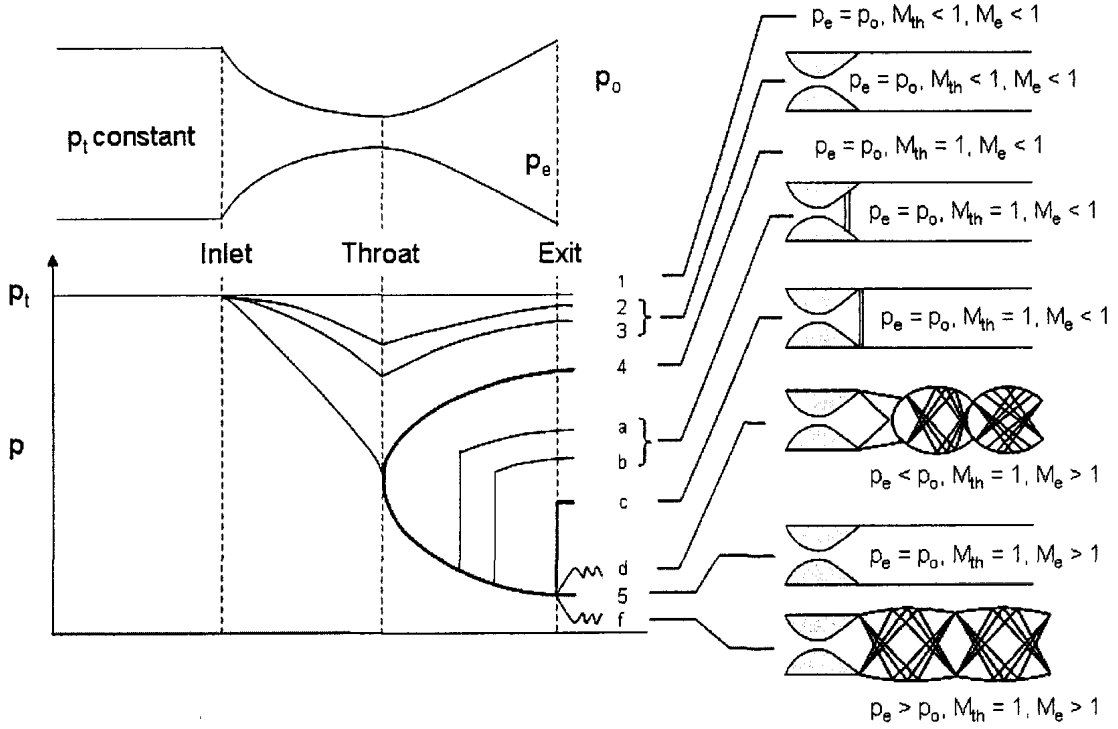

Figure 4.3: Pressure distribution in a convergent–divergent nozzle (Adapted from John and Keith, 2006).

Curves 1 to 4 in Figure 4.3 represent subsonic flow through the nozzle. In condition 4, the nozzle is choked at the throat, but the background pressure is not low enough to achieve supersonic flow in the divergent section. Flows *a* to *c* are supersonic after the nozzle's throat, however a normal shock, represented by the vertical lines, is formed and after this shock the nozzle flow becomes subsonic. In condition 5, the nozzle exit pressure is equal to the background pressure and this is considered the ideal condition for the supersonic flow. Curves *d* and *f* represent conditions where either the pressure at the exit of the nozzle is lower or higher than the background pressure, and shock and waves will appear outside the nozzle. Condition *d* refers to an overexpanded nozzle and condition *f* represents an underexpanded nozzle.

It is important to note that for all backpressures below curve *c*, the flow downstream of the exit plane adjusts to the backpressure outside the nozzle, and the flow inside the nozzle remains unchanged. Figure 4.4 shows how the nozzle exit pressure and the backpressure are related in a convergent–divergent nozzle (John and Keith, 2006).

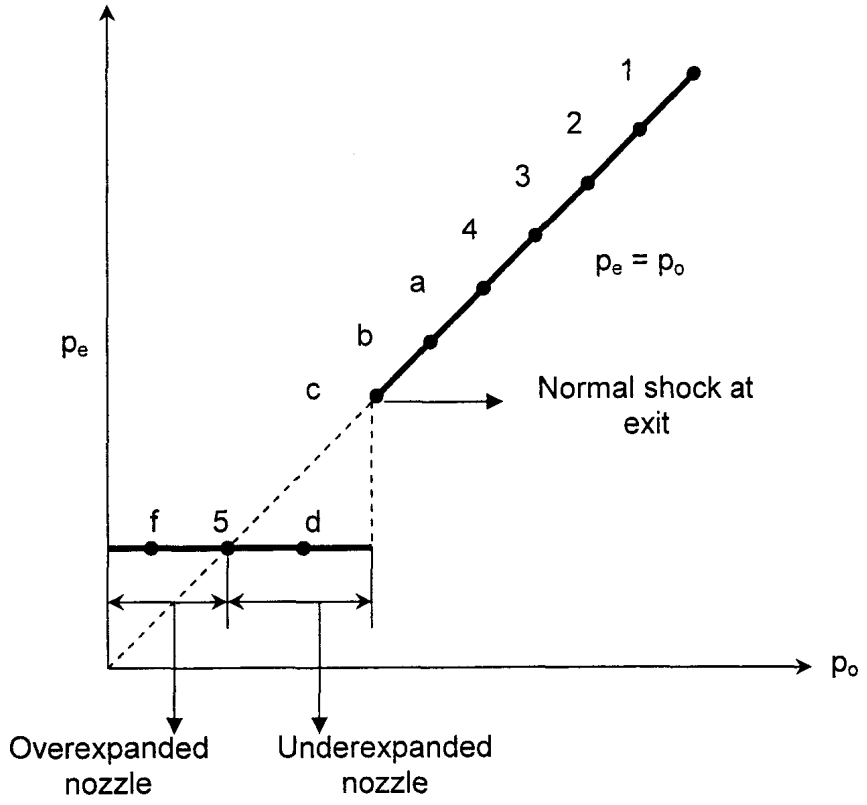

Figure 4.4: Exit pressure versus backpressure for a convergent-divergent (CD) nozzle (Adapted from John and Keith, 2006).

To maximize thrust from a convergent-divergent nozzle, there are some constraints in its design, especially relative to the divergent section. The divergent angle of this section should not be excessively large in order to avoid shocks and axial momentum losses. On the contrary, if the divergence angle is too small, an excessive boundary layer will occur (Perry et al., 1997). The axial momentum loss for a conical divergent section can be calculated with a theoretical correction factor λ, defined as the ratio between the momentum of the gases in a nozzle with a finite nozzle angle, and the momentum of an ideal nozzle with all the gases flowing in an axial direction (Sutton and Biblarz, 2001):

$$\lambda = \frac{1}{2}(1 + \cos\alpha) \tag{4.7}$$

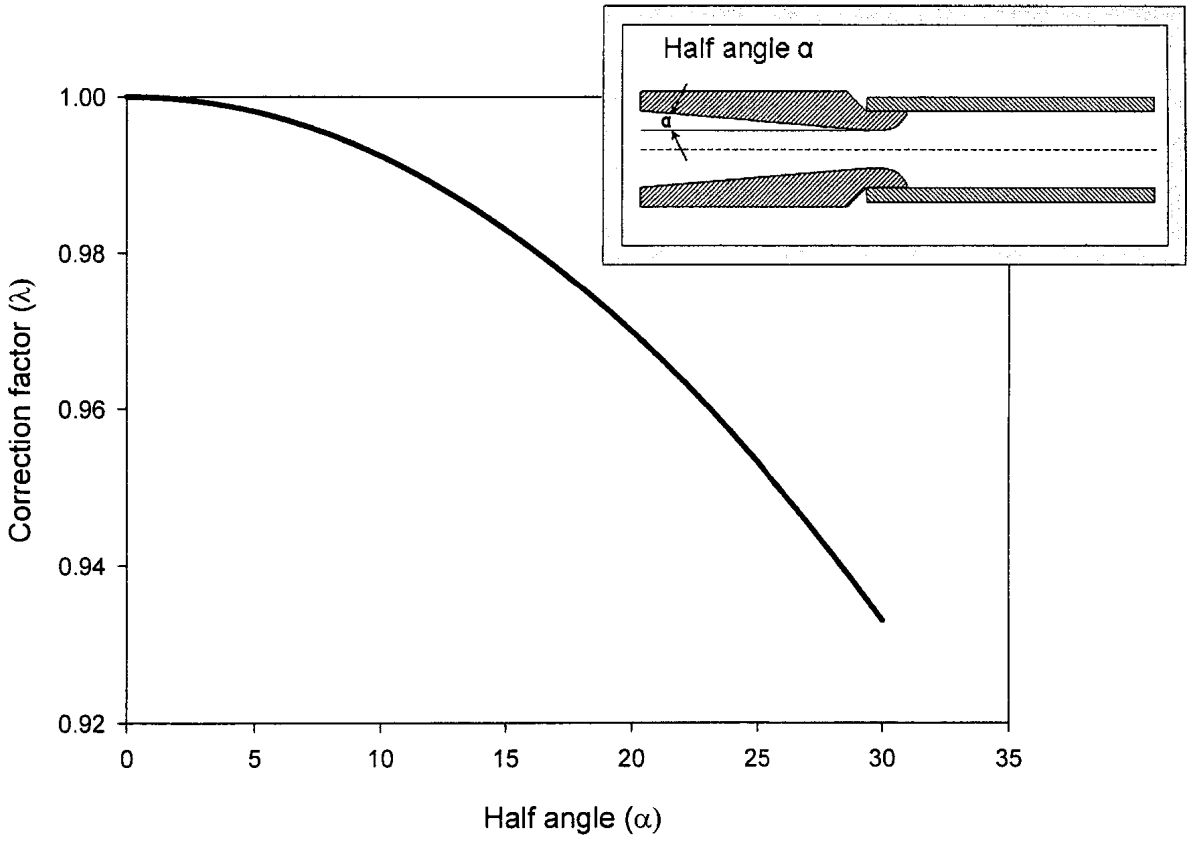

Figure 4.5: Nozzle angle correction factor for conical nozzles.

It is seen in Figure 4.5 that, for half angles more than 5°, the axial momentum loss increases drastically.

The friction effects in a convergent-divergent nozzle can be estimated using the equations given by Abdulhadi (1998):

Mach number:

$$\gamma M^2 \frac{f}{2D} = \frac{2dD}{Ddx} + \frac{2(1-M^2)}{M[2+(\gamma-1)M^2]} \frac{dM}{dx} \tag{4.8}$$

Temperature:

$$\frac{1}{T}\frac{dT}{dx} = \frac{2(\gamma-1)M^2}{(1-M^2)D}\frac{dD}{dx} + \frac{\gamma(\gamma-1)M^4 f}{2(1-.M^2)D} \tag{4.9}$$

Pressure:

$$\frac{1}{P}\frac{dp}{dx} = \frac{2\gamma M^2}{(1-M^2)D}\frac{dD}{dx} + \frac{\gamma M^2(1+(\gamma-1)M^2)f}{2(1-.M^2)D} \tag{4.10}$$

The previous equations can be applied to any nozzle shape, as long as there is an equation to represent that shape. When combining divergence and friction losses for the case of a conical divergent section, it is found that the optimum half angle is between 3° and 7.5° approximately, and all the nozzles used in this study are within this range. This optimum half angle range was obtained from the ratio of the thrust generated by the A1 nozzle when injecting air at 25 °C and a total pressure of 2170 kPa (300 psig), considering divergence and friction losses, and the thrust created for the same nozzle and conditions, but frictionless and without divergence losses. For the friction losses a friction coefficient equal to 0.005 was used, which is the value for commercial steel pipe with the standard wall roughness of 0.046 mm (John and Keith, 2006; Perry et al., 1997).

4.2 Experimental set up

Jet penetration experiments were conducted in a small fluidized bed with a height of 0.90 cm, and a rectangular cross sectional area of 0.10 m by 0.50 m (Fig. 4.6). All experimental runs used fresh silica sand with a Sauter mean diameter of 200 μm, and the height of the static bed was 0.22 m. The supersonic nozzle was located on the side of the bed, 0.10 m above the porous plate distributor with the nozzle tip penetrating 0.03 m from the wall. The fluidization superficial gas velocity was kept constant at 0.09 m/s for all the runs, corresponding to approximately 3.6 times the minimum fluidization velocity for the silica sand used.

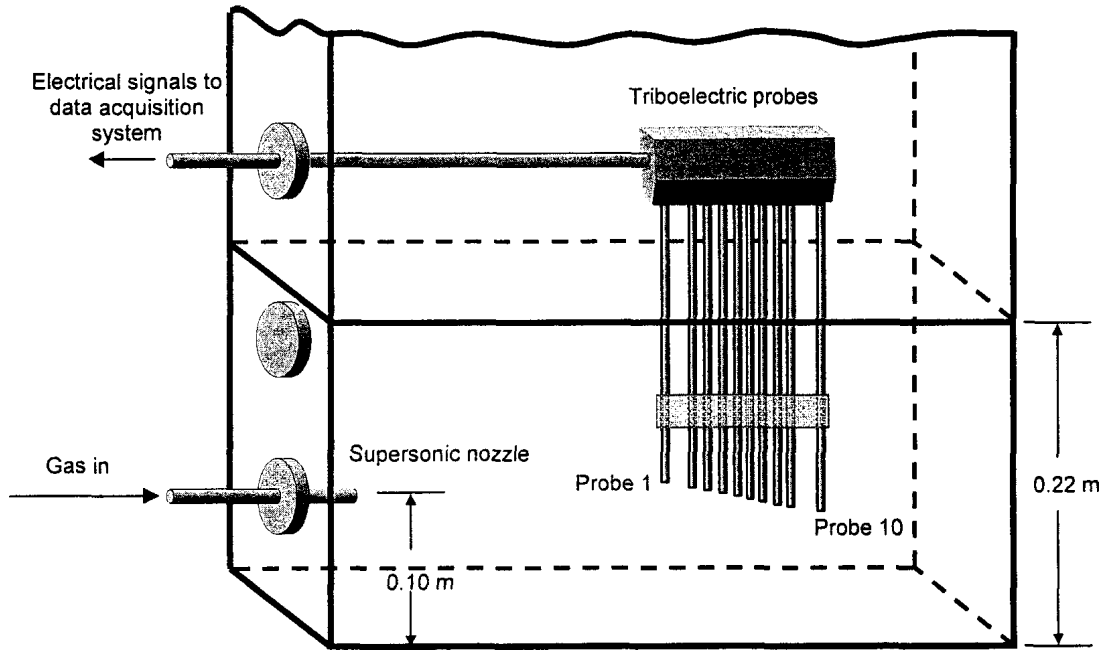

Figure 4.6: Schematic of the fluidized bed and the triboelectric probes.

Jet penetration length was measured with an arrangement of 10 triboelectric probes, and the method was taken from Dawe et al. (2008), although the triboelectric probes were arranged in a different way for this research. This technique uses the phenomenon known as tribo-charging in which charges are exchanged whenever any two surfaces come into contact with each other, and a net charge will be created on each of

the surfaces when they are separated. That occurs with conductors, semiconductors or insulators; solids or liquids; and even for cases where the bulk materials are the same (Castle, 1997). The objective with the triboelectric probe technique is to measure just the current created by contact between high velocity, entrained particles in the gas jet and a metal probe tip.

The triboelectric probes were made with a brass pipe with an electrical wire inside as shown in Figure 4.7. The brass pipe was grounded, and the internal wire was insulated except for one end that was attached to the stainless steel tip that was in contact with the moving silica sand particles. The exposed length of the metal tips was 0.007 m. The tips of the probes were not horizontally aligned because it was found that if they were in the same horizontal line, the signal of each probe was affected by the probes located upstream. The horizontal level difference was small and its maximum value was 0.01 m between the first and the last probe. The distance between probes 1 and 2, and probes 9 and 10 was 0.015 m, and a 0.005 m spacing was used for the remaining probes.

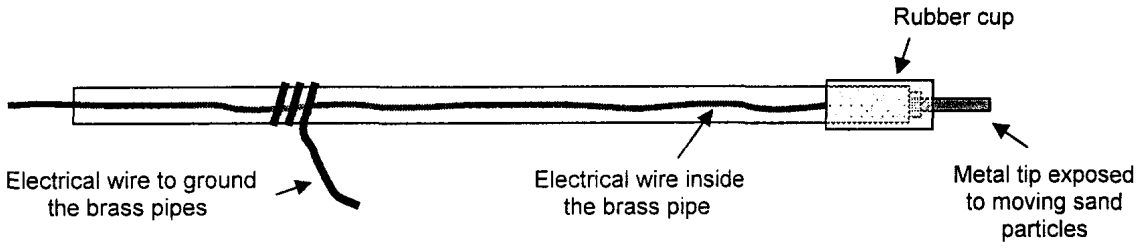

Figure 4.7: Representation of the triboelectric probes used.

The electrical current, generated by the friction between the metal tip of each probe and the silica sand, resulting from the presence of the gas jet, was sent to an amplifier that converted the signal to a voltage. A data acquisition system collected the voltage signal at a frequency of 1000 Hz.

Air, helium and carbon dioxide were used for jet penetration experiments and the relative gas pressures to feed the nozzles were between 193 and 1930 kPa (28 and 280

psig). The characteristics of the supersonic nozzles used in the experiments are shown in Figures 4.8 to 4.11.

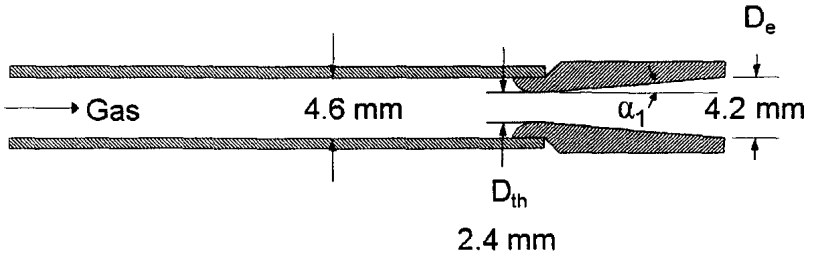

Figure 4.8: A1 nozzle.

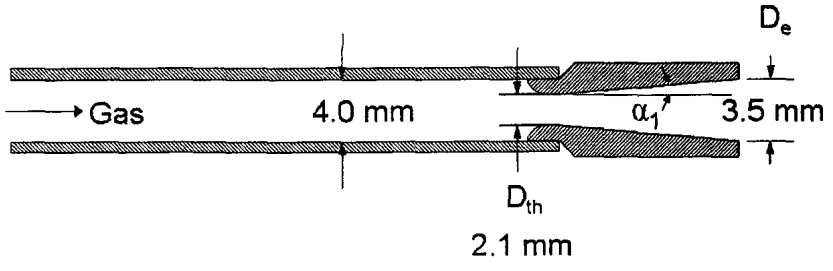

Figure 4.9: A2 nozzle.

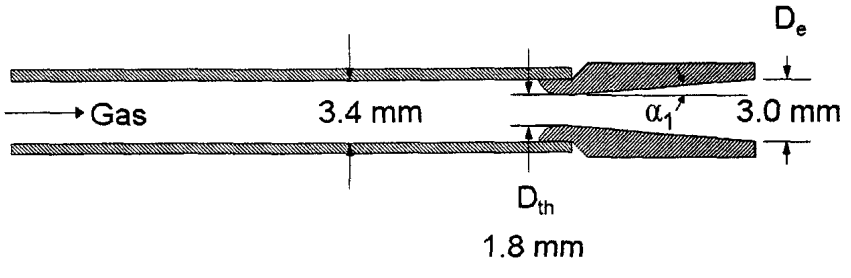

Figure 4.10: A3 nozzle.

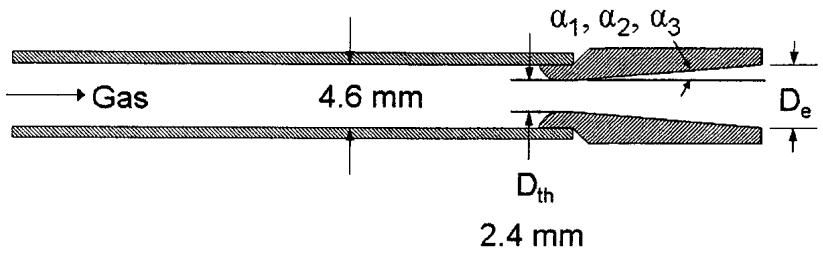

Figure 4.11: B, D, G and F nozzles.

One of the most important features of the previous convergent-divergent nozzles is the divergent angle, and three different angles were used, depending on the nozzle type. Nozzle A1, A2 and A3 had the same shape but different measurements, and nozzles B, D, G and F had different geometries. The characteristics of the nozzles and the operating pressures are listed in Table 4.2.

For the initial runs under each operating condition, the distance from the closest probe to the tip of the nozzle was around 0.10 m farther than the estimated penetration. It was found that, for these initial distances, the voltage signal was similar to the signal without gas injection. Then, the nozzle was progressively moved closer to the probes by increments of 0.015 m and, at some point, the signal for the first probe started increasing, showing that the particles entrained by the gas jet were hitting the metal tip of this probe. Usually the second probe did not show any change at this point, but with an additional distance reductions each subsequent probe started increasing its voltage signal. As expected, when the gas jet was touching all the probes, the highest voltage signal was between the first and the second probe, and the lowest voltage was for the last probe.

Collection of data for single jet penetration measurements was done over a period of 30 seconds, with gas injection in the sonic nozzle starting at 10 seconds and finishing at 27 seconds. The recorded signal from 18 to 25 seconds was used for analysis and calculation of jet penetration. For high gas pressures, this injection time was enough to substantially grind the silica sand particles, and the sand was replaced after each 30 second run to keep a constant particle size distribution

Table 4.2: Critical measurements of the convergent-divergent nozzles, and attrition pressures used.

Attrition Gas	Nozzle Type	Nozzle throat diameter D_{th}(mm)	Nozzle exit diameter D_e (mm)	Half angle α	Relative upstream pressure kPa (Gauge)
Air	A1	2.4	4.2	α_1	676, 1275, 1930
Helium	A1	2.4	4.2	α_1	1275
CO_2	A1	2.4	4.2	α_1	1275
Air	A2	2.1	3.5	α_1	676, 1275, 1930
CO_2	A2	2.1	3.5	α_1	1137
Air	A3	1.8	3.0	α_1	676, 1275, 1930
Helium	A3	1.8	3.0	α_1	676
CO_2	A3	1.8	3.0	α_1	331
Air	B	2.4	4.7	α_1	676, 1275, 1930
CO_2	B	2.4	4.7	α_1	1275
Air	D (C	2.4	2.8	α_1	676, 1275, 1930
Air	G (D	2.4	4.9	α_2	676, 1275, 1930
Air	F (E	2.4	3.2	α_3	676, 1275, 1930
Helium	F (E	2.4	3.2	α_3	1275
CO_2	F (E	2.4	3.2	α_3	193, 1275

4.3 Results and discussion

Absolute values of the probe signals at 100 Hz are shown in Figure 4.12. In that graph, the difference between the signal during simple fluidization and after the injection of the gas jet is very clear. For the particular case of Figure 4.12, the data show that the jet is touching probes 1 to 4.

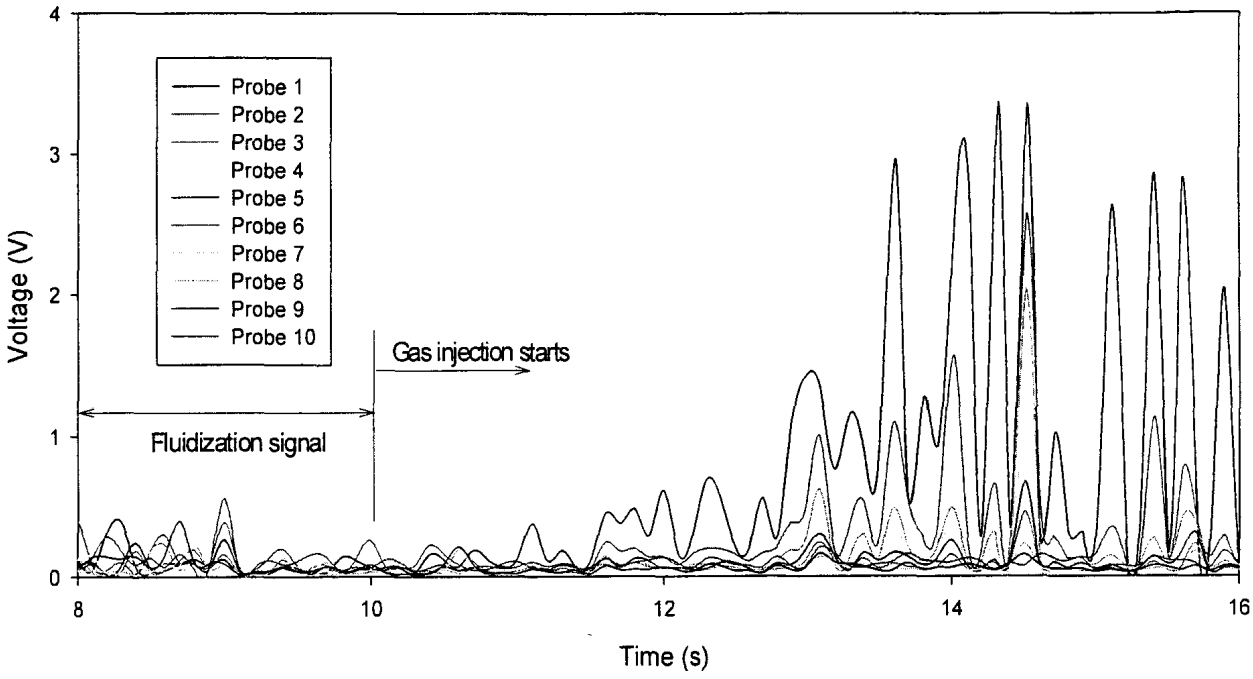

Figure 4.12: Absolutes values of the recorded signal at 100 Hz.

Several signal analysis methods were attempted to calculate jet penetration, and cycle analysis using the V statistic gave the best results (Briens, L. A., and Briens, C. L., 2002). Average cycle amplitude versus jet penetration distance is shown for each probe in Figure 4.13. These results have been obtained using the G type nozzle with air injected at a total pressure of 1275 kPa. The experimental data using the triboelectric probes shows that the gas jet started touching the probes at 0.305 m. The second probe signal was used to develop an analytical calculation for the determination of the jet penetration since this probe gave a clean and strong signal.

The analytical method utilized in this work was very simple, and consisted of fitting a curve using the variation of the average cycle amplitude with distance from nozzle tip from the second probe signal. The absolute value of the slope of this curve was close to zero when the jet was not touching the probe, and started increasing once there was contact with the jet. It was noticed that when the absolute value of the slope was -0.012, the values for jet penetration were very similar to the values that were estimated

visually from the average cycle amplitude versus distance graphs. Utilizing this criterion, the same slope value was used to estimate the value of the jet penetration depth for all the experimental runs. It is shown in Figures 4.13 and 4.14 that the analytical calculation for penetration is 0.305 m.

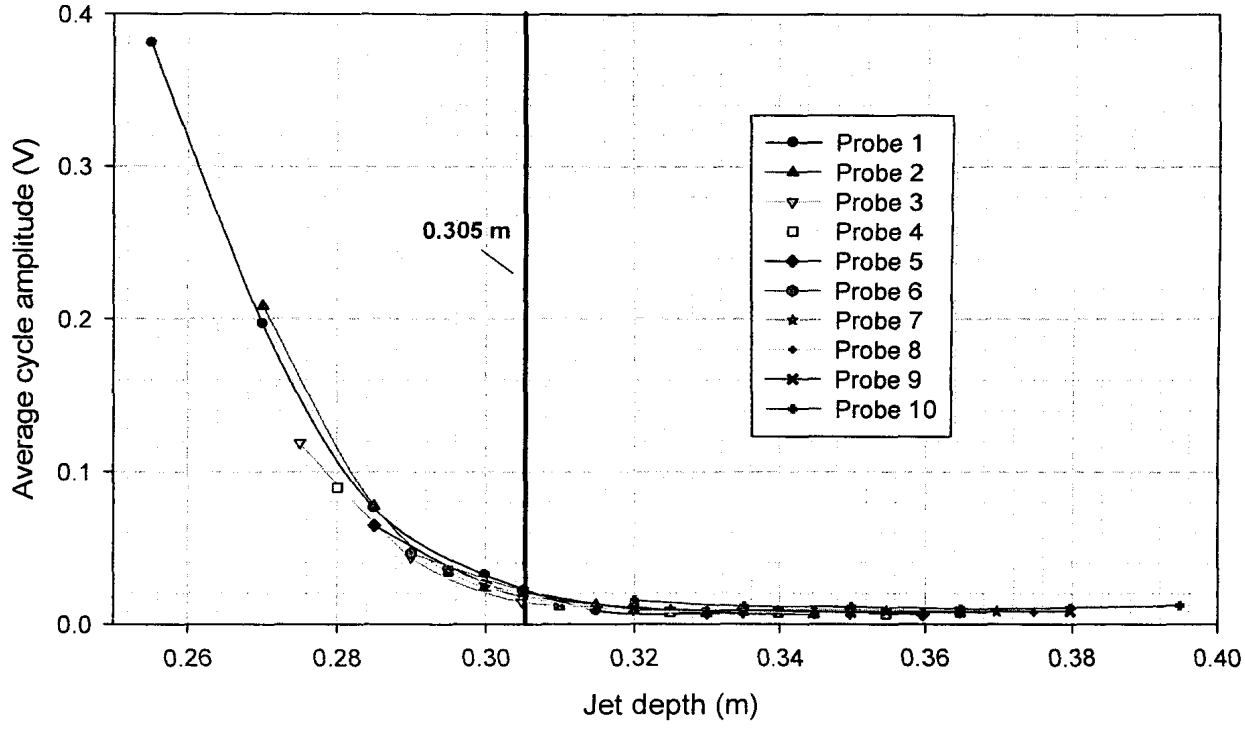

Figure 4.13: Average cycle amplitude versus penetration distance for each probe when injecting air at 1275 kPa and using the G nozzle.

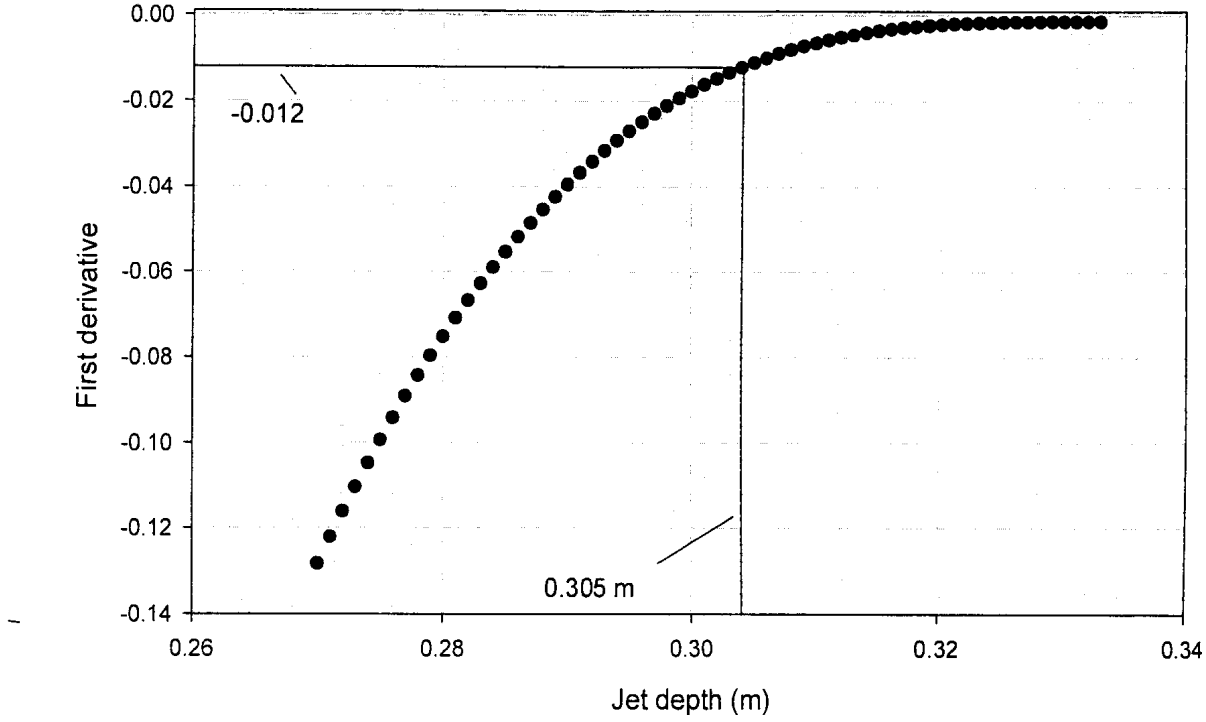

Figure 4.14: First derivative of the fitted curve for the average cycle amplitude using the second probe versus jet depth.

The calculated jet penetration depths and thrusts are strongly correlated, as shown in Figure 4.15, and this applies to all the gases and nozzles used in this work. Equation 4.11 fits the results with a correlation coefficient of 0.992, where jet penetration and thrust are given in meters and Newtons, respectively.

$$L_{jet} = \frac{0.2257 * F}{0.1695 + F} + 0.01149 * F \qquad (4.11)$$

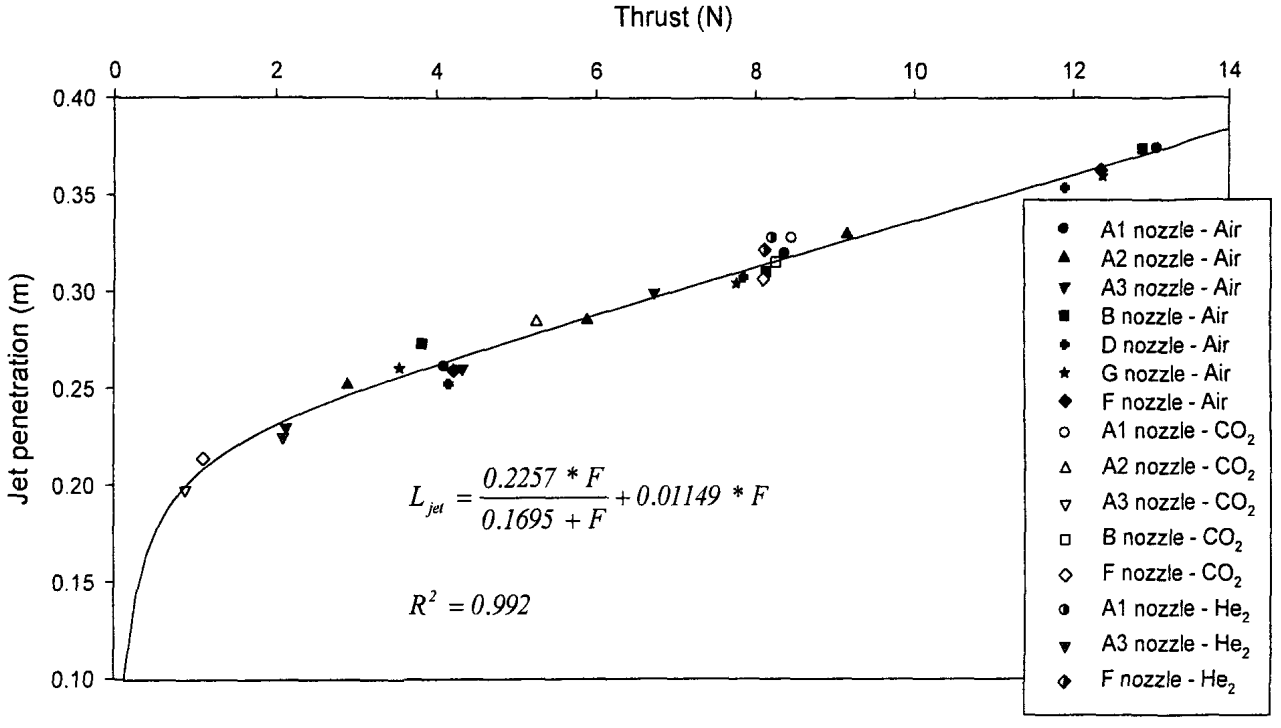

Figure 4.15: Jet penetration versus thrust for all the nozzles and gases.

There is also a good correlation between the experimental results and the jet momentum, as illustrated in Figure 4.16, and the derived correlation (Equation 4.12) shows a correlation coefficient of 0.968.

$$L_{jet} = \frac{0.2298 * M}{0.3572 + M} + 0.0114 * M \qquad (4.12)$$

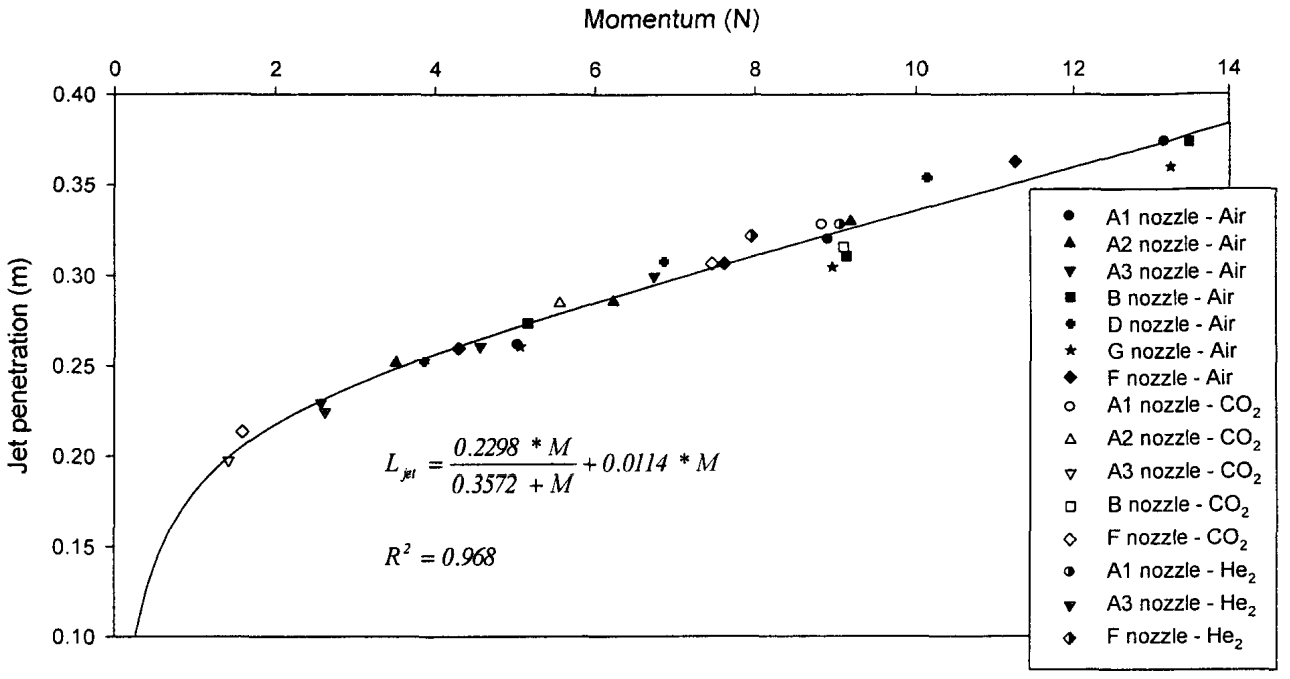

Figure 4.16: Jet penetration versus momentum for all the nozzles and gases.

It is observed in the previous two graphs that momentum fits better the data for short jet penetration lengths, and that thrust fits really well the data corresponding to the longest jet penetration distances. Figure 4.17 represents the combination of thrust and momentum versus experimental jet penetrations, calculated as the addition of 30% momentum and 70% thrust. These percentages were obtained empirically, using an iterative procedure to maximize the correlation coefficient. Equation 4.13 resulted from this momentum-thrust combination, with a correlation coefficient of 0.994, which represents an improvement over Equation 4.11.

$$L_{jet} = \frac{0.2274 * (\dot{m}U_e + 0.7(p_e - p_o)A_e)}{0.3312 + (\dot{m}U_e + 0.7(p_e - p_o)A_e)} + 0.01163 * (\dot{m}U_e + 0.7(p_e - p_o)A_e) \qquad (4.13)$$

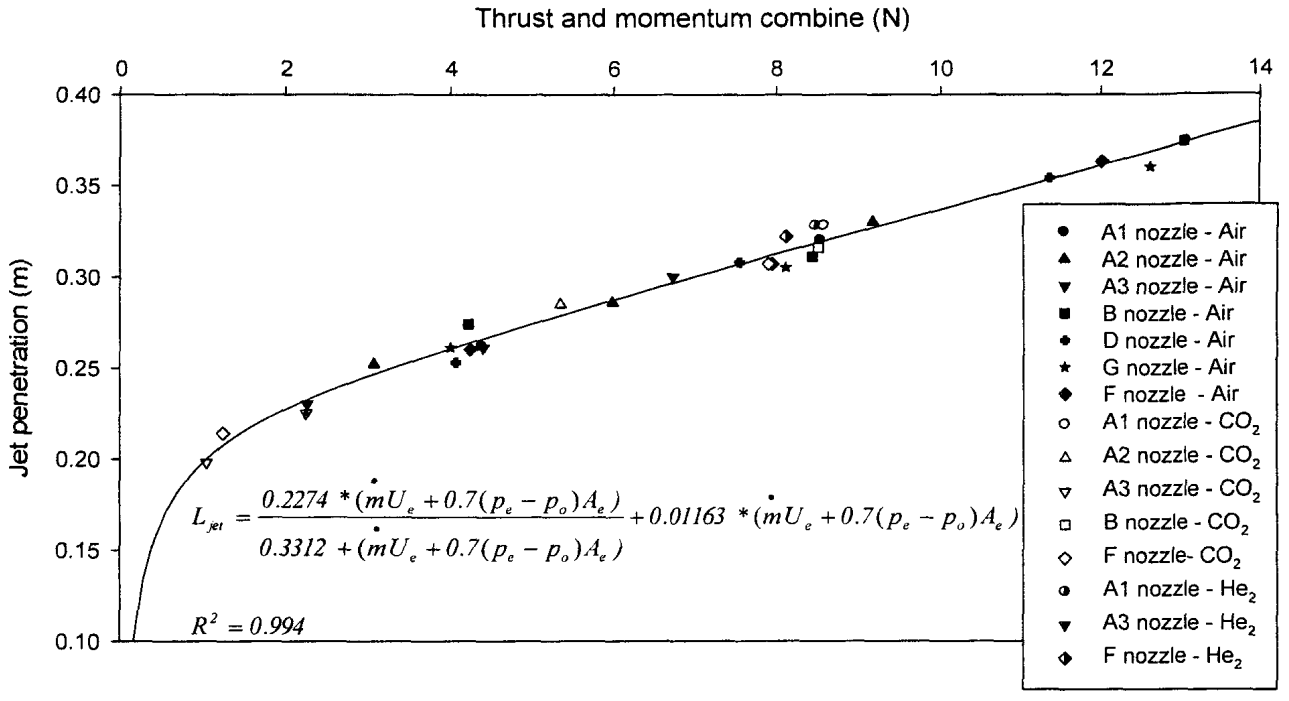

Figure 4.17: Jet penetration versus combination of thrust and momentum. This combination is calculated using Equation 13.

For a given gas and nozzle geometry, the exit velocity of the gas jet is the same regardless of the gas pressure as long as there is supersonic flow at the nozzle exit, and it is suspected that this may explain why momentum fits better with short jet penetrations. Probably for short penetration distances, the gas jet has less time and length to fully develop the effects of underexpansion or overexpansion of the supersonic jet, and maybe that is not the case for the longer jets. In all cases, the results show that thrust can be used to predict gas jet penetration, and the correlation presented in this study is limited to the operating conditions mentioned at the beginning, i.e. silica sand with a Sauter mean diameter of 200 μm, and a fluidization velocity of 0.09 m/s. The momentum-thrust combination is slightly better to predict jet penetration than thrust.

This finding seems logical, since thrust is the force given by the supersonic gas jet at the nozzle exit, and this thrust takes into account the mass flow rate and the nozzle exit velocity and pressure. The mass flow rate depends on the gas used, on the nozzle throat diameter, and on the gas injection pressure and temperature. The exit velocity and pressure vary according to the expansion ratio between the exit and throat areas. As it

was stated in the introduction section, the expansion angles used in this study are close to an optimum range of values if friction and axial momentum losses are considered, and it seems that the experimental results in this work confirm this. If these angles were too small or too big, significant losses in momentum and thrust would occur, and the momentum and thrust calculated using Equations 4.1 to 4.6 would not fit well the experimental results for jet penetration. In that case, Equations 4.8 to 4.10 would have to be used to calculate momentum and thrust, and Equation 4.7 would correct thrust for axial momentum loss.

Another interesting result is that different gases at equal injection pressure give similar thrust and momentum values and jet penetration distances. Helium produces higher exit velocities than air, due to its lower molecular weight, but, at the same time, its mass flow rate is lower than the one for air, and the combination of these two variables gives similar thrust values for air and helium. A similar analysis can be done for air and carbon dioxide.

Comparison of experimental jet penetrations with values predicted using the correlations presented in the introduction section show that the Merry's correlation gives penetration depths that are very close to experimental results (Fig. 4.18). The correlations by Yates et al. (1988) and by Benjelloun et al. (1995) produce acceptable values, while those by Zenz (1968) and Hong et al. (2003) predict jet depths that are far from the experimental penetration distances. All the previous correlations were developed for subsonic gas jets, and that may explain the observed errors. Besides, these correlations were generated using different fluidization velocities and, as stated by Ariyapadi et al. (2003) and Chyang et al. (1997), fluidization velocity affects jet penetration.

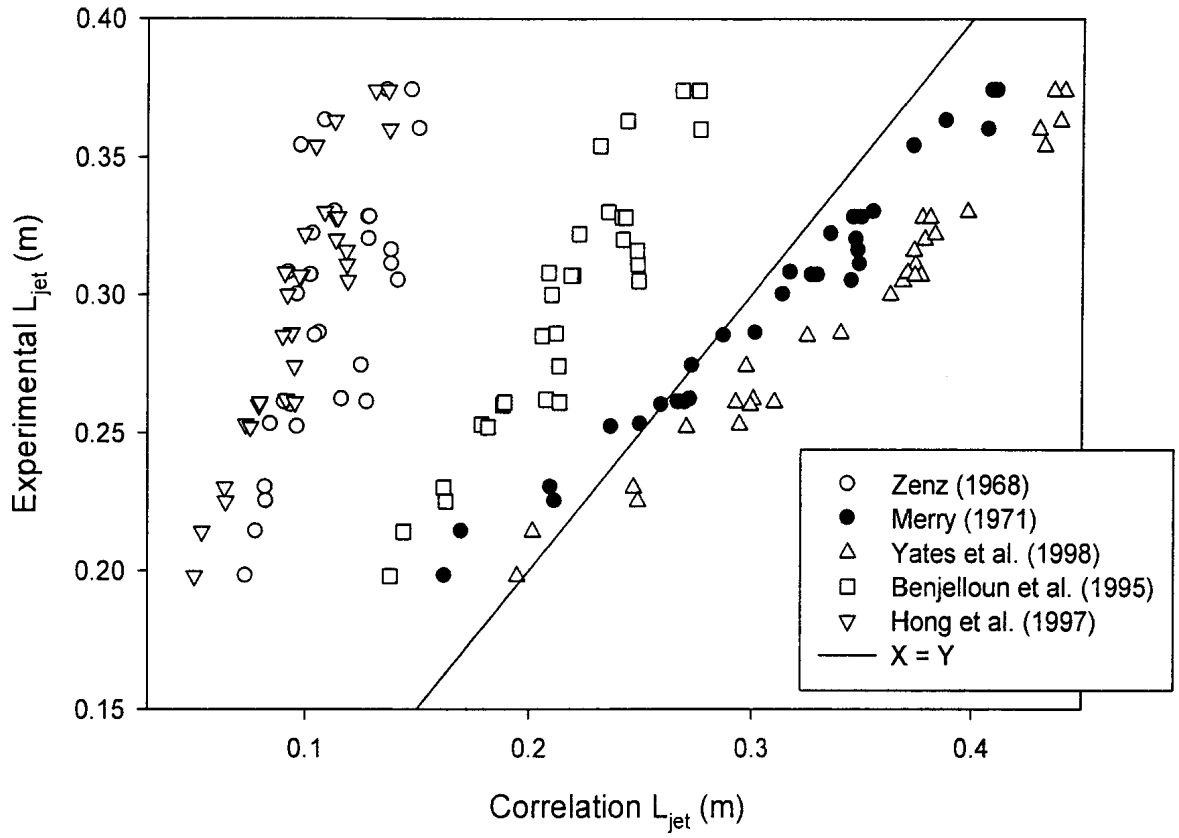

Figure 4.18: Predicted jet penetration distances using different correlations versus experimental results.

Ariyapadi et al. (2004) used a correction factor for nozzle geometry to modify the Benjelloun's correlation, and, in this study, it was found that by introducing a similar correction factor to the same correlation, the predicted jet penetration depths are the closest to the experimental results. The numerical values of this correction factor are obtained when dividing the experimental gas jet penetrations by the predicted values when using the original Benjelloun's correlation:

$$C_g = \frac{Experimental\ \ jet\ \ penetration}{Predicted\ \ jet\ \ penetration\ using\ \ Benjelloun's\ \ correlation} \tag{4.14}$$

Examination of the data showed that there is a strong relationship between the correction factor and the nozzle exit diameter as illustrated in Figure 4.19, and this relationship can be represented by Equation 4.15, with D_e in meters:

$$C_g = 1.72 - 93.06 * D_e \tag{4.15}$$

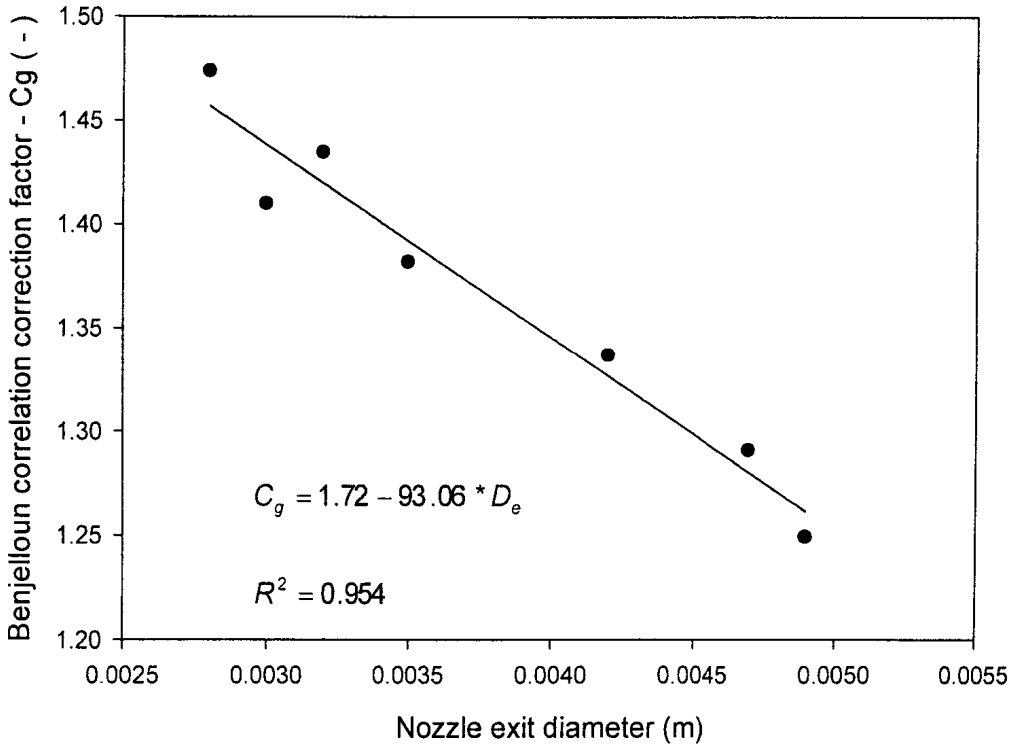

Figure 4.19: Correction factor for the Benjelloun's correlation.

As expected, when multiplying the gas jet penetrations predicted by the original Benjelloun correlation by the C_g values calculated using Equation 4.15, it is found that the corrected values of jet penetration are very close to the experimental values, as shown in Figure 4.20.

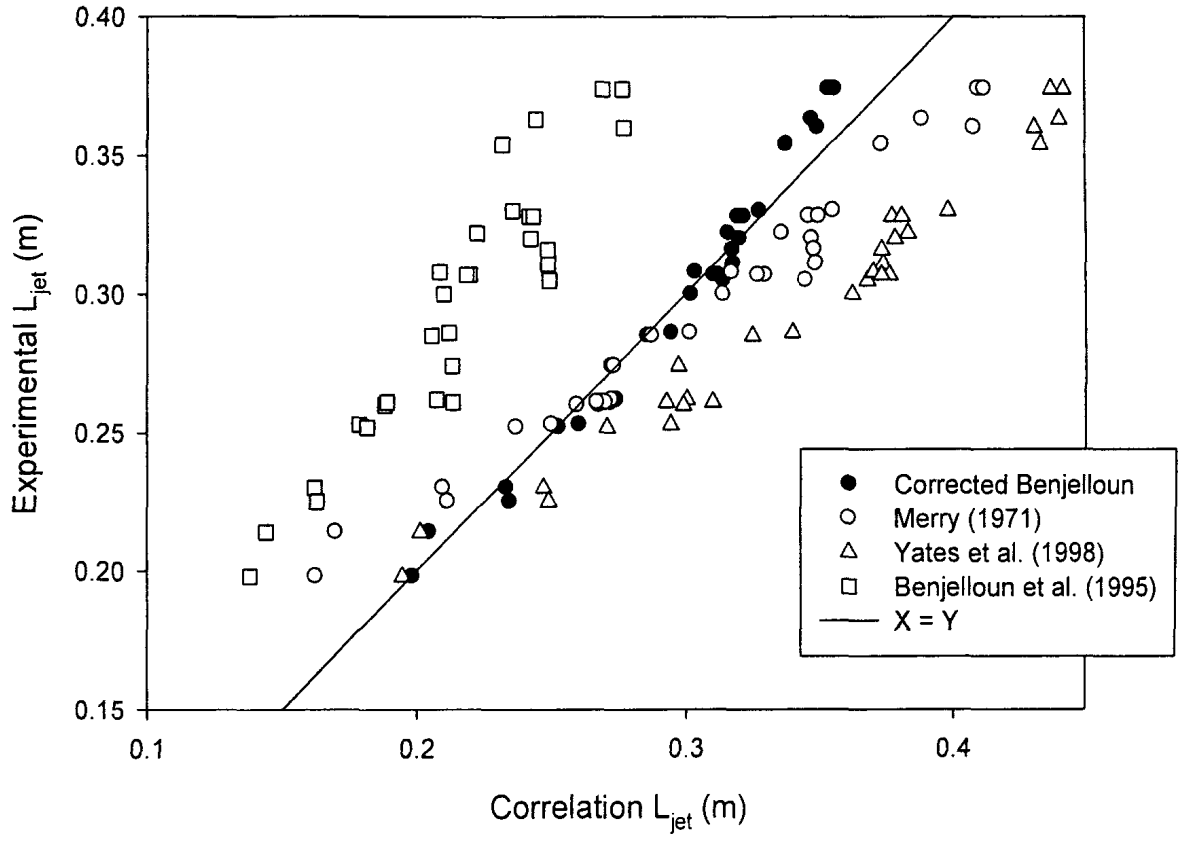

Figure 4.20: Comparison between the predicted jet penetrations using the modified Benjelloun's correlation and other correlations.

The jet penetrations calculated with the modified Benjelloun's correlation are given by Equation 4.16.

$$\frac{L_{jet}}{D_e} = 5.52\left[\frac{\rho_e U_e^{\,2}}{(\rho_p - \rho_e) g D_e}\right]^{0.27} * C_g \tag{4.16}$$

By replacing C_g with Equation 4.15, the modified Benjelloun's correlation can be written as:

$$\frac{L_{jet}}{D_e} = 5.52\left[\frac{\rho_e U_e^{\,2}}{(\rho_p - \rho_e) g D_e}\right]^{0.27} * (1.72 - 93.06 * D_e) \tag{4.17}$$

It is expected that the previous modified correlation may work as a general correlation to predict horizontal gas jet penetration into gas-solid fluidized beds. However, the effect of operating parameters on the correction factor predicted by Equation 4.15 would have to be determined.

As it was mentioned before, the objective of this study was to show the relationship between thrust and gas jet penetration when working with supersonic nozzles. To develop a new general correlation, more experiments would be required using different fluidization velocities, bed particles, and fluidization gases.

4.4 Conclusions

Supersonic nozzles with different geometries were used to inject horizontal gas jets into a laboratory-scale solid-gas fluidized bed. The gases injected into the nozzles were air, helium and carbon dioxide, and the jet penetration lengths of the resulting gas jets were measured with a set of triboelectric probes. For all gases used in this study, it was found that the jet penetration showed a strong correlation with thrust, and a good relationship with momentum, especially for short jet penetration distances.

The jet penetration values predicted when using the Benjelloun's correlation, modified by introducing a correction coefficient dependent on the nozzle exit diameter, are the closest to the experimental results.

4.5 Nomenclature

A_e Area at the nozzle exit (m^2)

A_{th} Area at the nozzle throat (m^2)

C_g Correction factor for Benjelloun's correlation (-)

D Diameter (m)

D_e Diameter at the nozzle exit (m)

D_{th} Diameter at the nozzle throat (m)

d_p Sauter mean particle diameter (m)

f Friction coefficient (-)

F Thrust (N)

L_{jet} Jet penetration depth (m)

M Momentum

$\dot{m}$ Mass flow rate of gas (kg/s)

M_e Mach number at nozzle exit (-)

M_{th} Mach number at nozzle throat (-)

p_e Gas pressure at the nozzle exit (kPa)

p_t Total pressure (kPa)

p_{th} Gas pressure at the nozzle throat (kPa)

p_o Background pressure (kPa)

R Gas constant (Nm/moles/K)

T_e Gas temperature at the nozzle exit (K)

T_t Total temperature (K)

T_{th} Gas temperature at the nozzle throat (K)

U_e Gas velocity at the nozzle exit (m/s)

U_{eq} Equivalent velocity (m/s)

U_{th} Gas velocity at the nozzle throat (m/s)

V Voltage (V)

Greek letters

α Half angle of the sonic nozzle (degrees)

ε Bed voidage (-)

γ Specific heat ratio of the gas (-)

ρ_e Gas density at the nozzle exit

ρ_p Bed particles density (kg/m^3)

ρ_{th} Gas density at the nozzle throat (kg/m^3)

λ Correction factor for axial momentum loss (-)

4.6 References

Abdulhadi, M., "Dynamics of compressible air flow with friction in a variable-area duct", *Wärme – und Stoffübertragung*, **22** 169-172 (1988).

Ariyapadi, S., Berruti, F., Briens, C., McMillan, J., and Zhou, D., "Horizontal Penetration of Gas-Liquid Spray Jets in Gas-Solid Fluidized Beds", *Int. J. Chem. Reactor Eng.*, **2** Article A22 (2004).

Ariyapadi, S., Holdsworth, D. W., Norley, C. J. D., Berruti F., and Briens, C., "Digital X-ray Imaging Technique to Study the Horizontal Injection of Gas-Liquid Jets into Fluidized Beds", *Int. J. Chem. Reactor Eng.* **1** Article A56 (2003).

Benjelloun, F., Vanderschuren, J., and Liegeois, R., "Penetration Length of Horizontal Gas Jets into Atmospheric Fluidized Beds", *Proc. Fluidization-VIII, J-F.* Large and C. Laguerie Eds., Engineering Foundation, N.Y., 239-246 (1995).

Briens, L. A., and Briens, C. L., "Cycle Detection and Characterization in Chemical Engineering", *AIChE J.*, **48** 970-980 (2002).

Chyang, C. S., Chang, C. H., and Chang J. H., "Gas Discharge Modes at a Single Horizontal Nozzle in a Two-Dimensional Fluidized Bed", Powder Technol., **90** 71-77 (1997).

Dawe, M., Briens, C., and Berruti, F., "Study of Horizontal Sonic Gas Jets in a Gas-Solid Fluidized Beds", *Can. J. Chem. Eng.*, **86** 506-513 (2008).

Hong, R. Y., Guo, Q. J., Luo, G. H., Zhang, J. Y., and Ding, J., "On the Jet Penetration Height in Fluidized Beds with Two Vertical Jets", *Powder Technol.*, **133** 216-227 (2003).

Hong, R., Li, H., Li, H., and Wang Y., "Studies on the Inclined Jet Penetration Length in a Gas-Solid Fluidized Bed", *Powder Technol.* **92** 205-212 (1997).

John, J. E., and Keith, T. G., *Gas dynamics*, Pearson Prentice Hall, 3rd edn., 68-102 and 283-331 (2006).

Li, T., Pougatch, K., Salcudean M., and Grecov D., "Numerical Simulation of Horizontal Jet Penetration in a Three-Dimensional Fluidized Bed", *Powder Technol.*, **184** 89-99 (2008).

Luo, G., Zhang, J.-Y., Guo, Q., and Zhang B., "Study on Jet Flow from Two Vertical Nozzles in a 500 mm I. D. Semi-Circular Fluidized Bed", *Chem. Eng. Technol.*, **22** 247 – 251 (1999).

Merry J. M. D., "Penetration of a Horizontal Gas Jet into a Fluidised Bed", *Trans. Inst. Chem. Eng.* **49** 189-195 (1971).

Merry, J. M. D., "Penetration of Vertical Jets into Fluidized Beds", *AIChE J.*, **21** 507-510 (1975).

Perry, R. H., Green, D. W., and Maloney J. O., *Perry's Chemical Engineers' Handbook*, McGraw-Hill, 7th edn. 6-25–6-26 (1997).

Sutton, G. P., and Biblarz, O., *Rocket Propulsion Elements*, John Wiley & Sons, Inc, 7th edn., 32, and 77-82 (2001).

Vaccaro, S., "Analysis if the Variables Controlling Gas Jets Expansion Angles in Fluidized Beds", *Powder Technol.* **92** 213-222 (1997).

Yang, W.-C., and Keairns, D. L., "Estimating the Jet Penetration Depth of Multiple Vertical Grid Jets", *Ind. Eng. Chem. Fundam.*, **18** 317-320 (1979).

Yates, J. G., Cobbinah, S.S., Cheesman, D. J., and Jordan S. P., "Particle Attrition in Fluidized Beds Containing Opposing Jets", *AIChE Symp.* Ser. 281 13-19 (1988).

Zenz, F. A., "Bubble Formation and Grid Design", *Inst. Chem. Eng. Symp.* Ser. 30 136-139 (1968).

CHAPTER 5

General Discussion

This chapter shows how the three studies of this thesis are linked. It discusses the results and the most important contributions to the field.

5.1 Connections between chapters

Gas-solid fluidized beds have many industrial applications, and some of those applications use attrition nozzles with the objective of reducing the size of the bed particles. Fluid coking is one of the processes where attrition nozzles control the size of coke particles in a gas-solid fluidized bed, and this is done to maintain good fluidization (McMillan et al., 2007b). This research emphasizes the optimization of the attrition nozzles in the fluid coking process, and foresees a possible application of the same attrition principles for green sand reclamation. Optimization of attrition nozzles is critical in the fluid coking process to reduce consumption of the attriting gas and, thus, increase equipment throughput. Similar benefits can be expected in the green sand reclamation process.

The main difference between these two particular applications is that for fluid coking, the desired attrition mechanism is fragmentation, and abrasion is not desired since this produces fine particles that adversely affect fluidization. In green sand reclamation, abrasion is preferred because this attrition mechanism removes the outer layer of the attrited particles. In other words, abrasion is ideal to reclaim green sand since this will remove the external coating of clay and carbonaceous material that is attached to the silica sand particles which are the main component in the green sand. Fragmentation is not desired because it will change drastically the particle size distribution of the green sand and shift it away from its ideal range.

To determine the effectiveness of the green sand reclamation method four measurements were done: clay or oolitic content, organic content, acid request, and particle size distribution. In the case of nozzle optimization experiments, the key measurement was the grinding efficiency which is the new surface area created per unit of mass of the attrition gas used.

This research also studied the penetration of attrition jets into a gas-solid fluidized, and these experiments were done because it is important to understand the interaction between gas jets and fluidized beds, and calculation of the jet penetration depth is a key characteristic in fluidized bed design since jets may impact and erode bed internals.

5.2 Chapter 2

Green sand reclamation using a gas-solid fluidized bed and an attrition nozzle can be considered as an innovative method to separate clay and organic material from silica sand. Green sand is already being reused several times for mold making casting, however for core making operations a reclamation process is required (Zanetti and Fiore, 2002). Current methods for green sand reclamation are not that effective since they use particle to surface collisions or mills for grinding, and this requires constant replacement of eroded parts. Some methods even create waste waters and the associate complications with its treatment and disposal. The proposed technique in this research uses attrition jets into the gas-solid fluidized where just particle to particle collisions occur. Fluidization allows for good mixing of the green sand, and uniform calcination of particles if this is required. Additionally, most of the separated clay and organic material can be removed by elutriation or segregation.

Preliminary experiments show that this method may work, and that the biggest challenge is the removal of clay from the silica sand since there is a strong bond between these two. Calcination of green sand makes easier that separation, and the reasons for this can be that high temperatures make the bond weaker and the clay more brittle. A disadvantage of calcination is the energy consumption, and the requirement of high temperature equipment. However, it was estimated that green sand reclamation combine with calcination may be economically feasible if the reclaim green sand has similar properties to the original sand.

Since this was a preliminary test, the attrition nozzle used for these experiments was a straight nozzle with a diameter of 4.6 mm, and this nozzle gives a maximum

velocities equivalent to the speed of the sound. No more nozzles were utilized during experimentation, but it is expected that process can be greatly improved by using more efficient nozzles. The results from nozzle optimization study can be applied to green sand reclamation if further research on this possible application is desired.

5.3 Chapter 3

As it was mentioned earlier the objective of particle size reduction experiments was the optimization of the supersonic attrition nozzles used in the fluid coking process, however, this is beneficial for any process that uses this kind of nozzles to attrite particles. Therefore, this also applies to green sand reclamation if the proposed method is going to be used at industrial level.

Nozzle optimization was focused on convergent-divergent or Laval-type nozzles, and for this several attrition gases were used at pressures between 138 and 2550 kPa. Similar to green sand reclamation experiments, fluidization velocity, fluidizing gas, and bed particles were the same during all experimental runs.

It was found that grinding efficiency increases with nozzle size, attrition pressure, and by decreasing the molecular weight of the attriting gas. In general these results are similar to the ones from previous studies (McMillan et al., 2007a; Palaniandy et al., 2008; Midoux et al., 1999). A few experimental runs were done with a straight nozzle to compare grinding results with the Laval-type nozzles, and as expected the straight nozzles are less efficient than the convergent-divergent nozzle (McMillan et al., 2007a). This is an indication that the consumption of the attrition gas for green sand reclamation can be reduced and that reclamation results can be improved.

It was shown that thrust produced in the supersonic nozzles is related to the grinding efficiency, and a correlation was calculated.

$$\eta_{pred.} = \frac{\frac{(-3.849 + 9.842 * F)}{(1 + 0.069 * F)}}{\left(\frac{U_{eq.gas}}{U_{eq.air}}\right)^{0.61}\left(\frac{\rho_{gas}}{\rho_{air}}\right)} \quad (5.1)$$

This correlation fits well the experimental data with a correlation coefficient of 0.978, and it is valid for the experimental conditions used, that is, fluidization velocity of 0.18 m/s, a weight of 25.0 kg of silica sand particles with a Sauter mean diameter of 200 μm, and air as fluidizing gas. Thrust and equivalent velocities values take into account the nozzle size and geometry, attrition pressure and background pressure. To apply Equation 5.1 to different gases a correction factor was introduced and it uses the ratio of equivalent velocities and densities with air considered as the base gas, as shown in that equation.

In general it was found that at high attrition pressures more fines were produced and, as expected, the original bed particles left in the bed were smaller.

5.4 Chapter 4

The method used to calculate gas jet penetration is the one utilized by Dawe et al. (2008), and this technique proved to be appropriate. Similar to grinding efficiency, it is found that jet penetration is related to thrust, and it also has a relationship with momentum and with the combination of thrust-momentum. Equations 2, 3 and 4 show the correlations for these relationships.

$$L_{jet} = \frac{0.2257 * F}{0.1695 + F} + 0.01149 * F \quad (5.2)$$

$R^2 = 0.992$

$$L_{jet} = \frac{0.2298 * M}{0.3572 + M} + 0.0114 * M \tag{5.3}$$

$R^2 = 0.968$

$$L_{jet} = \frac{0.2274 * (Combine\ F\ and\ M)}{0.3312 + (Combine\ F\ and\ M)} + 0.01163 * (Combine\ F\ and\ M) \tag{5.4}$$

$R^2 = 0.994$

$$Combine\ F\ and\ M = 0.3 * M + 0.7 * F = \dot{m} U_e + 0.7(p_e - p_o)A_e \tag{5.5}$$

These correlations are valid for the conditions used during experimentation, or in other words, they do not considered variations in fluidization velocity, and bed particles properties. Comparable to particle size reduction experiments, the correlations take into consideration convergent-divergent nozzle size, nozzle geometry, type of gas and pressure of the gas to feed the supersonic nozzles.

During data analysis it was noticed that the Benjelloun's correlation (1995) fits very well the experimental data when modifying that correlation with a correction factor. This factor considers the variation in nozzle exit diameter as is represented with Equation 6.

$$C_g = 1.72 - 93.06 * D_e \tag{5.6}$$

The modified Benjelloun's correlation is given by Equation 7, and the values predicted by this correlation and very close to the values predicted by equations 2 to 4. The main difference is that the modified Benjelloun's correlation takes into account changes in the bed particles density.

$$\frac{L_{jet}}{D_e} = 5.52\left[\frac{\rho_e U_e^{\,2}}{(\rho_p - \rho_e) g D_e}\right]^{0.27} * (1.72 - 93.06 * D_e) \qquad (5.7)$$

5.5 Nomenclature

A_e Area at the nozzle exit (m^2)

C_g Correction factor for Benjelloun's correlation (-)

D_e Diameter at the nozzle exit (m)

F Thrust (N)

L_{jet} Jet penetration depth (m)

M Momentum

$\dot{m}$ Mass flow rate of gas (kg/s)

U_e Gas velocity at the nozzle exit (m/s)

U_{eq} Equivalent velocity (m/s)

p_e Gas pressure at the nozzle exit (kPa)

p_o Background pressure (kPa)

Greek letters

ρ_e Gas density at the nozzle exit

ρ_p Bed particles density (kg/m^3)

$\eta_{pred.}$ Predicted grinding efficiency (m^2/kg)

5.6 References

Benjelloun, F., Vanderschuren J., and Liegeois, R., "Penetration Length of Horizontal Gas Jets into Atmospheric Fluidized Beds", *Proc. Fluidization-VIII, J-F. Large and C. Laguerie Eds., Engineering Foundation, N.Y.*, 239-246 (1995).

Dawe, M., Briens, C., and Berruti, F., "Study of Horizontal Sonic Gas Jets in a Gas-Solid Fluidized Beds", *Can. J. Chem. Eng.*, **86** 506-513 (2008).

McMillan, J., Briens, C., Berruti, F., and Chan, E., "High Velocity Attrition Nozzles in Fluidized Beds", *Powder Technol.*, **175** 133-141 (2007a).

McMillan, J., Briens, C., Berruti, F., and Ed, C., "Particle Attrition Mechanism with a Sonic Gas Jet Injected into a Fluidized Bed", *Chem. Eng. Sci.*, **62** 3809-3820 (2007b).

Midoux, N., Hosek, P., Pailleres, L., and Authelin, J.R., "Micronization of Pharmaceuticals Substances in a Spiral Jet Mill", *Powder Technol.*, **104** 113-120 (1999).

Palaniandy, S., Azizli, K. A. M., Hussin, H., and Hashim, S. F. S., "Effect of Operational Parameters on the Breakage Mechanism of Silica in a Jet Mill", *Miner. Eng.*, **21** 380-388 (2008).

Zanetti, M.C., Fiore, S., "Foundry Processes: The Recovery of Green Moulding Sands for Core Operations", *Resour. Conserv. & Recy.*, **38**, 243-254 (2002).

CHAPTER 6

Conclusions and Recommendations

Results and findings from this research and some recommendations are summarized in this section.

6.1 Conclusions

1. Experimental results during green sand reclamation show that there is some separation of clay and organic material from the silica sand when using a fluidized bed and an attrition nozzle. Removal of clay is by far more difficult than removal of the organic material, and the best results are obtained when the green sand is calcinated. Our estimates indicate that the proposed reclamation method is economically feasible as long as the reclaimed product complies with the minimum quality requirements for green sand to be used in core making.
2. In agreement with previous studies, it was found that particle size reduction is more efficient with Laval-type or convergent-divergent nozzles than with simple straight nozzles. The main difference between these nozzles is that the Laval-type produces supersonic velocities at the exit while the straight nozzle does not give velocities higher than the speed of sound.
3. An innovation in this research is the introduction of the equations for compressible flow to calculate the properties along the convergent-divergent nozzle especially at the nozzle exit. With this information, thrust can be calculated and it was found that thrust has a strong relationship with grinding efficiency.
4. An optimum half angle for the divergent section of the Laval nozzles with a conical divergent section was estimated. This half angle is in the range between 3^{o} and 8^{o} approximately. The proposed theory also gives the optimum length of the nozzle expansion section. All the convergent-divergent nozzles used in this research had a half angle between that range, and it is suspected that the A nozzle geometry is already an optimization of the Laval nozzles used for attrition. A more radical change in the supersonic nozzles geometry would probably be required to greatly improve the grinding efficiency.

5. It was confirmed that gases with lower molecular weight give higher grinding efficiency, which is defined as the new surface area created during attrition per unit mass of attriting gas, and that is because these gases reach higher velocities at the nozzle tip, for the same thrust. A correlation was developed to predict the grinding efficiency: it is valid for the experimental conditions in this study and it is not a general correlation, that is, it only takes into account variations in nozzle scale, nozzle geometry and attrition gases.
6. Jet penetration experiments show that use of triboelectric probes is an effective method to measure the penetration depth of supersonic gas jets.
7. Jet penetration can be directly correlated with thrust, even when using different gases.
8. As general confirmation from previous studies, it can be concluded that grinding efficiency is affected by nozzle size, nozzle geometry, and attrition gas properties and pressure. This research did not test for the effects of changes in fluidization velocity, or bed particles properties.
9. It is postulated that for supersonic nozzles, background pressure in the fluidized beds affects both grinding efficiency and jet penetration. Depending on the difference in pressure between the nozzle exit and the background, the supersonic nozzle can operate as underexpanded or overexpanded.

6.2 Recommendations

1. If more experiments with green sand are planned, the used of a convergent-divergent nozzle would be the next step. The recommendation is to use a Laval-type nozzle with a throat diameter smaller than the one used in the preliminary experiments. This will allow for higher grinding pressures using similar masses of air for attrition, resulting in higher values of exit velocities for the air and therefore higher momenta. Unlike the particle size reduction experiments, green sand reclamation requires just abrasion of the particles to remove the clay and

organic material, thus, a proper exit velocity of air at the nozzle tip and mass flow rate should be found to reduce fragmentation of the green sand particles.

2. The convergent-divergent nozzle used for particle size control studies may be considered close to an optimum for that specific type of nozzle. Another nozzle shape that can be used is a bell shape instead of a conical shape. The bell shape with a half angle close to zero at the nozzle exit should have less divergence losses. Probably the improvement in grinding efficiency, if any, would be minimal, but it would be worth trying these nozzle shapes. Experiment can be also performed using a plug or spike nozzle. This nozzle is similar to a Laval-type nozzle, but with a concentric, central piece. The main challenge for the proper use of this nozzle is its design and construction.
3. If general correlations are desired for grinding efficiency and jet penetration, it is recommended to conduct experiments using different fluidization velocities and bed particles. Also the location of the attrition nozzle, and bed mass and height may have an effect on grinding efficiency and jet penetration.
4. If it is desired to confirm whether grinding efficiency and jet penetration are affected by background or bed pressure, a fluidized bed that allows changing that pressure would be useful.

APPENDIX

Tables for supersonic nozzle exit conditions

A.1 Data for supersonic nozzles used in grinding experiments

Table A.1: Calculation of different properties at the exit of the supersonic nozzles used during the attrition experiments.

Attrition gas	Nozzle type	Throat diameter D_{th} (m)	Exit diameter D_e (m)	Attrition Press. P_T (kPa)	Area ratio A_e/A_{th} (-)	Exit sound veloc. U_s (m/s)	Mass flow rate $\dot{m}$ (kg/s)	Exit mach M_e (m/s)	Exit density ρ_e (kg/m^3)	Exit temp. T_e (K)	Exit Press. P_e (kPa)	Exit veloc. U_e (m/s)	Equiv. veloc. U_{eq} (m/s)	Thrust F (N)
Air	A1	0.00244	0.00424	138	3.02	222	0.0026	2.65	0.3	122.7	-90	588	104	0.3
	A1	0.00244	0.00424	414	3.02	222	0.0057	2.65	0.7	122.7	-77	588	395	2.2
	A1	0.00244	0.00424	620	3.02	222	0.0079	2.65	1.0	122.7	-68	588	467	3.7
	A1	0.00244	0.00424	1103	3.02	222	0.0133	2.65	1.6	122.7	-45	588	539	7.2
	A1	0.00244	0.00424	1275	3.02	222	0.0152	2.65	1.8	122.7	-37	588	553	8.4
	A1	0.00244	0.00424	1930	3.02	222	0.0224	2.65	2.7	122.7	-7	588	583	13.1
	A1	0.00244	0.00424	2550	3.02	222	0.0292	2.65	3.5	122.7	22	588	598	17.5
	A2	0.00206	0.00351	620	2.94	223	0.0056	2.62	1.0	124.3	-66	585	471	2.6
	A2	0.00206	0.00351	1275	2.94	223	0.0106	2.62	1.9	124.3	-34	585	554	5.9
	A2	0.00206	0.00351	1930	2.94	223	0.0157	2.62	2.8	124.3	-2	585	584	9.2
	A3	0.00175	0.00299	620	2.90	224	0.0041	2.60	1.0	125.1	-65	584	472	1.9
	A3	0.00175	0.00299	1275	2.90	224	0.0078	2.60	1.9	125.1	-33	584	554	4.3
	A3	0.00175	0.00299	1930	2.90	224	0.0115	2.60	2.8	125.1	0	584	584	6.7
	B	0.00244	0.00472	1103	3.74	211	0.0133	2.87	1.2	111.2	-62	607	526	7.0
	B	0.00244	0.00472	1275	3.74	211	0.0152	2.87	1.4	111.2	-56	607	542	8.2
	B	0.00244	0.00472	1930	3.74	211	0.0224	2.87	2.1	111.2	-34	607	580	13.0
	B	0.00244	0.00472	2550	3.74	211	0.0292	2.87	2.7	111.2	-14	607	599	17.5

Table A.1: Calculation of different properties at the exit of the supersonic nozzles used during the attrition experiments. (cont.)

Attrition gas	Nozzle type	Throat diameter D_{th} (m)	Exit diameter D_e (m)	Attrition Press. P_T (kPa)	Area ratio A_e/A_{th} (-)	Exit sound veloc. U_s (m/s)	Mass flow rate $\dot{m}$ (kg/s)	Exit mach M_e (m/s)	Exit density ρ_e (kg/m^3)	Exit temp. T_e (K)	Exit Press. P_e (kPa)	Exit veloc. U_e (m/s)	Equiv. veloc. U_{eq} (m/s)	Thrust F (N)
Air	C	0.00244	0.00462	1275	3.59	213	0.0152	2.83	1.5	113.4	-53	603	545	8.3
	C	0.00244	0.00462	1930	3.59	213	0.0224	2.83	2.2	113.4	-30	603	581	13.0
	C	0.00244	0.00462	2550	3.59	213	0.0292	2.83	2.9	113.4	-8	603	599	17.5
	D	0.00239	0.00280	1103	1.37	272	0.0127	1.74	4.4	183.6	128	473	535	6.8
	D	0.00239	0.00280	1930	1.37	272	0.0214	1.74	7.4	183.6	286	473	555	11.9
	E	0.00238	0.00350	1103	2.16	241	0.0126	2.29	2.4	144.1	-3	550	548	6.9
	E	0.00238	0.00350	1930	2.16	241	0.0213	2.29	4.0	144.1	64	550	579	12.3
	F	0.00239	0.00318	1103	1.77	253	0.0127	2.06	3.1	159.7	39	521	545	6.9
	F	0.00239	0.00318	1275	1.77	253	0.0145	2.06	3.5	159.7	60	521	553	8.0
	F	0.00239	0.00318	1930	1.77	253	0.0214	2.06	5.2	159.7	136	521	571	12.2
	G	0.00239	0.00490	1275	4.38	204	0.0145	3.04	1.2	103.5	-66	620	530	7.7
	G	0.00239	0.00490	1930	4.38	204	0.0214	3.04	1.8	103.5	-49	620	575	12.3
	S	0.00240	0.00240	620	1.00	314	0.0077	1.00	5.4	245.8	280	314	479	3.7
	S	0.00240	0.00240	1275	1.00	314	0.0147	1.00	10.3	245.8	626	314	507	7.4
	S	0.00240	0.00240	1930	1.00	314	0.0216	1.00	15.2	245.8	972	314	517	11.2

Table A.1: Calculation of different properties at the exit of the supersonic nozzles used during the attrition experiments. (cont.)

Attrition gas	Nozzle type	Throat diameter D_{th} (m)	Exit diameter D_e (m)	Attrition Press. P_T (kPa)	Area ratio A_e/A_{th} (-)	Exit sound veloc. U_s (m/s)	Mass flow rate $\dot{m}$ (kg/s)	Exit mach M_e (m/s)	Exit density ρ_e (kg/m^3)	Exit temp. T_e (K)	Exit Press. P_e (kPa)	Exit veloc. U_e (m/s)	Equiv. veloc. U_{eq} (m/s)	Thrust F (N)
Helium	A1	0.00244	0.00424	620	3.02	504	0.0031	3.01	0.1	73.2	-79	1518	1161	3.6
	A1	0.00244	0.00424	1275	3.02	504	0.0060	3.01	0.3	73.2	-59	1518	1378	8.2
	A1	0.00244	0.00424	1930	3.02	504	0.0088	3.01	0.4	73.2	-39	1518	1456	12.8
	D	0.00239	0.00280	1930	1.37	695	0.0084	1.83	1.1	139.4	211	1271	1425	12.0
0.82 Helium 0.18 Nitrogen	A1	0.00244	0.00424	138	3.03	361	0.0015	2.94	0.1	80.9	-93	1061	168	0.2
	A1	0.00244	0.00424	414	3.03	361	0.0032	2.94	0.2	80.9	-84	1061	687	2.2
	A1	0.00244	0.00424	620	3.03	361	0.0045	2.94	0.3	80.9	-77	1061	816	3.6
	A1	0.00244	0.00424	1275	3.03	361	0.0085	2.94	0.6	80.9	-55	1061	969	8.2
	A1	0.00244	0.00424	1930	3.03	361	0.0126	2.94	0.8	80.9	-34	1061	1023	12.8
Argon	A1	0.00244	0.00424	620	3.03	160	0.0099	3.01	1.5	73.6	-79	481	367	3.6
	A1	0.00244	0.00424	1275	3.03	160	0.0188	3.01	2.8	73.6	-59	481	436	8.2
	A1	0.00244	0.00424	1930	3.03	160	0.0278	3.01	4.1	73.6	-39	481	461	12.8
	F	0.00239	0.00318	1930	1.77	197	0.0266	2.22	7.7	112.0	78	437	460	12.3
CO_2	A1	0.00244	0.00424	1275	3.02	193	0.0182	2.52	2.6	151.0	-26	486	466	8.5
	A1	0.00244	0.00424	1654	3.02	193	0.0232	2.52	3.4	151.0	-5	486	483	11.2

A.1 Data for supersonic nozzles used in jet penetration experiments

Table A.2: Calculation of different properties at the exit of the supersonic nozzles used for jet penetration experiments.

Attrition gas	Nozzle type	Throat diameter D_{th} (m)	Exit diameter D_e (m)	Attrition Press. P_T (kPa)	Area ratio A_e/A_{th} (-)	Exit sound veloc. U_s (m/s)	Mass flow rate $\dot{m}$ (kg/s)	Exit mach M_e (m/s)	Exit density ρ_e (kg/m^3)	Exit temp. T_e (K)	Exit Press. P_e (kPa)	Exit veloc. U_e (m/s)	Equiv. veloc. U_{eq} (m/s)	Thrust F (N)
Air	A1	0.00244	0.00424	676	3.02	222	0.0086	2.65	1.0	122.7	-65	588	480	4.1
	A1	0.00244	0.00424	1275	3.02	222	0.0152	2.65	1.8	122.7	-37	588	553	8.4
	A1	0.00244	0.00424	1930	3.02	222	0.0224	2.65	2.7	122.7	-7	588	583	13.1
	A2	0.00206	0.00351	676	2.94	223	0.0060	2.62	1.1	124.3	-63	585	483	2.9
	A2	0.00206	0.00351	1275	2.94	223	0.0106	2.62	1.9	124.3	-34	585	554	5.9
	A2	0.00206	0.00351	1930	2.94	223	0.0157	2.62	2.8	124.3	-2	585	584	9.2
	A3	0.00175	0.00299	676	2.90	224	0.0044	2.60	1.1	125.1	-63	584	484	2.1
	A3	0.00175	0.00299	1275	2.90	224	0.0078	2.60	1.9	125.1	-33	584	554	4.3
	A3	0.00175	0.00299	1930	2.90	224	0.0115	2.60	2.8	125.1	0	584	584	6.7
	B	0.00244	0.00472	676	3.74	211	0.0086	2.87	0.8	111.2	-76	607	452	3.9
	B	0.00244	0.00472	1275	3.74	211	0.0152	2.87	1.4	111.2	-56	607	542	8.2
	B	0.00244	0.00472	1930	3.74	211	0.0224	2.87	2.1	111.2	-34	607	580	13.0
	D	0.00239	0.00280	676	1.37	272	0.0082	1.74	2.8	183.6	47	473	508	4.2
	D	0.00239	0.00280	1275	1.37	272	0.0145	1.74	5.0	183.6	161	473	541	7.9
	D	0.00239	0.00280	1930	1.37	272	0.0214	1.74	7.4	183.6	286	473	555	11.9

Table A.2: Calculation of different properties at the exit of the supersonic nozzles used for jet penetration experiments. (Cont.)

Attrition gas	Nozzle type	Throat diameter D_{th} (m)	Exit diameter D_e (m)	Attrition Press. P_T (kPa)	Area ratio A_e/A_{th} (-)	Exit sound veloc. U_s (m/s)	Mass flow rate $\dot{m}$ (kg/s)	Exit mach M_e (m/s)	Exit density ρ_e (kg/m^3)	Exit temp. T_e (K)	Exit Press. P_e (kPa)	Exit veloc. U_e (m/s)	Equiv. veloc. U_{eq} (m/s)	Thrust F (N)
Air	F	0.00239	0.00318	676	1.77	253	0.0082	2.06	2.0	159.7	-10	521	511	4.2
	F	0.00239	0.00318	1275	1.77	253	0.0145	2.06	3.5	159.7	60	521	553	8.0
	F	0.00239	0.00318	1930	1.77	253	0.0214	2.06	5.2	159.7	136	521	571	12.2
	G	0.00239	0.00490	676	4.38	204	0.0082	3.04	0.7	103.5	-81	620	425	3.5
	G	0.00239	0.00490	1275	4.38	204	0.0145	3.04	1.2	103.5	-66	620	530	7.7
	G	0.00239	0.00490	1930	4.38	204	0.0214	3.04	1.8	103.5	-49	620	575	12.3
Helium	A1	0.00244	0.00424	1275	3.02	504	0.0060	3.01	0.3	73.2	-59	1518	1378	8.2
	A3	0.00175	0.00299	676	2.90	504	0.0017	3.01	0.2	73.2	-77	1518	1206	2.1
	F	0.00239	0.00318	1275	1.77	622	0.0057	2.22	0.5	111.5	20	1381	1408	8.0
CO_2	A1	0.00244	0.00424	1275	3.02	193	0.0182	2.52	2.6	151.0	-26	486	466	8.5
	A2	0.00206	0.00351	1137	2.94	194	0.0115	2.50	2.5	152.5	-30	483	458	5.3
	A3	0.00175	0.00299	331	2.90	194	0.0029	2.49	0.9	153.1	-76	482	301	0.9
	B	0.00244	0.00472	1275	3.74	185	0.0182	2.72	2.1	140.0	-47	504	459	8.3
	F	0.00239	0.00318	193	1.77	193	0.0037	2.52	0.6	151.0	-85	486	305	1.1
	F	0.00239	0.00318	1275	1.77	193	0.0174	2.52	2.6	151.0	-26	486	474	8.3